Unit Cell Orientation and Batch Variation Effect on the Mechanical Behaviour of Simple Cubic Ti-6Al-4V Lattice Made by Electron Beam Powder Bed Fusion

Antony R. O. Wan

A research component submitted to

Auckland University of Technology

in fulfilment of the requirements for the degree of

Master of Philosophy (MPhil)

2024

School of Engineering, Computer and Mathematical Sciences

Abstract

Electron beam powder bed fusion (EB-PBF) can make Ti-6Al-4V biomedical bone implants with porous lattice structures that are fully customised and patient-specific, potentially improving osseointegration and preventing stress shielding of Ti-6Al-4V bone implants. However, the mechanical strength of simple Ti-6Al-4V porous lattice structures with geometrical lattice parameters that are favourable for osseointegration and osteoconduction with consideration for the factors of the ease of powder removal, unit cell orientation and batch variation between builds for small lattices in an industrial production setting for EB-PBF have yet to be examined and understood. The mechanical strength of lattice with simple cubic unit cells of features desired for biomedical bone implants was investigated.

This study examined the effect of unit cell orientation and batch variation on the mechanical strength of simple cubic Ti-6Al-4V lattice made with EB-PBF for quasi-static compressive and compressive-compressive fatigue loading. Four unit cell orientations of [001], [011], [111] and [$\sqrt{1/2}$ $\sqrt{1/2}$1] made from six batches of the simple cubic lattice were tested for in the quasi-static compressive test and two unit cell orientations of [011] and [$\sqrt{1/2}$ $\sqrt{1/2}$1] made from four batches of the simple cubic lattice were tested in the compressive-compressive fatigue test. Two net themes were used to print the specimens. Four batches were printed with net theme A and two with net theme B.

The unit cell orientation affected the mechanical behaviour of the simple cubic Ti-6Al-4V lattice structure under compressive load. The [001] orientation still behaves with a stretching-dominated deformation, even with a small strut diameter and pore diameter that follows the osteoconductive requirement. The [001] orientation is significantly stronger than the [011], [111], and [$\sqrt{1/2}$ $\sqrt{1/2}$1] orientations with bending-dominated deformation, which are in agreement with the quasi-static compressive simulation results. The [001] orientation has the highest compressive strength with $\sigma_{UCS\text{-}L}$ of 2.0 to 2.5 times higher, $\sigma_{y\text{-}L}$ of 1.8 to 2.1 times higher and E_L of 1.6 to 2.1 times higher than other orientations. The [011] and [$\sqrt{1/2}$ $\sqrt{1/2}$1] orientations were also found to affect the fatigue strength of the simple cubic Ti-6Al-4V lattice structure under cyclic compressive-

compressive loading. The fatigue strength generally follows the compressive strength trend of the lattice structure.

The batch variation factor affected the compressive strength behaviour of the simple cubic Ti-6Al-4V lattice structure. The specimens that were printed using both of the net themes A and B showed that they had been affected by the batch variation of either increasing the spread of the $\sigma_{UCS\text{-}L}$, $\sigma_{y\text{-}L}$ and E_L values or decreasing their mean values. The batch variation in net theme A were more significant in affecting the compressive strength of the printed lattice specimens. The batch variation factor also affected the fatigue strength of the simple cubic Ti-6Al-4V lattice structure with bending-dominated deformation under compressive-compressive cyclic loading. The fatigue strength generally follows the compressive strength of the lattice structure with the effect of the batch variation factor, but only in LCF regions. The fatigue strength of all the specimen batches seems to converge at 10.5 MPa past 10^6 cycles to failure.

Contents

List of Figures

List of Tables

Nomenclature

Abbreviations

AB	as-built
AM	additive manufacturing
BD	build direction
CAD	computer-aided design
EB-PBF	electron beam powder bed fusion
EBM	electron beam melting
HCF	high cycle fatigue
HIP	hot isostatic pressing
L-PBF	laser powder bed fusion
LCF	low cycle fatigue
LD	loading direction
MAM	metal additive manufacturing
PBF	powder bed fusion
SC	simple cubic
SD	standard deviation
SEM	scanning electron microscope
SLM	selective laser melting
Ti-6Al-4V	titanium 6-aluminium 4-vanadium
VOI	volume of interest

Symbols

[001]	unit cell orientation vector of [001]
[011]	unit cell orientation vector of [011]
[111]	unit cell orientation vector of [111]

$[\sqrt{1/2}\,\sqrt{1/2}1]$	unit cell orientation vector of $[\sqrt{1/2}\,\sqrt{1/2}1]$
$\bar{\rho}$	relative density, %
ϕ	porosity, %
σ_a	stress amplitude, MPa
σ_c	compressive strength, MPa
σ_{max}	maximum stress, MPa
σ_{min}	minimum stress, MPa
σ_m	mean stress, MPa
σ_N	fatigue strength at N cycles
$\sigma_{UCS\text{-}L}$	lattice ultimate compressive strength, MPa
$\sigma_{y\text{-}L}$	lattice yield strength with 0.2% strain offset, MPa
$\sigma_{y\text{-}SL}$	simulated lattice yield strength with 0.2% strain offset, MPa
ε	strain, %
$\varnothing$	electron beam spot diameter, μm
A_o	cross sectional area of VOI, mm^2
d_a	average pore diameter, mm
d_p	pore diameter, mm
d_{max}	maximum displacement, mm
D_o	lattice specimen diameter or VOI diameter, mm
$d_{s\text{-}e}$	effective strut diameter or thickness, mm
d_s	strut diameter or thickness, mm
E_{line}	line energy density, $J{\cdot}mm^{-1}$
E_L	lattice elastic modulus, GPa
E_o	specimen base material elastic modulus, GPa
$E_{SL[001]}$	simulated [001] lattice elastic modulus, GPa
$E_{SL[011]}$	simulated [011] lattice elastic modulus, GPa
$E_{SL[111]}$	simulated [111] lattice elastic modulus, GPa
$E_{SL[\sqrt{1/2}\,\sqrt{1/2}1]}$	simulated $[\sqrt{1/2}\,\sqrt{1/2}1]$ lattice elastic modulus, GPa
E_{SL}	simulated lattice elastic modulus, GPa
F_{max}	maximum force, N
h	scan line offset
h_m	melt pool depth
H_o	lattice specimen height or VOI height, mm

I_e	electron beam current, mA
l_c	cell size or unit cell length, mm
n	exponential factor
N_c	completed cycles
N_f	cycles to failure
P	electron beam power, W
R	stress ratio
s_c	cell size, mm
t	powder layer thickness
U_e	voltage acceleration, kV
v	scanning speed, mm•s^{-1}
w_m	melt pool width
FO	focus offset, mA
$S\text{-}V$	surface area to volume ratio, mm^{-1}
SF	speed function

Attestation of Authorship

I hereby declare that this submission is my own work and that, to the best of my knowledge and belief, it contains no material previously published or written by another person (except where explicitly defined in the acknowledgements), nor used artificial intelligence tools or generative artificial intelligence tools (unless it is clearly stated, and referenced, along with the purpose of use), nor material which to a substantial extent has been submitted for the award of any other degree or diploma of a university or other institution of higher learning.

Antony R. O. Wan

Acknowledgements

I want to express my gratitude to my supervisors, Prof. Dr Zhan Chen and Prof. Dr Sarat Singamneni, for giving me the opportunity to carry out this research and for their valuable guidance throughout.

I sincerely thank Zenith Tecnica Ltd for the financial and technical support, which this research would not be possible without. I would also like to sincerely thank the Zenith Tecnica team, Mr Kurt Schmidt, Mr Peter Sefont and Dr Bruno Le Razor, for their immense support and insightful collaboration.

In addition, I would like to give special thanks to the AUT team, Dr Yuan Tao, Mr Mark Masterton, Mr Jim Leahy, Mr Jim Crossen and Mr Ross Jamieson, for their invaluable help and support during the experimental work of this research. Also, thank you to Ms Yawen Huang for assisting in the simulation study.

Finally, I am profoundly grateful and cannot find the words to thank my mother, my family and my extended family for their unconditional love, support and encouragement. I specially dedicate this work to my beloved late father.

Chapter 1

Introduction

The first chapter of this study introduces the research by discussing the background and context of the metal additive manufacturing of EB-PBF and porous Ti-6Al-4V biomedical bone implants. Next, the research problem and scope of the research aims are presented, along with the research aims and objective, research significance, and study limitation. Lastly, the thesis outline is given at the end of this chapter.

1.1 Background

Lattice structures are topologically ordered structures of a repeating unit cell that is tessellated in all three dimensions. These structures can have internal spaces that are either open or closed and can be at large scales like building structures or small scales like cellular foams. The advantage of lattice structures is that the mechanical properties of the overall lattice can be different from the mechanical properties of the material from which the lattice is made, which is why lattice structures are also referred to as meta-materials. Lattice structures can be optimised for load support with as little material as needed, reducing the weight of the overall structure or designed to crush and have high energy absorption for material impact.

Processing metal alloys like Ti-6Al-4V into lattice structures has been time-consuming and difficult with fabrication or machining (subtractive manufacturing) methods. However, the advancement in metal additive manufacturing (MAM) has enabled the printing of complex-shaped lattice structures, especially with tiny features. Complex-shaped parts can be designed by computer-aided design and 3D printed layer by layer using MAM, which results in a near-net-shaped part with minimal machining or fettling required. These have gathered great interest for the application of biomedical bone implants made from Ti-6Al-4V, where not only customised and patient-specific parts can be printed based on the patient bone scans, but porous lattice structures can integrated

into the implant for better osseointegration, bone-implant fixation and the potential prevention bone mass loss around the implant due to stress shielding. In addition, the MAM technology of electron beam powder bed fusion (EB-PBF) has enabled the printing of reactive alloys like Ti-6Al-4V in an inert vacuum chamber that prevents the alloy from picking up oxygen during the melting and resolidification process, which is crucial for the biomedical implant application.

Figure 1.1
Schematic Diagram of an EB-PBF Machine

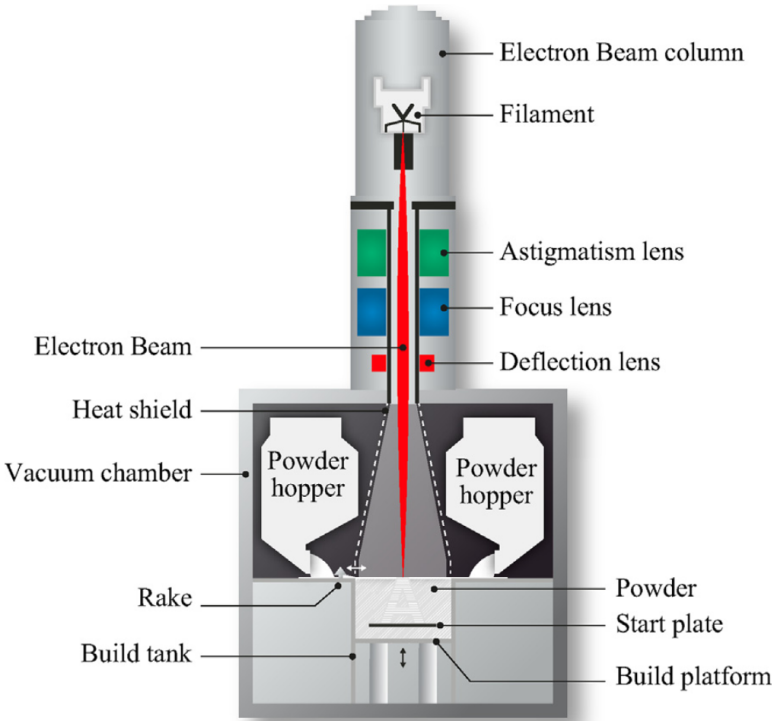

Note. Schematic diagram of an electron beam powder bed fusion or electron beam melting machine (Galati & Iuliano, 2018).

Many studies in the past decade have examined the mechanical properties of Ti-6Al-4V porous lattice printed by powder bed fusion (PBF) type of MAM. Some studies looked into the bio-function properties of the Ti-6Al-4V lattice. Many factors are still not fully understood for the numerous parameters involved in the lattice design and printing of Ti-6Al-4V porous lattice with tiny features using the EB-PBF process. Although many unit cell designs and modification methods, such as porosity grading and unit cell stretching, have been studied for their mechanical properties, there is still a lack of consideration of simple strut-based lattice with excellent powder removal properties, printability, and geometrical parameters that are favourable for bio-functions when used as a bone implant.

1.1.1 Metal Additive Manufacturing and EB-PBF

Electron beam powder bed fusion is a metal additive manufacturing technology that utilises the Powder Bed Fusion method, also known as electron beam melting (EBM) or selective electron beam melting (SEBM). EB-PBF uses a high-energy electron beam as its heat source for melting, as opposed to the laser beam used in selective laser melting (SLM), also known as laser powder bed fusion (L-PBF), which is another PBF-based metal additive manufacturing (AM) technology. In PBF, the feedstock material of powder is spread uniformly across a build platform to create a powder bed, where the heating source melts and fuses the powder selectively based on a pre-determined pattern, hence the name powder bed fusion. There are several advantages of EB-PBF over L-BPF, which are faster build times due to higher scan speeds of the electron beam, ideal for processing reactive feedstocks due to its inert build environment and low residual stresses in its as-built parts due to its preheating conditions, eliminating the need for post-processing heat treatment.

Figure 1.2
Ti-6Al-4V Alloy Powder as Feedstock for Powder Bed Fusion

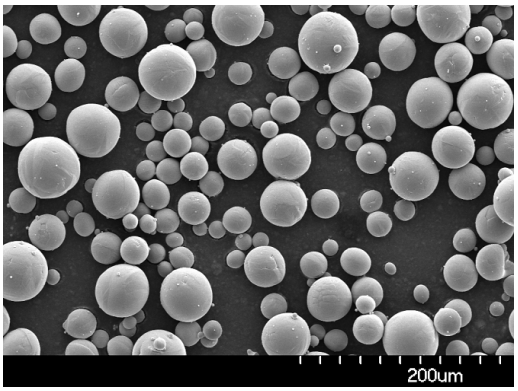

Note. SEM image of Ti-6Al-4V grade 5 powder for use in EB-PBF or L-PBF (AP&C, 2024).

EB-PBF machine consists of an electron beam column and a vacuum chamber, as shown in Figure 1.1. At the top of the electron beam column is the electron gun that comprises a single crystalline tungsten filament cathode that is heated to emit electrons, which are then accelerated into the column by the anode with the voltage acceleration of 60 kV, producing the high energy electron beam. The astigmatism and focus lens then shape and focus the electron beam, then redirect the beam to the desired X-Y location of the build surface by the deflection lens or scanning coils (Murr & Gaytan, 2014). These lenses are electromagnetic coils, and due to their fast control response, the beam can be controlled accurately at high scanning speeds of up to 8000 ms^{-1}, which enables multiple melt pools to be maintained at the same time and faster build time (General

Electric, 2024).

The metal powder is kept in the powder hoppers on each side of the vacuum chamber and fed to the rake. The rake fetches powder from both sides and distributes it evenly over the build platform. The start plate or the substrate is where the part is built, and this sits on top of a build platform that lowers into the build tank after each selective melting cycle. The vacuum chamber is pumped down to a minimum vacuum pressure of 5×10^{-4} mbar and is kept at 4×10^{-3} mbar during the build process with helium gas fed into the chamber continuously at about a litre per hour to maintain an inert atmosphere (General Electric, 2024). The heat shield separates the space where the electron beam moves about and the components in the vacuum chamber.

Figure 1.3
Illustration of the Electron Beam Powder Bed Fusion Build Cycle Process

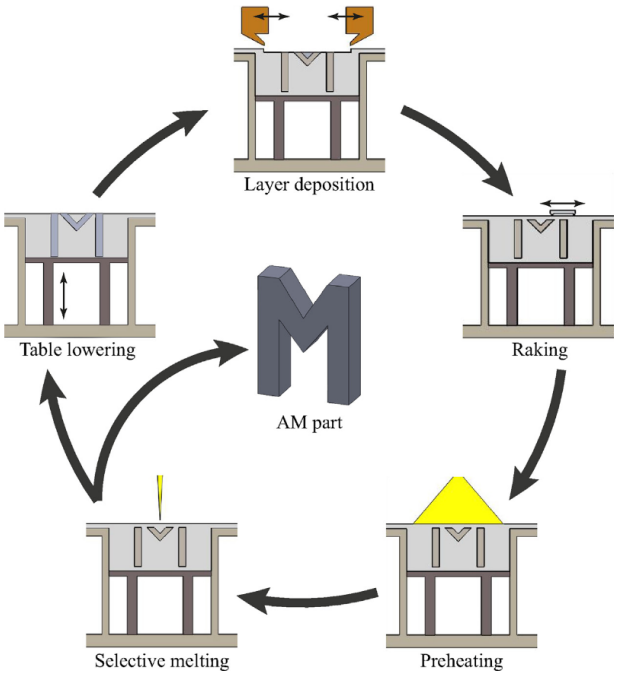

Note. The layer-by-layer build cycle process of the electron beam powder bed fusion (Galati & Iuliano, 2018). Each build cycle process begins at the table lowering steps and ends after the selective melting. The cycle is repeated until a full part is achieved.

The build process cycle is illustrated in Figure 1.3. It consists of five stages: table lowering, layer deposition (from powder hoppers), raking or fetching fresh powder, preheating and selective melting. However, in the initial stage before the beginning of the build process, the start plate is first preheated to a similar preheat temperature in the preheating stage of the build process cycle. The preheat temperature is material dependent, and the preheat temperature for Ti-6Al-4V is approximately 600 °C to 750 °C (S. Liu & Shin, 2019). These preheating steps result in a built part with low internal stresses, and unlike L-PBF, there is less need for post-processing heat

treatment for stress relief. After the initial preheating, the build process cycle begins and repeats for every layer slice of the CAD 3D drawing, building the whole part layer by layer.

EB-PBF technology enables the fabrication of geometrically complex metallic parts, which are nearly impossible to manufacture with conventional manufacturing methods. EB-PBF is perfect for printing topology-optimised parts and lattice structure integrated parts for light-weighting, increasing strength-to-weight ratio and customising part mechanical properties (Figure 1.4). Using parts with the least material needed (topology optimisation and lattice structure) for critical load-supporting parts requires a defined process-material-mechanical property of Ti-6Al-4V EB-PBF to ensure accurate essential factors of safety, especially when printing lattice structures that have geometric features of less than one millimetre.

Figure 1.4
Examples of Complex Shaped Ti-6Al-4V Parts Printed with EBPBF

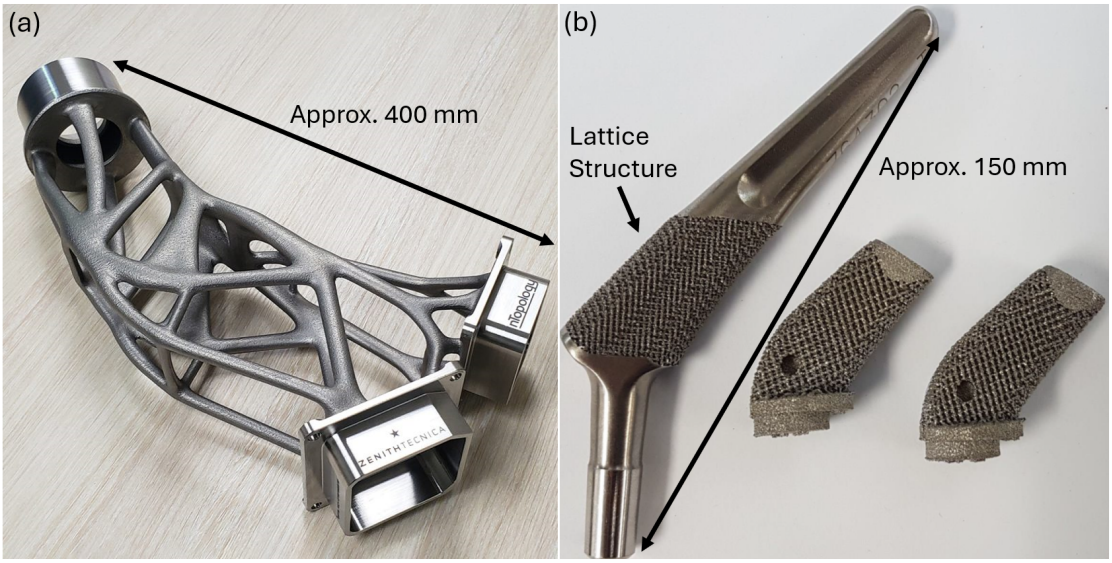

Note. EB-PBF enables the manufacturing of complex shapes with high resolution (a) topology optimised support structure for aerospace application (Zenith Tecnica, 2024) and (b) femoral stem implant with porous lattice structure for hip replacement (Zenith Tecnica, 2024).

1.1.2 Porous Ti-6Al-4V Biomedical Bone Implant Printed with EB-PBF

EB-PBF technology can produce metal parts with complex geometry, which are impossible to make with conventional manufacturing methods. One of the best applications of this metal AM technology is fabricating metallic parts with topology optimisation or lattice structure for light-weighting, increasing strength-to-weight ratio, and customising part mechanical properties. The use of EB-PBF in printing porous Ti-6Al-4V medical implants has been of interest since the beginning of the EBM technology. It has the potential to solve two critical problems of current

Ti-6Al-4V medical implants of lack of porosity for osseointegration and stress shielding due to elastic modulus mismatch by incorporating porous lattice structure in the implant (Wang et al., 2016; Zadpoor, 2019).

Figure 1.5
Illustration of Osseointegration for Solid and Porous Ti-6Al-4V Implant

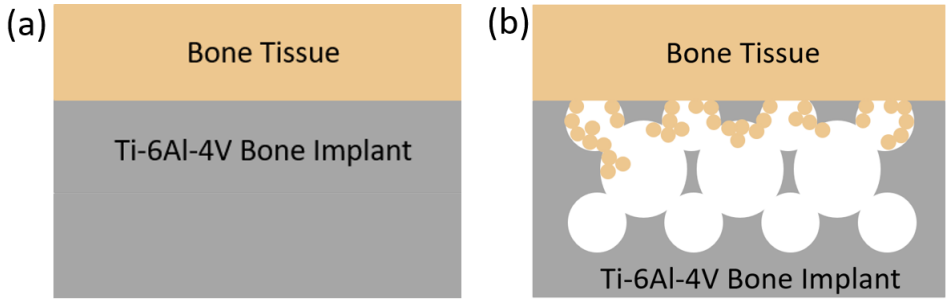

Note. Osseointegration example of (a) solid Ti-6Al-4V bone implant and (b) porous Ti-6Al-4V bone implant with bone cells growth into the porous spaces for bone-implant fixation. Own work.

The incorporation of porous lattice structures in biomedical bone implants, like in Figure 1.4(b), provides the porous space that allows the bone cells to populate and grow, as illustrated in Figure 1.5. This improves the fixation of the implant with the bone compared to solid Ti-6Al-4V implants and prevents implant loosening over time, which avoids painful and costly revision surgery for the patient. The lattice structure also has the potential to prevent stress shielding, which happens with solid Ti-6Al-4V implants, by having a lower elastic modulus compared to solid Ti-6Al-4V. Stress shielding occurs when the elastic modulus of the solid implant is too high compared to bone, causing the stresses during loading to be transmitted through the solid Ti-6Al-4V implant and bypassing the bone cells around the implant (B. Liu et al., 2021), as illustrated in Figure 1.6. This is due to the continuous remodelling of the bone tissue, where the bone adapts to the mechanical stresses it experiences. Bones with loads and stresses will cause more bone cells to be produced, making the bone stronger, while bones without loads or stresses will have their bone cells reabsorbed, causing diminishing bone mass (Naghavi et al., 2022), as shown in Figure 1.7.

In this thesis, the reference to lattice structure is understood to be the open structure and porous type that is geometrically isotropic. This means that the empty spaces in the cell are interconnected to adjacent cells through the openings of pores at the faces of the cell and that the same cells are tessellated through both sides of the 3D axes, which form the lattice structure.

Figure 1.6
Illustration of Stress Shielding with Solid Femoral Implant

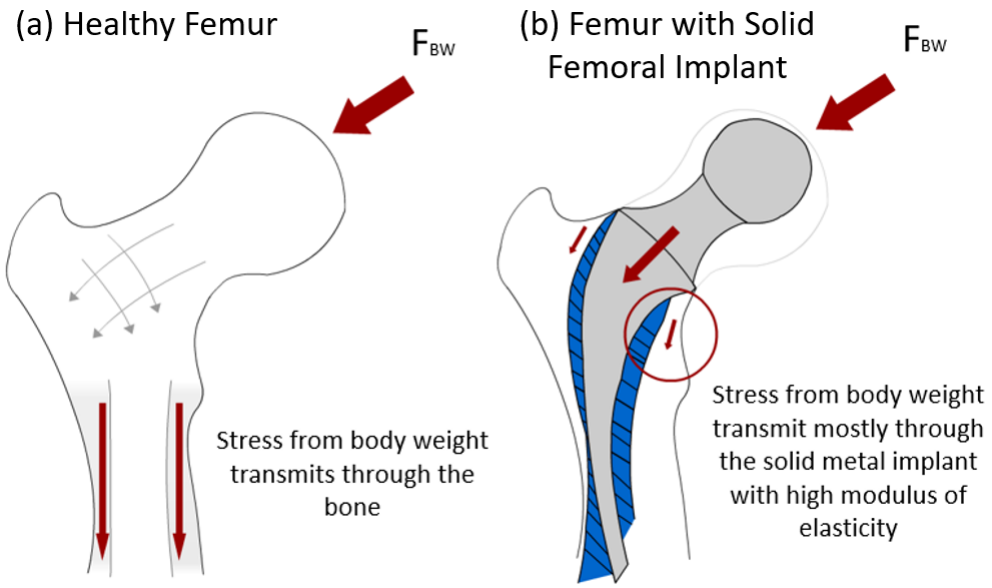

Note. (a) The stress from the body weight is transmitted through the bone cells in a healthy femur, while (b) the stress from the body is transmitted through the solid implant bypassing some bone cells due to the stiffer solid implant compared to bone cells (CORE-Materials, 2006).

Figure 1.7
Low Bone Mass in Femur due to Stress Shielding

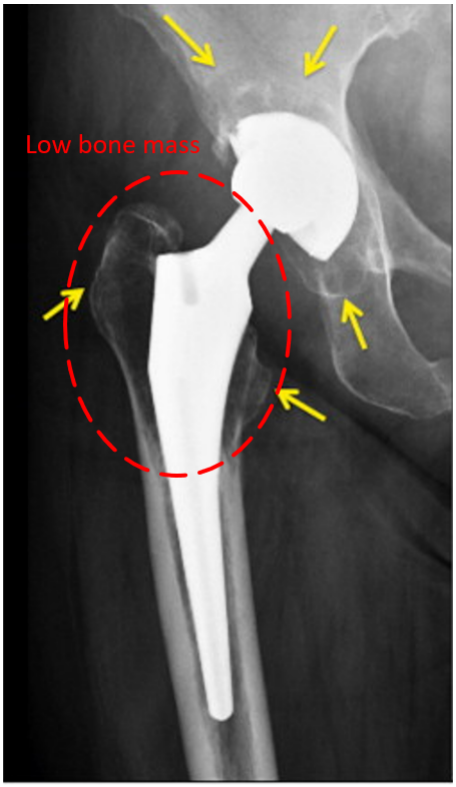

Note. Radiograph image of a hip replacement showing low bone mass density at the top end of the femur due to stress shielding (Millis, 2014).

1.2 Research Problem

Additive manufacturing of metals has advanced to the point that biomedical bone implant parts made from Ti-6Al-4V alloy can be custom-made for patients and incorporate lattice structures to mimic trabecular bone structures for better osseointegration and stress shielding prevention. Although studies have looked into various unit cell designs and modification methods to improve the mechanical strength of the lattice, such as porosity grading and unit cell strengthing, there is a lack of consideration for the factors of unit cell orientation and batch variation of simple unit cell designs that have good printability and ease of powder removal. The mechanical properties of Ti-6Al-4V lattice structures with the elementary unit cell design of simple cubic are not fully understood for the factor of unit cell orientation relative to the loading direction and the influence of batch variation from the electron beam powder bed fusion process in an industrial setting.

The mechanical performance of the lattice in biomedical bone implants is critical in ensuring that the lattice does not fail under load during everyday use. A balance between the mechanical strength and porosity for optimum osseointegration and osteoconduction has to be achieved for the lattice in the implant to be beneficial. Numerous studies have examined the mechanical properties of different unit cell designs, including complex designs created by triply periodic minimal surfaces (TPMS) to improve the mechanical performance of the lattice. However, these studies do not consider the lattice geometries favourable for osseointegration, which are high porosity and surface area, with pore sizes of about 0.3 mm to 0.6 mm (Barba et al., 2019). The factor of powder removal has also been ignored in most studies, especially for TPMS designs, when selecting the lattice geometry parameters tested. The literature examining the mechanical properties of unit cell designs also does not consider the unit cell orientation relative to the loading direction factor, which is essential when considering the orientation of the unit cell in the lattice of a biomedical bone implant, where loading may not be in a single direction.

Another factor that has been overlooked in the current literature is the batch variation effect for the process of EB-PBF, which is present in an industrial setting due to the nature of production operations when using EB-PBF machines. Different ordered parts are stacked within the build volume to maximise the number of parts per build batch for a cost-effective operation, which means that parts between batches will inherently have variation. These variations are primarily negligible when the parts have large geometries and a finishing step of machining involves getting the part to the final dimensions. However, the batch variations may be significant for lattices with tiny features of less than a millimetre and are used in as-built conditions. Most studies have specimens printed in a single batch and do not consider the batch variation factor.

1.3 Scope of the Study

1.3.1 Research Aims and Objective

This study aims to understand the effects of unit cell orientation and batch variation on the mechanical behaviour of Ti-6Al-4V lattice structure with simple cubic unit cell design and osteoconductive lattice parameters made with EB-PBF during quasi-static and cyclic compressive loading. The objectives of this thesis are listed as follows.

1. Investigate and analyse the quasi-static compressive strength of Ti-6Al-4V simple cubic lattices with four orientations made from different build batches using EB-PBF.

2. Examine the Ti-6Al-4V simple cubic lattice morphology and collapse deformation behaviour to help understand the quasi-static compressive strength behaviour observed.

3. Analyse and compare the compressive strength of EB-PBF strut-based Ti-6Al-4V lattices from literature with the experimental data obtained.

4. Investigate and analyse the compression-compression fatigue strength of Ti-6Al-4V simple cubic lattices with two orientations made from different build batches using EB-PBF.

5. Examine the Ti-6Al-4V simple cubic lattice fatigue fracture to help understand the compressive fatigue strength behaviour observed.

6. Analyse and compare the fatigue strength of EB-PBF and L-PBF strut-based Ti-6Al-4V lattices from literature with the experimental data obtained.

The research questions of this study based on the review of current literature in the next chapter are presented in Section 2.4.

1.3.2 Research Significance

EB-PBF can produce Ti-6Al-4V biomedical bone implants with porous lattice structures that are fully customised and patient-specific, potentially improving osseointegration and preventing stress shielding of Ti-6Al-4V bone implants. However, the mechanical strength of simple Ti-6Al-4V porous lattice structures with geometrical lattice parameters that are favourable for osseointegration and osteoconduction with consideration for the factors of the ease of powder removal, unit cell orientation and batch variation between builds for small lattices in an industrial setting for EB-PBF have yet to be examined and understood. The mechanical strength of lattice with simple

cubic unit cells of features desired for biomedical bone implants was investigated. Unit cell orientation and batch variation significantly affected the mechanical strength of simple cubic Ti-6Al-4V lattice. The findings of this study will help advance the understanding of the mechanical strengths of simple lattice structures that are favourable for osseointegration when produced in an industrial production setting and aid in selecting unit cell orientation to match load direction in a biomedical bone implant.

1.3.3 Study Limitations

One of the limitations of this study is the limited number of specimens available for the experiment. The study was conducted within industrial settings, which was also one of the objectives of this study, which was to examine the batch variation effect. Therefore, the printing and availability of these specimens depend significantly on the collaborating company, where batch samples can only be printed when there is a scheduled build with the availability of space within the build volume for the specimens. This is because the printing of specimens is done together within the production process of the collaborating company, which is the only financially viable way for the specimen to be made without costing the company extra production time for machine setup and turnover. Therefore, the specimens are limited, and the number of specimens for each batch and orientation also differ.

Another limitation of this research is the limited information on the net theme used for printing the lattice specimens in the EB-PBF machine. The net theme is a melting program used in the Arcam EBM Q10plus machine designed for printing tiny features, such as the porous lattice structure, and is different from the common melt theme used for printing solid parts. The net theme used for the company's production operation was updated during the study, resulting in five batches with the original net theme and another two with the updated net theme. The machine's supplier does not disclose the exact information for the net themes or their differences.

1.4 Thesis Outline

The first chapter introduces the research by discussing the background and context of the metal additive manufacturing of EB-PBF and porous Ti-6Al-4V biomedical bone implants. Next, the research problem and scope of the research aims are presented, along with the research aims and objective, research significance, and study limitation. Lastly, the thesis outline is given at the end of this chapter.

In the second chapter, the first section reviews the current literature on porous lattice structures

and osteoconductive porous lattice structures for biomedical bone implants. The second section reviews the current literature on the metal additive manufacturing of electron beam powder bed fusion and its printing process for Ti-Al-4V lattice structures. The third section reviews the existing literature on the mechanical behaviour of Ti-6Al-4V lattices made with powder bed fusion. The fourth and final section summarises the literature gaps and lists the research questions for this thesis.

The third chapter will present and detail the experimental designs and procedure for testing the mechanical strength of the simple cubic Ti-6Al-4V lattice. The details of the simple cubic lattice specimen design are first outlined with the details of the EB-PBF machine and the batch processing. Next, examining the lattice structure using scanning electron microscopy is specified. Then, the experimental mechanical testing for the quasi-static compressive test and compression-compression fatigue test are detailed. Lastly, the numerical analysis of the quasi-static compressive test is described.

In the fourth chapter, the results of the experiments conducted, as stated in the previous chapter, are presented and discussed in two sections to understand how this answers the research questions outlined in the second chapter. The first section presents the data and analysis from the quasi-static compression experiment with the simulated test data, followed by the discussion of findings and comparison with similar simple cubic Ti-6Al-4V lattice quasi-static compressive data from existing studies. The second section presents the experimental data and analysis for the compressive fatigue test. A discussion of the findings with compressive fatigue test data from current literature follows at the end of the chapter.

The last and concluding chapter summarises the key research findings of this study relative to the research questions stated in the second chapter. The lists of possible opportunities for future research based on the current findings are presented at the end of the chapter.

Chapter 2

Literature Review

In this chapter, the first section reviews the current literature on porous lattice structures and osteoconductive porous lattice structures for biomedical bone implants. The second section reviews the current literature on the metal additive manufacturing of electron beam powder bed fusion and its printing process for Ti-Al-4V lattice structures. The third section reviews the existing literature on the mechanical behaviour of Ti-6Al-4V lattices made with powder bed fusion. The fourth and final section summarises the literature gaps and lists the research questions for this thesis.

2.1 Porous Lattice Structures and Osteoconductive Lattice

2.1.1 Unit Cell Designs and Simple Cubic Unit Cell

Lattice structures are a type of cellular structure that are topologically ordered and have a unit cell repeated and tesselated in all three dimensions. A unit cell for a lattice structure is a cube or cuboid shaped, and the structure in the unit cell will have a shape known as unit cell design that connects and forms a lattice structure when the unit cell is repeated along the three axes (Figure 2.1). Unit cell designs for porous lattice structures can be categorised into three types, which are strut-based, skeletal-TPMS and sheet-TPMS, as summarised by Al-Ketan et al. (2018) and later again by Benedetti et al. (2021), shown in Figure 2.2. The studies of lattice structures made with metal additive manufacturing (MAM) that uses the powder bed fusion (PBF) process have started with strut-based unit cell designs due to its design simplicity and ease of creation using computer-aided design software. After that, triply periodic minimal surfaces (TPMS) based unit cell design has gained popularity in studies. TPMS unit cell designs are generated using trigonometric equations, and the unit cell parameters are tweaked by changing the input into the equation (Gupta & Babu L, 2023). TPMS-based unit cell designs are categorised into two types, skeletal-TPMS and sheet-

TPMS, where skeletal-TPMS has shapes that resemble struts, and sheet-TPMS has a continuous sheet as its structure.

Figure 2.1
Illustration of Unit Cell and Lattice

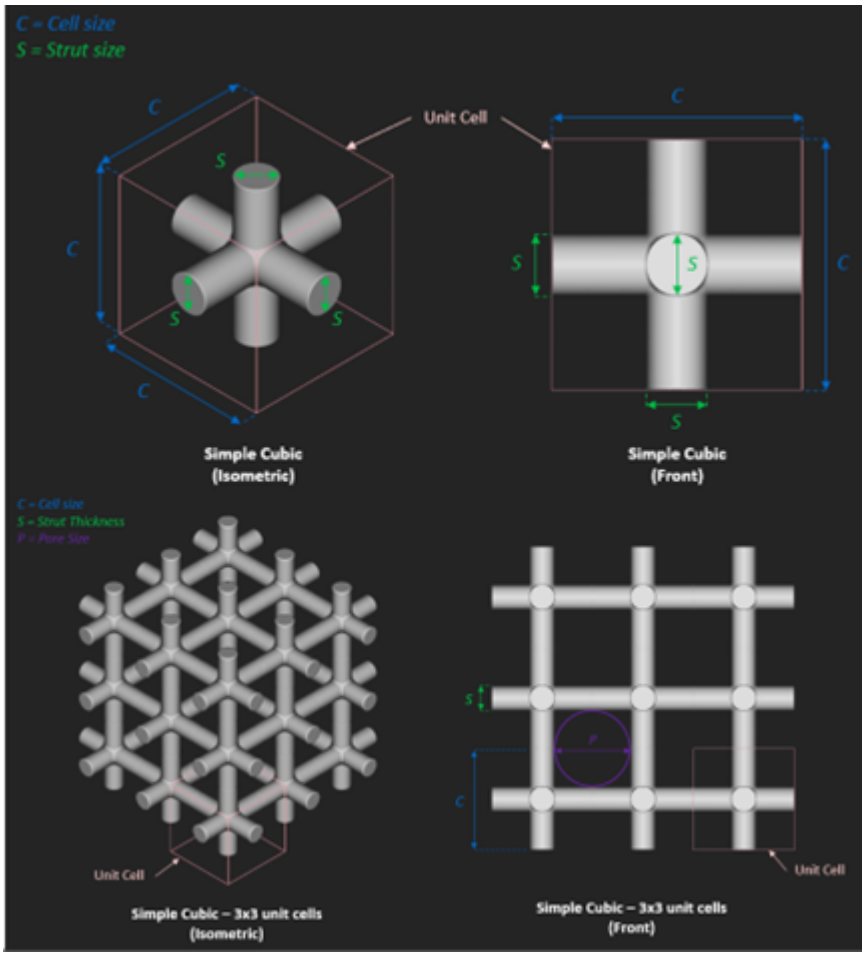

Note. Example of a unit cell with a simple cubic design on the top two images and a lattice structure at the bottom two images when the simple cubic unit cell is repeated three times along the three-dimensional axes. l_c is the cell size and is similar to l_c. d_s is the strut size or diameter and is similar to d_s. P is the pore diameter and is similar to d_p. Own work.

The simple cubic is one of the basic strut-based unit cell designs. It consists of one node at the centre of the cell that is formed by the intersection of three cylindrical struts (Figure 2.1). The lattice structure created by tessellating the simple cubic unit cell has the combined struts forming a cube, thus the simple cubic name. This unit cell is also referred to as cubic unit cell design in literature (Ahmadi et al., 2015; Parthasarathy et al., 2010). Another version of the simple cubic is shown in Figure 2.2(a), where quarters of the strut along the edges of the cube form the unit cell. The simple cubic has a uniform pore diameter on all its faces, as shown in Figure 2.3. Its simple design allows for easy powder removal post-print due to the clear line of sight through the face of

the unit cell and its lattice.

Figure 2.2
Types of Unit Cell Design

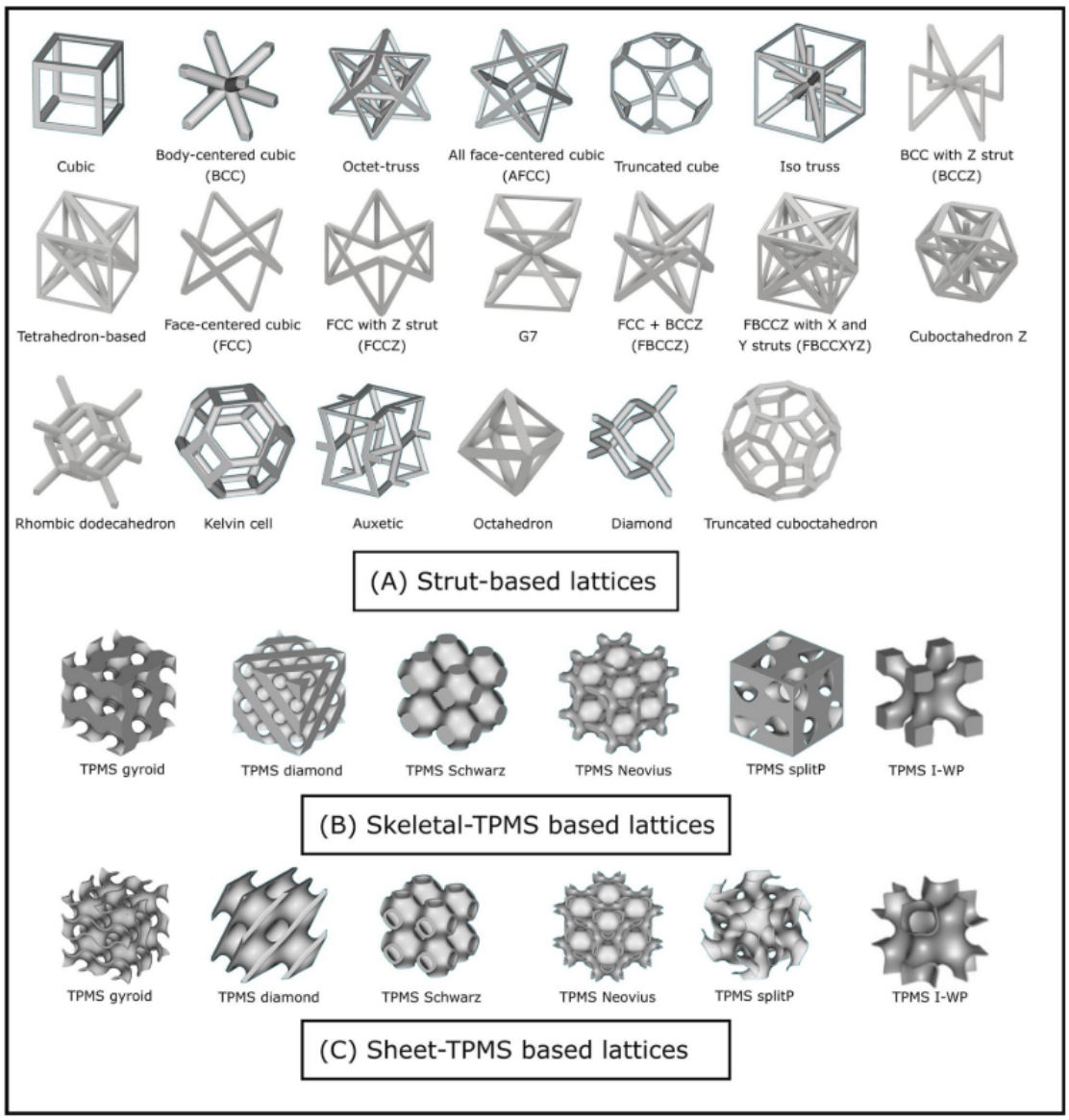

Note. Categories of unit cell designs used in lattice structures made with metal additive manufacturing as defined by Benedetti et al. (2021). There are three categories of unit cell designs, which are (a) strut-based lattices, (b) skeletal-TPMS based lattices and (c) sheet-TPMS based lattices. TPMS is triply periodic minimal surfaces.

2.1.2 Properties and Parameters of Porous Lattice Structures

The parameters of the porous lattice structures are related to the unit cell design parameters. These lattice parameters are used to describe and define the geometric properties of the lattice structure. There are generally three unit cell design parameters. First is the cell size or unit cell length, l_c, which is the length of the cubic unit cell. Second is the strut size or strut diameter, d_s, which is

the diameter of the struts in strut-based and TPMS-skeletal based unit cell designs. Strut diameter for skeletal-TPMS unit cells may be expressed as a few d_s corresponding to specific locations in the unit cell structure. Sheet thickness would be equivalent to the strut diameter for TPMS-sheet based unit cell designs. Third is the pore size or pore diameter, d_p, which can be defined as the largest sphere that can pass through the face or at a plane through a unit cell (Figure 2.3). The unit cell design may have more than one d_p if the design has more than one opening at the face, and additional pore diameters may be formed between combined unit cells as shown in Figure 2.3(b). All of these parameters are to be defined with additional information that will sufficiently describe the geometry of the unit cell design.

Figure 2.3
Pore Sizes Examples for Strut-based Lattice Structure

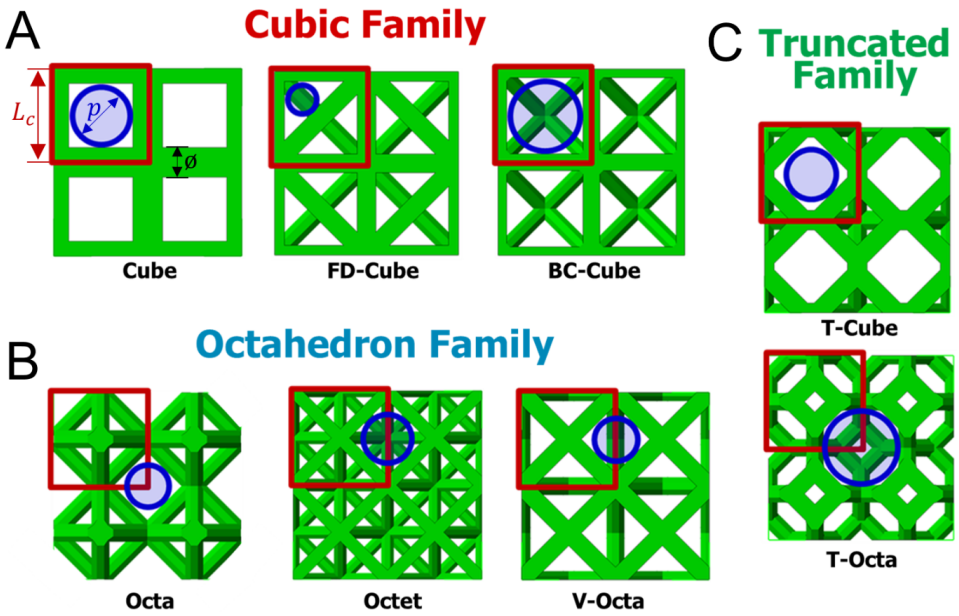

Note. Example of pore sizes for different types of strut-based lattice structures by Egan et al. (2017). L_c is the unit cell length, similar to cell size, l_c. p is the pore size or pore diameter, similar to d_p.

The unit cell design parameters form the lattice structure parameter of relative density or porosity ϕ, and surface area to volume ratio, S-V. The relative density, $\bar{\rho}$ of the lattice is defined as the ratio of the density of the lattice to the density of the material that the lattice is made of, as shown in Equation 2.1 and usually expressed as a percentage. For example, a relative density of 20 % translates to the lattice structure having a mass of 20 % of the solid with the same material and overall dimension. The density of the lattice is the mass of the lattice structure, m_L over the volume of interest, *VOI* or the volume of the overall dimension of the lattice structure, as shown in Equation 2.2. Relative density can also be expressed as porosity, as shown in Equation 2.3 and

the porosity of a lattice structure is the percentage of void volume to the overall lattice structure volume or *VOI*.

$$\bar{\rho} = \frac{\rho_L}{\rho_o} \tag{2.1}$$

$$\rho_L = \frac{m_L}{VOI} \tag{2.2}$$

$$\phi = 1 - \bar{\rho} \tag{2.3}$$

$$S\text{-}V = \frac{A_L}{VOI} \tag{2.4}$$

The surface area of the lattice structure is the surface area that makes up the wall of the interconnected porosity. A surface area to volume (S-V) ratio value is more useful as a lattice parameter value that can be used for comparing between lattice structures instead of just the surface area of a lattice, and this is calculated by taking the surface area of the lattice, A_L and dividing it by the overall dimension of the lattice structure or the *VOI*. The S-V ratio parameter of the lattice structure is of interest based on the intended application of the lattice, such as for heat exchanger application between the lattice and fluid (Catchpole-Smith et al., 2019) or osteoconductivity for osseointegration of biomedical implants. A higher S-V ratio would preferred to increase the contact between the lattice structure and fluid for heat transfer or increase the surface area available for the bone cells to grow and populate on.

$$\frac{\sigma_{UCS\text{-}L}}{\sigma_{UCS\text{-}o}} = C_1 \left(\frac{\rho_L}{\rho_o}\right)^{n_1} \tag{2.5}$$

$$\frac{\sigma_{y\text{-}L}}{\sigma_{y\text{-}o}} = C_2 \left(\frac{\rho_L}{\rho_o}\right)^{n_2} \tag{2.6}$$

$$\frac{E_L}{E_o} = C_3 \left(\frac{\rho_L}{\rho_o}\right)^{n_3} \tag{2.7}$$

It is well established that when the relative density of the porous lattice structure made with PBF is increased (and porosity decreased), its compressive strength, yield strength and elastic modulus also increase (Alomar & Concli, 2020; Bonatti & Mohr, 2019; Del Guercio et al., 2020; McGregor et al., 2021). The relationship of the mechanical strength of the lattice to its relative density can be characterised using the characterisation of cellular structures by Gibson and Ashby (1997) using the Gibson-Ashby model, where the ratio of the mechanical strength of the lattice to its material is related to the ratio of the density of the lattice structure to its material density. The Gibson-Ashby model can be written for lattice structure as Equation 2.5 for ultimate compressive strength, Equation 2.6 for yield strength and Equation 2.7 for the elastic modulus of the lattice structure. The constants of C_1, C_2, C_3, and power constants of n_1, n_2 and n_3 are dependent on the

unit cell design and the deformation modes of the lattice with the unit cell design under loading (Deshpande et al., 2001), which are determined experimentally. $\sigma_{y\text{-}L}$ and E_L are the yield strength and elastic modulus of the lattice, while $\sigma_{y\text{-}o}$ and E_o are the yield strength and elastic modulus of the material of the lattice or when the lattice is fully solid.

Figure 2.4
Deformation Modes of Simple Lattice Structures

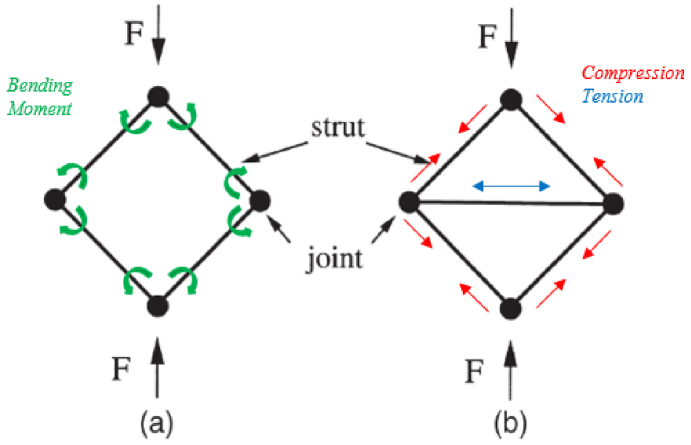

Note. Illustration of (a) bending deformation and (b) stretching deformation modes for simple lattice structures by Deshpande et al. (2001).

The illustration of bending deformation and stretching deformation modes of simple lattice structures by Deshpande et al. (2001) is shown in Figure 2.4. A bending-dominated deformation lattice will have a bending moment in the struts during loading. In contrast, a stretching-dominated deformation lattice will have a combination of compression and tension along the strut. Lattice structures with stretching-dominated deformation are stronger than those with bending-dominated deformation (Zhong et al., 2023). There have been many factors considered on how it affects $\sigma_{UCS\text{-}L}/\sigma_{UCS\text{-}o}$, $\sigma_{y\text{-}L}/\sigma_{y\text{-}o}$ and E_L/E_o of the Ti-6Al-4V lattice made with EB-PBF by studies reviewed by Del Guercio et al. (2021b) and X. Z. Zhang et al. (2018). However, the unit cell orientation relative to the loading direction factor has not been considered as a factor.

2.1.3 Porous Ti-6Al-4V Lattice for Biomedical Bone Implant

EB-PBF technology can produce metal parts with complex geometry, which are impossible to make with conventional manufacturing methods. The best application of this metal AM technology is in fabricating metallic parts with topology optimisation or lattice structure for lightweighting, increasing strength-to-weight ratio and customising part mechanical properties. The use of EB-PBF in printing porous Ti-6Al-4V medical implants has been of interest since the be-

ginning of the EBM technology. It has the potential to solve two critical problems of current Ti-6Al-4V medical implants of lack of porosity for osseointegration and stress shielding due to elastic modulus mismatch by incorporating porous lattice structure in the implant (Sumner, 2015; Tan et al., 2017).

Osseointegration is the structural and bio-functional integration of the bone with the medical implant (Branemark, 1983). This involves osteoconduction, which is the population of osteoblast cells that form new bone cells and vascularisation to facilitate blood and nutrient supply. An implant with poor or no osseointegration can lead to bone scar tissue growth (fibrous tissues) at the implant-bone interface and causes poor implant fixation or loosening (Jin & Chu, 2019). An interconnected porous structure in the implant at the bone-implant interface is required for osseointegration. However, the performance of osseointegration is dependent on how osteoconductive the implant porous structure (Ryan et al., 2006).

Figure 2.5
Preferred Pore Sizes for Biomedical Bone Implant Application

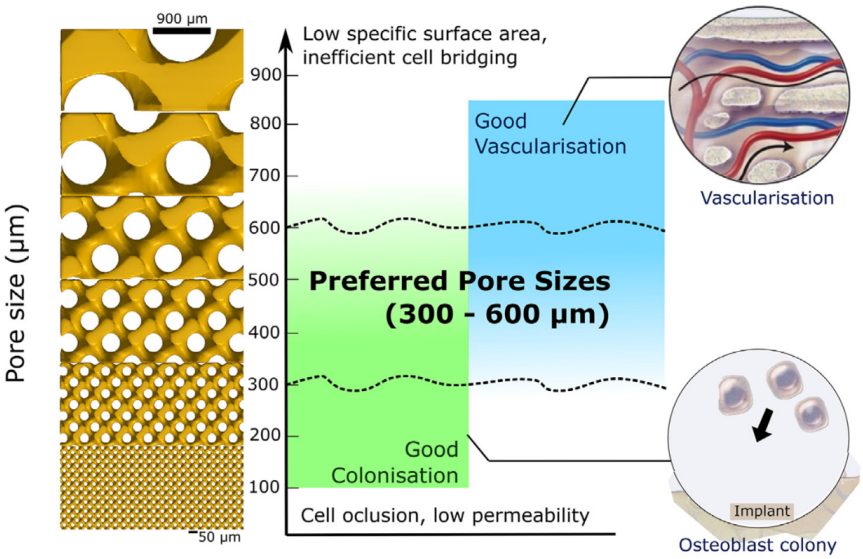

Note. Range of preferred pore sizes for osteoconductivity of the lattice structure for osseointegration of biomedical bone implant, as summarised from literature by Barba et al. (2019).

A crucial parameter that affects the osteoconductivity of the porous lattice structure in the implant is the pore size, d_p of the lattice structure. According to Barba et al. (2019), from their comprehensive review of studies, summarised that d_p of the lattice structure for porous implant n the range of 300 µm to 600 µm enables both the excellent population of osteoblast cells and vascularisation (Figure 2.5). Larger d_p than 600 µm will promote good vascularisation but cause poor colonisation of bone cells. On the other hand, smaller d_p than 300 µm allows good colonisation of

bone cells but causes poor vascularisation. Therefore, 300 μm to 600 μm is a preferred range that balances both good colonisation of bone cells and good vascularisation in the lattice structure.

Other than pore size, the surface area of the porous structure and permeability are also essential factors for osteoconductivity (Wang et al., 2016). A larger surface area provides more area for osteoblast cells to adhere and for bone cells to grow. A higher permeability, which is a lower resistance to internal fluid flow through the interconnected porous spaces of the lattice structure, will favour better transportation of cells and nutrients. There is no exact value of a minimum surface area and permeability for the requirement of osteoconductivity mentioned. Therefore, the pore size is taken as the main criteria for osteoconductivity in this proposed study, as the preferred pore sizes mentioned by Barba et al. (2019) for bone colonisation and bone vascularisation can also be assumed to have favourable surface area and permeability. Therefore, the lattice parameter for an osteoconductive porous Ti-6Al-4V lattice structure for the biomedical bone implant can be summarised into two parameters:

- Pore size, d_p = 300 μm to 600 μm
- Surface area to volume ratio, S-V = higher is better

Although there have been many studies done on the mechanical strengths of Ti-6Al-4V lattice structures made by PBF additive manufacturing with consideration for a biomedical bone implant like the studies in the review by McGregor et al. (2021), there has not been a consideration of a lattice structure that not only have the lattice parameters as stated above but also have a lattice structure has a good printability by EB-PBF and ease of powder removal, which is especially important for lattices with small pore sizes. The lattice structure with the factors considered would use a simple unit cell design like the simple cubic.

2.1.4 Mechanical Properties for Ti-6Al-4V Lattice Biomedical Bone Implant

The critical issue for a non-porous and solid Ti-6Al-4V medical implant is the stress-shielding effect, as shown in Figure 1.6. Bone cells are in a continuous cycle of removal (by the osteoclast cells) and generation (by the osteoblast cells), which respond to the load stresses within the skeletal system. This enables the regeneration of damaged bone and the reinforcement of bones that experience high stresses (B. Liu et al., 2021). On the other hand, the lack of stress stimulus can also cause bone reabsorption, where the bone loses density and mass (Figure 1.7). The stress-shielding effect is caused by the mismatch of elastic modulus, where the implant has an elastic modulus much greater than the bone, absorbs the loading stresses and prevents the transfer

of stress through the bones, where the implant is attached (Karachalios et al., 2004; Nagels et al., 2003). This eventually leads to the weakening of the surrounding bone and causes the loosening of the implant or fixation failure. Therefore, a Ti-6Al-4V lattice structure must have an elastic modulus lower than a solid Ti-6Al-4V and closer to bone. Table 2.1 shows the elastic modulus values of human bones.

Table 2.1
Mechanical Strength of Human Bone

Bone	Porosity (%)	Elastic Modulus (GPa)		Strength (MPa)		Poisson's Ratio
Cortical	3 to 5	Longitudinal	17.9 ± 3.9	Tension	135 ± 15.6	0.4 ± 0.16
				Compression	205 ± 17.3	
		Transverse	10.1 ± 2.4	Tension	53 ± 10.7	0.62±0.26
				Compression	131 ± 20.7	
		Shear	3.3 ± 0.4	Shear	65 ± 4.0	
Trabecular	up to 90	Vertebra	0.067 ± 0.045		2.4 ± 1.6	
		Tibia	0.445 ± 0.257		5.3 ± 2.9	
		Femur	0.441 ± 0.271		6.8 ± 4.8	

Note. Human bone mechanical strength properties with averaged values (Wang et al., 2016).

Ti-6Al-4V alloy is the popular material choice for biomedical implant applications due to its bio-compatibility with the human body. Ti-6Al-4V is also highly corrosion-resistant and has a high strength-to-weight ratio, making it ideal for biomedical implants. However, in its fully dense form, its elastic modulus is about 113 GPa, which is about six times higher than the elastic modulus of the cortical bone when in the longitudinal direction. This will cause a huge elastic modulus mismatch with bone when used as an implant. Cortical bone is the outer hard bone tissue or compact bone that is the strongest part of the bone. The trabecular bone is the inner soft bone tissue that is porous (Wang et al., 2016). A Ti-6Al-4V porous lattice with an elastic modulus close to the value of 17.9 GPa will be good for the biomedical implants of the hip stem to prevent the likelihood of stress-shielding. At the same time, the Ti-6Al-4V porous lattice should also be able to withstand loading forces up to 11 kN for situations of high loading for a hip stem of a person with 100 kg bodyweight and a good cycles to failure for fatigue at about 4 kN of loading forces (Bergmann et al., 2016).

2.1.5 EB-PBF Printability and Powder Removal for Osteoconductive Ti-6Al-4V Lattice

Like any other manufacturing technology, EB-PBF has limitations that need to be considered for printing parts, especially designs with very small features like osteoconductive lattice structures for biomedical bone implants. Based on the review from the previous Section 2.1.3, a lattice with a higher surface area will be beneficial for osteoconduction, which means that the ratio of the surface area of the lattice to the volume of the overall dimension of the lattice structure, *S-V* should be as high as possible. This can be achieved by either selecting a unit cell design with more surface area per overall unit cell volume or reducing the cell size, l_c together with the strut size, d_s and pore size, d_p. Increasing the *S-V* of the lattice structure is also in line with trying to reduce its elastic modulus. However, other than facing the possible issue of the lattice structure not having sufficient mechanical strength to support the necessary load, the additional issues faced would be the difficulty in the printability or manufacturability of the lattice and the ease of powder removal post-print. Therefore, these two factors of EB-PBF printability and powder removal must be considered when selecting the unit cell design and the lattice parameters of the lattice structure for the biomedical bone implant.

The EB-PBF printability factor relates to the minimum strut diameter that can be printed accurately. Smaller strut and cell sizes favour medical implant lattice structure for its higher *S-V* ratio. However, the minimum strut diameter is limited to the minimum melt pool width and depth, which is controlled by the electron beam (e-beam) diameter, speed and power, which are explained in further detail in Section 2.2.2. The minimum e-beam diameter is 140 μm for the Arcam EBM Q10plus machine by GE Additive (General Electric, 2024). Thus, it is theoretically impossible to print strut with sizes that are smaller than 140 μm and have difficulties printing strut diameters less than double the minimum e-beam diameter, as the melt pool width would be larger, and powder would adhere to the melt pool's edge as partially melted powder. This was observed by X. Zhang et al. (2019) in their study, where an Arcam A2 EBM machine with a minimum e-beam diameter of 250 μm was used to print designed strut diameters of 100 μm and 200 μm and produced struts that were oversized, with average sizes of 500 μm to 600 μm.

The other factor mentioned is the powder removal. The Ti-6Al-4V powder is not only the feedstock material in the EB-PBF process but is also used as a medium to provide support while the part is being printed. Hence, unmelted powder in the porous spaces of the printed lattice structure must be removed to ensure that the porous cavity is indeed porous and that no loose powder is present in the porous implant that may cause a medical hazard. Powder removal is

done using the powder removal station (PRS), an abrasive blasting cabinet that uses the Ti-6Al-4V powder as the abrasive medium to blast unmelted powder off the printed parts. The ease of powder removal consideration becomes even more critical as the pore size of the lattice structure is below a millimetre, which makes powder removal even more difficult. Ideally, the arrangement of pores of the lattice cell should provide a clear line of sight to allow unmelted powder to be blown out easily and for visual confirmation of any unmelted powder left (Figure 2.6). A complex lattice structure design with no clear line of sight may be acceptable for larger pore sizes but will fail powder removal for sub-millimetre pore sizes. Current studies have not considered the EB-PBF printability and powder removal factors when selecting the structure's unit cell design and lattice parameters for biomedical bone implant application.

Figure 2.6
Illustration of Lattice Structures for Good and Poor Powder Removal

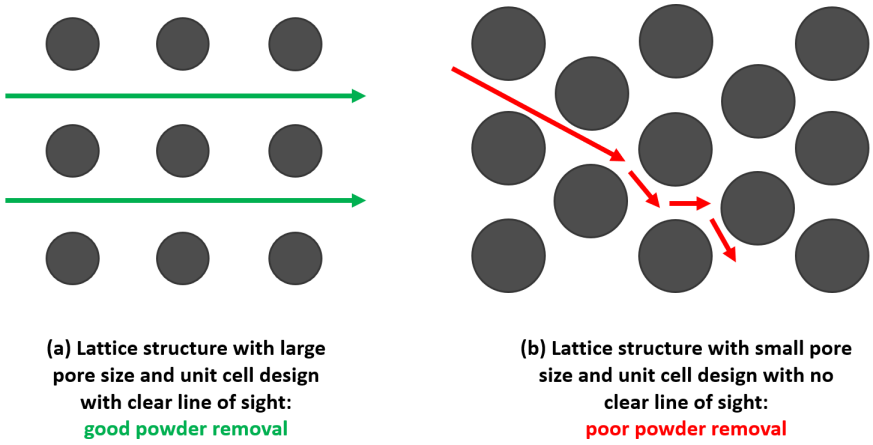

Note. Lattice structure of unit cell design examples with struts spacing, related to pore size d_p and the strut arrangement, related to unit cell design for good and poor powder removal. The illustration shows a cross-section of the strut-based lattice structure. Own work.

2.1.6 Simple Cubic Lattice Parameters for Osseointegration

The lattice parameter directly correlates to the EB-PBF printing process parameters, which is the strut thickness or strut diameter. However, the geometric relationship between the strut diameter, pore size, cell size, pore size and the surface-volume ratio has not been examined in the existing literature. Thus, a geometric expression of the lattice parameters regarding strut diameter must first identify the limits based on the bio-function requirement. The cell design of simple cubic is selected for its simplicity and uniform pore size. This section describes the geometrical relationship between the strut diameter and the other lattice parameters. An octagon-shaped strut is used instead of a circular strut to simplify the geometric calculation with a minimal difference. This is

also used when creating lattice structures using the standard triangle language (STL) file format used for additive manufacturing, as using cylindrical struts with smooth curved surfaces will be difficult to resolve into STL.

Figure 2.7
Simple Cubic Unit Cell Design with Octagon-Shaped Strut

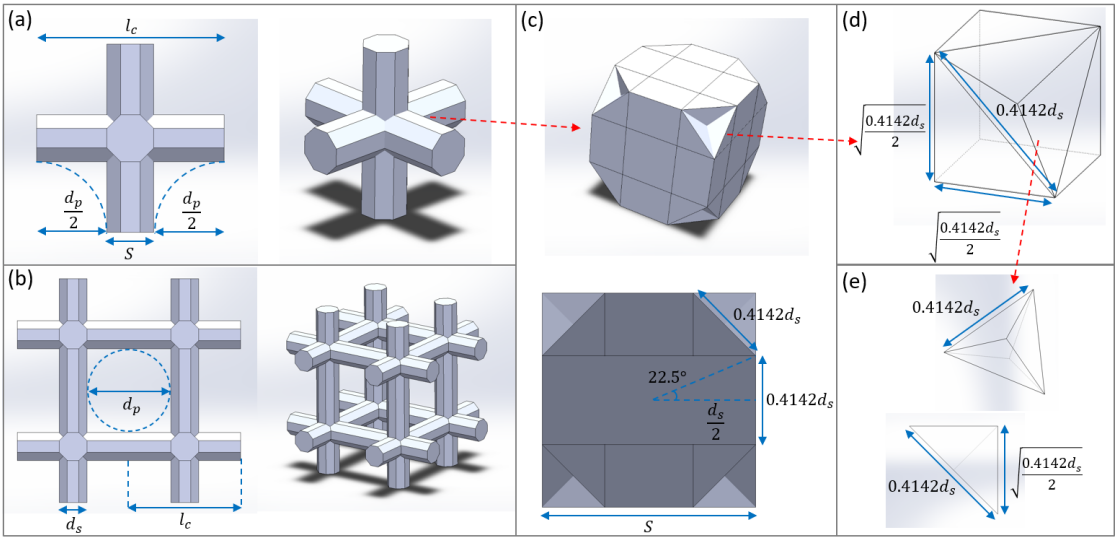

Note. (a) Simple cubic unit cell design. (b) 2×2 cells of simple cubic lattice structure. (c) Node volume of the simple cubic cell. (d) Vertex cube volume of the node volume and (e) vertex void volume. Own work.

As the lattice structure is a topologically ordered structure formed by repeated unit cells, the lattice parameters of the simple cubic lattice structures of porosity and S-V can be calculated based on a single simple cubic unit cell. Based on Figure 2.7, the strut diameter, d_s of a simple cubic unit cell design can be defined as the difference between the cell size, l_c and pore size, d_p (Equation 2.9) and the strut diameter can be expressed as a function of cell size and pore size (Equation 2.10).

$$\textbf{Strut diameter} = (\text{cell size}) - (\text{pore size}) \tag{2.8}$$

$$d_s = l_c - d_p \tag{2.9}$$

$$d_s = f(l_c, d_p) \tag{2.10}$$

The porosity of a simple cubic unit cell can be described as the percentage of void volume to the overall volume of interest. It can also be calculated by taking the difference between one and the relative density (Equation 2.12). The relative density of the simple cubic unit cell is the percentage of the simple cubic cell volume to the unit cell volume. Porosity is selected for calculation over relative density due to the importance of porosity in osteoconductivity. The porosity

of a simple cubic cell can be expressed in the form of its pore size and cell size (Equation 2.14). Therefore, it can be defined as a function of strut diameter (Equation 2.15).

$$\textbf{Porosity} = \left[1 - \frac{\text{(SC cell volume)}}{\text{(unit cell volume)}}\right] \times 100\% \tag{2.11}$$

$$\phi = \left(1 - \frac{V_{c\text{-}L}}{V_c}\right) \tag{2.12}$$

$$\phi = \left(1 - \frac{6d_p(1+\sqrt{2})(0.4142d_s)^2 + d_s^3 - 2(0.2071d_s)^{\frac{3}{2}}}{l_c^3}\right) \tag{2.13}$$

$$\phi = \left(1 - \frac{6d_p(1+\sqrt{2})\left[0.4142(l_c - d_p)\right]^2 + (l_c - d_p)^3 - 2\left[0.2071(l_c - d_p)\right]^{\frac{3}{2}}}{l_c^3}\right) \tag{2.14}$$

$$\phi = f(l_c, d_p) = f(d_s) \tag{2.15}$$

$$\text{SC cell volume} = 6(\text{strut volume}) + (\text{node volume}) \tag{2.16}$$

$$V_{c\text{-}L} = 6V_s + V_n \tag{2.17}$$

$$V_{c\text{-}L} = 6\left[d_p(1+\sqrt{2})(0.4142d_s)^2\right] + \left[d_s^3 - 2(0.2071d_s)^{\frac{3}{2}}\right] \tag{2.18}$$

$$V_{c\text{-}L} = 6d_p(1+\sqrt{2})(0.4142d_s)^2 + d_s^3 - 2(0.2071d_s)^{\frac{3}{2}} \tag{2.19}$$

$$\text{Strut volume} = (\text{strut cross-section area}) \times (\text{strut length}) \tag{2.20}$$

$$V_s = 2(1+\sqrt{2})(0.4142d_s)^2 \times \left(\frac{d_p}{2}\right) \tag{2.21}$$

$$V_s = d_p(1+\sqrt{2})(0.4142d_s)^2 \tag{2.22}$$

From Figure 2.7(c), the node volume can be resolved as a cubic volume with the edge length of the strut size, minus the vertex void volumes, as shown in Figure 2.7(d) and Figure 2.7(e).

$$\text{Node volume} = (\text{centre cubic volume}) - 8(\text{vertex void volume}) \tag{2.23}$$

$$V_n = d_s^3 - 8V_{vv} \tag{2.24}$$

$$V_n = d_s^3 - 8\left[\frac{(0.2071d_s)^{\frac{3}{2}}}{4}\right] \tag{2.25}$$

$$V_n = d_s^3 - 2(0.2071d_s)^{\frac{3}{2}} \tag{2.26}$$

$$\text{Vertex Void Volume} = \frac{1}{4} \times (\text{vertex cube volume}) \tag{2.27}$$

$$V_{vv} = \frac{1}{4} \times \left(\sqrt{\frac{0.4142 d_s}{2}} \right)^3 \tag{2.28}$$

$$V_{vv} = \frac{(0.2071 d_s)^{\frac{3}{2}}}{4} \tag{2.29}$$

The surface area of the SC unit cell can be calculated from the sum of the strut surface area and vertex void surface area (Equation 2.35). A surface area to cell volume ratio can then be described as the calculated SC surface area to the cell volume from the cell size (Equation 2.31). These equations can be expressed in terms of pore size, cell size, and strut size. Since the strut size is a function of both pore size and cell size, then the *S-V* ratio is a function of strut size (Equation 2.33).

$$\textbf{Surface Area-Volume Ratio} = \frac{(\text{SC surface area})}{(\text{unit cell volume})} \tag{2.30}$$

$$S\text{-}V = \frac{A_{sc}}{l_c^3} \tag{2.31}$$

$$S\text{-}V = \frac{24 d_p (0.4142 d_s) + 24 (0.2071 d_s) \left[\left(\frac{1}{2} \sqrt{(0.2071 d_s) + (0.4142 d_s)^2} \right)^2 - (0.2071 d_s) \right]^{\frac{1}{2}}}{l_c^3} \tag{2.32}$$

$$S\text{-}V = f(d_p, l_c) = f(d_s) \tag{2.33}$$

$$\text{SC surface Area} = 6(\text{strut surface area}) + 8(\text{vertex void surface area}) \tag{2.34}$$

$$A_{sc} = 6A_s + 8A_{vv} \tag{2.35}$$

$$A_{sc} = 6 \left[4 d_p (0.4142 d_s) \right] + 8 \left[3 (0.2071 d_s) \left[\left(\frac{1}{2} \sqrt{(0.2071 d_s) + (0.4142 d_s)^2} \right)^2 - (0.2071 d_s)^2 \right]^{\frac{1}{2}} \right] \tag{2.36}$$

$$A_{sc} = 24 d_p (0.4142 d_s) + 24 (0.2071 d_s) \left[\left(\frac{1}{2} \sqrt{(0.2071 d_s) + (0.4142 d_s)^2} \right)^2 - (0.2071 d_s)^2 \right]^{\frac{1}{2}} \tag{2.37}$$

$$\text{Strut Surface Area} = (\text{strut diameter parameter}) \times (\text{strut length}) \tag{2.38}$$

$$A_s = (8 \times 0.4142 d_s) \times \left(\frac{d_p}{2} \right) \tag{2.39}$$

$$A_s = 4 d_p (0.4142 d_s) \tag{2.40}$$

$$\text{Vertex Void Surface Area} = 3(\text{vertex void triangular area}) \tag{2.41}$$

$$A_{vv} = 3 \times \frac{1}{2}(0.4142d_s)\left[\left(\frac{1}{2}\sqrt{\frac{0.4142d_s}{2} + (0.4142d_s)^2}\right)^2 - \left(\frac{0.4142d_s}{2}\right)^2\right]^{\frac{1}{2}} \tag{2.42}$$

$$A_{vv} = 3(0.2071d_s)\left[\left(\frac{1}{2}\sqrt{(0.2071d_s) + (0.4142d_s)^2}\right)^2 - (0.2071d_s)^2\right]^{\frac{1}{2}} \tag{2.43}$$

Based on the strut size, porosity and S-V ratio functions (Equation 2.9, Equation 2.14 and Equation 2.32), graph analysis of the geometric relationship for a simple cubic cell can be generated for the pore sizes of 300 μm, 600 μm and 900 μm, as shown in Figure 2.8. The minimum strut size for the Arcam EBM Q10plus machine that is used for this study is approximately 300 μm and is marked in Figure 2.8(a) (yellow). It can be observed that at that minimum strut size, the lattice structure with 600 μm pore size will have a porosity of about 78 %, while the pore size of 300 μm will yield a poor porosity of below 60 %. However, the *S-V* ratio for the smaller pore size is significantly higher than the pore size of 600 μm.

Alternatively, a good porosity level of 70 % is selected in Figure 2.8(b) (red). The strut size at this porosity level for the pore size of 300 μm is 200 μm, which is lower than the minimum strut size and exceeds the printability of EB-PBF. On the other hand, the strut size for the pore size of 600 μm is at 400 μm, which will be within the printability limit and is at a negligible decrease of *S-V* ratio, from the strut size of 300 μm with the same pore size.

The geometric relationship analysis for the simple cubic unit cell design shows that for smaller pore sizes, strut sizes must be reduced to sizes lower than the printability limit to maintain a good porosity level. Larger pore sizes can achieve high porosity levels and have large strut sizes but have a trade-off of the surface area or lower the *S-V*. While still satisfying the bio-function requirement, the best lattice parameters for a simple cubic unit cell would be a pore size of 600 μm and a strut size range of 300 μm to 500 μm. Selecting the maximum pore size enables the selection of a larger strut size, improving the printability factor for EB-PBF and allowing for good powder removal. Therefore, the lattice parameters of strut size and pore size selection for osteoconductive simple cubic lattice structure considering the EB-PBF printability factor can be summarised below.

- Strut size, d_s=300 μm to 500 μm
- Pore size, d_p=largest possible, better for larger d_s

Figure 2.8
Simple Cubic Unit Cell Geometric Parameters Relationship Graph

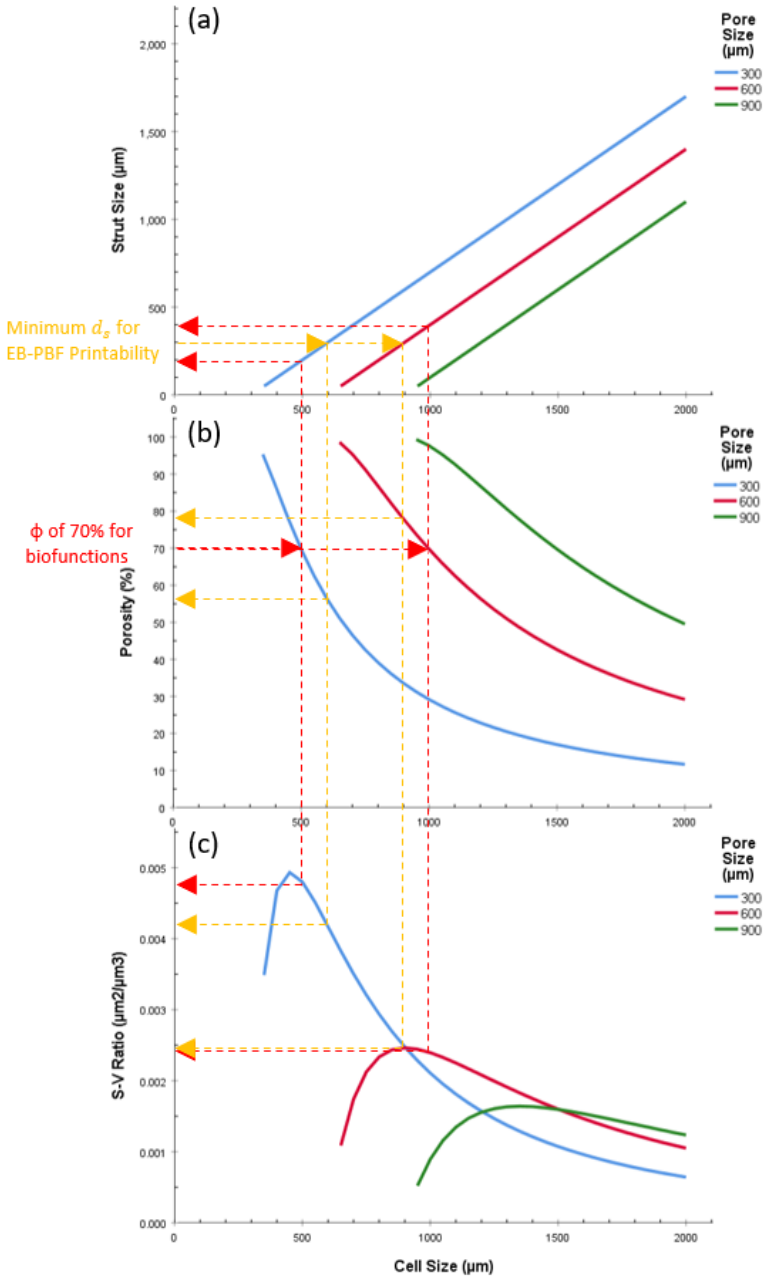

Note. (a) Strut size or strut diameter versus cell size, (b) porosity versus cell size, and (c) *S-V* ratio versus cell size, based on the Equation 2.9, Equation 2.14 and Equation 2.32. Own work.

2.2 Ti-6Al-4V Lattice Printing with EB-PBF

The EB-PBF process, like any other powder bed fusion technology, has a very dynamic printing process where melting and resolidification of metal powder are happening rapidly as the part is being built layer by layer. This section looks into the factors of the EB-PBF process that contribute to the batch variation and print quality for the Ti-6Al-4V lattice structure.

2.2.1 Ti-6Al-4V Alloy and PBF Powder

Titanium alloys are popular for aerospace, marine, automotive and medical applications due to their high strength-to-weight ratio, corrosion resistance and biocompatibility. Among titanium alloys, Ti-6Al-4V or Ti64 is the most used titanium alloy. Ti-6Al-4V exist as a dual $\alpha + \beta$ phase alloy due to the addition of α-stabilising aluminium and β-stabilising vanadium (Figure 2.9). The dual-phase of $\alpha + \beta$ makes Ti-6Al-4V to be high in strength and also high in ductility. Ti-6Al-4V is a highly printable alloy for MAM, primarily due to its short freezing range of approximately 10°C, making it resistant to hot cracking during solidification. It also has excellent mechanical and corrosion properties. These make the Ti-6Al-4V alloy a top choice for 3D printing or additive manufacturing using PBF and other powder-based MAM processes.

Figure 2.9
Ti-6Al-4V Phase Diagram

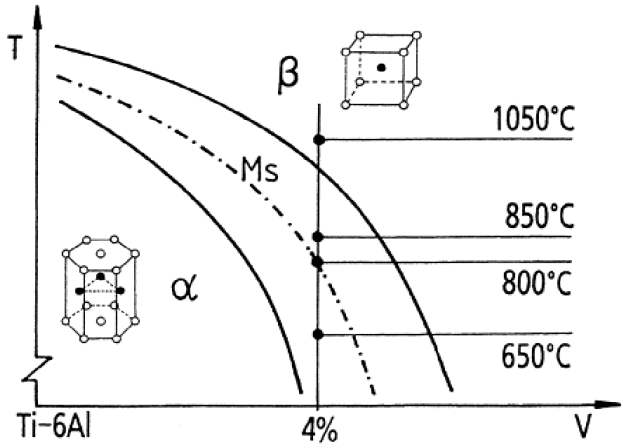

Note. Phase diagram of Ti-6Al-4V alloy showing microstructure composition (Ducato et al., 2013).

The common type of Ti-6Al-4V alloy used commercially in powder form in powder bed fusion metal additive manufacturing is the grade 5 alloy specified by the ASTM F2924-14 standard (ASTM International, 2014b). There is another grade of Ti-6Al-4V alloy with lower oxygen and hydrogen content, which is the extra low interstitial (ELI) grade, and its specification is described

in ASTM F3001-14 standard (ASTM International, 2014a). The difference between these two popular titanium alloys is shown in Table 2.2. The ELI grade is specified to contain a lower maximum amount of oxygen and hydrogen of 0.13 wt.% and 0.012 wt.%, compared to the grade 5 alloy of 0.20 wt.% and 0.015 wt.% respectively, in its chemical composition. The lower interstitial levels in ELI grade provide better ductility, fracture toughness, and fatigue strength. The oxygen element is an α phase stabiliser (Figure 2.10) and can increase the hardness and brittleness of Ti-6Al-4V alloy, which in turn reduces its fracture toughness (Yan et al., 2014). The lower oxygen level in the ELI grade decreases the hardness and increases the elastic modulus and ductility of the Ti-6Al-4V alloy. On the other hand, hydrogen content in the Ti-6Al-4V alloy causes the flow of stress to increase, causing the lowering of fracture toughness (Shan et al., 2008; Shaoqing & Linruo, 1995; Zong et al., 2007). The lower hydrogen levels in the ELI grade contribute to the higher fracture toughness.

Figure 2.10
Alloying Elements Effects on the Phase Diagram of Titanium

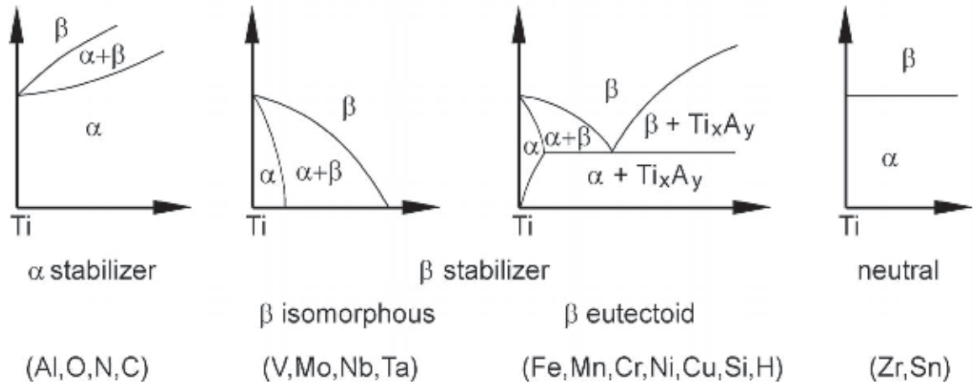

Note. Types of alloying elements for titanium and their effect on the phase diagram (Lütjering & Williams, 2007).

Powder reuse. In EB-PBF printing, it is common to recycle unmelted powder from previously completed build jobs. This is done mainly due to cost factors, where using a powder batch with fully virgin powder for every build will not be economically viable, especially for an expensive alloy like Ti-6Al-4V. The amount of powder required for a specific build part depends on the height of the designed part because each build layer must be filled with powder to support subsequent build layers. This means that a large amount of powder is required for a small build part, and a large fraction will be unmelted. On the other hand, to fully utilise the production capacity of the EB-PBF machine, the full amount of powder to fill the build tank is required. The powder cycle for EB-PBF with a filled build tank is illustrated in Figure 2.12. A batch of virgin powder may be used initially for the first build job or batch. After the build process, the built part and unmelted

powder will be transferred into the powder recovery station (PRS) to remove unmelted powder from the built part. The unmelted powder goes through a sieve mesh in the PRS to remove the large agglomerated powder, and the recovered powder is then collected for powder blending. The additional virgin powder will be added to the recovered unmelted powder to produce the same amount of powder for a filled build tank, and the resultant powder will be blended to ensure even distribution before being used again in the EB-PBF for the next build job.

Table 2.2
Ti-6Al-4V Alloy Powder Composition for PBF

Element	Ti-6Al-4V ELI[a] (wt.%)		Ti-6Al-4V Grade 5[b] (wt.%)	
	min	max	min	max
Aluminum	5.5	6.0	5.0	6.5
Vanadium	3.5	4.5	3.5	4.5
Iron	-	0.25	-	0.25
Oxygen	-	0.13	-	0.20
Carbon	-	0.08	-	0.08
Nitrogen	-	0.05	-	0.05
Hydrogen	-	0.012	-	0.015
Yttrium	-	0.005	-	0.005
Other, each	-	0.1	-	0.1
Other, total	-	0.4	-	0.4
Titanium	remainder	-	remainder	-

Note. Specification for the composition of Ti-6Al-4V alloy powder for powder bed fusion metal additive manufacturing by [a]ASTM International (2014a) and [b]ASTM International (2014b).

There is an advisable maximum number of reuse by PBF powder suppliers because the powder properties will change with every reuse cycle and will be out of specification, and the effects on the part quality are not fully understood. Thus, the unmelted powder will be disposed of at the maximum reuse cycle. The effects of powder reuse on the powder properties can be categorised into morphology, chemical composition, and microstructure (Sutton et al., 2017). The change in properties is due to environmental exposure during material handling, mechanical forces, and thermal energy exposure during printing. Chemical composition change is significant in specially reactive metal powder, like Ti-6Al-4V powder, which, in turn, also affects the microstructure of the powder.

Powder reuse in PBF is essential in an industrial setting to increase the economic viability of the manufacturing process and reduce waste in both energy and material. Thus, it is important to understand powder-part properties fully. Figure 2.11 shows the categorical relationship between the powder and part properties. According to Sutton et al. (2017), the powder properties for PBF

can be categorised into three properties of morphology, chemistry and microstructure, as shown in Figure 2.11, and these affect the performance of the powder when used in PBF, which ultimately affects the part properties.

Figure 2.11
Powder Properties Classification for Additive Manufacturing

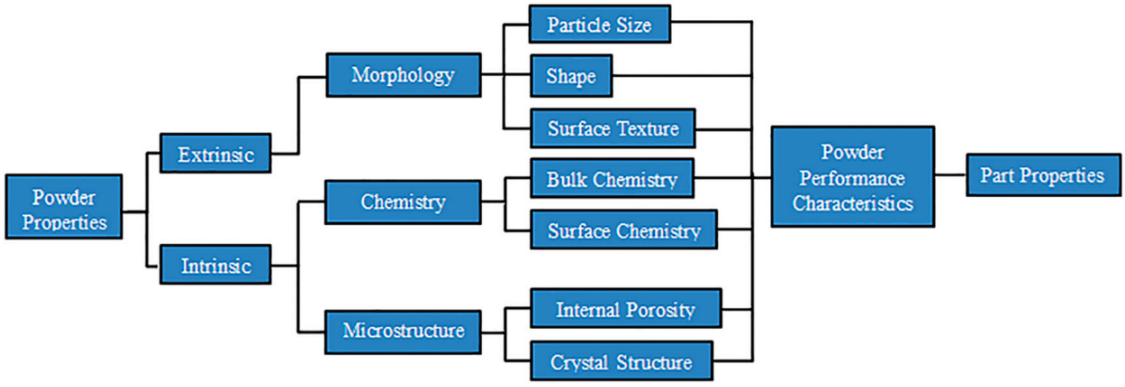

Note. Three main classifications of powder properties of morphology, chemistry and microstructure for metal powder used in additive manufacturing (Sutton et al., 2017).

Although there are studies done for investigating the effect of powder reuse on the powder properties of Ti-6Al-4V in PBF, most are done in limited reuse cycles and focus on the reusing of a single powder batch without blending of additional virgin powder that results in a mixture of powder fractions at different reuse powder cycles as shown in Figure 2.12 (Alamos et al., 2020; Cordova et al., 2019; Montelione et al., 2020). The study by Denti et al. (2019) was among the few research studies investigating the powder reuse effect using blended additional virgin powder with the unmelted powder batch. Their study used the L-PBF and reached a maximum of 100 reuse cycles. The study by Popov et al. (2018) examined the effect of reusing Ti-6Al-4V powder in EB-PBF and found that using reused powder causes more defects in the built part and causes a wider variation in mechanical strength.

Powder morphology change. The morphology property of change with powder reuse for Ti-6Al-4V in PBF has been studied extensively, and the characteristics found are particle size, shape and surface texture (Sutton et al., 2017). The morphology property is important as it affects the flowability and packing density of the powder, which determines the quality of the powder bed layer during the raking process. A powder that has difficulty flowing can cause an uneven spread of powder, and a lower packing density can cause higher porosity defects in the built part (Nandwana et al., 2018). Ti-6Al-4V powder, produced either by gas-atomisation or plasma-atomisation, is spherical and relatively smooth (Figure 2.13(a)). The particle size of the powder is generally examined in terms of particle size distribution (PSD) and average particle size. Studies of powder

reuse in both L-PBF and EB-PBF have commonly reported a narrowing of the PSD after cycles of reuse (Alamos et al., 2020; Carrion et al., 2019; Ghods et al., 2020; Quintana et al., 2018; Schur et al., 2020; Sun et al., 2018; Tang et al., 2015). On the other hand, only Denti et al. (2019) reported that the PSD has shifted to the finer side, which can be attributed to the blending of additional virgin powder to the recovered used powder.

Figure 2.12
EB-PBF Ti-6Al-4V Powder Cycle for Industrial Production Application

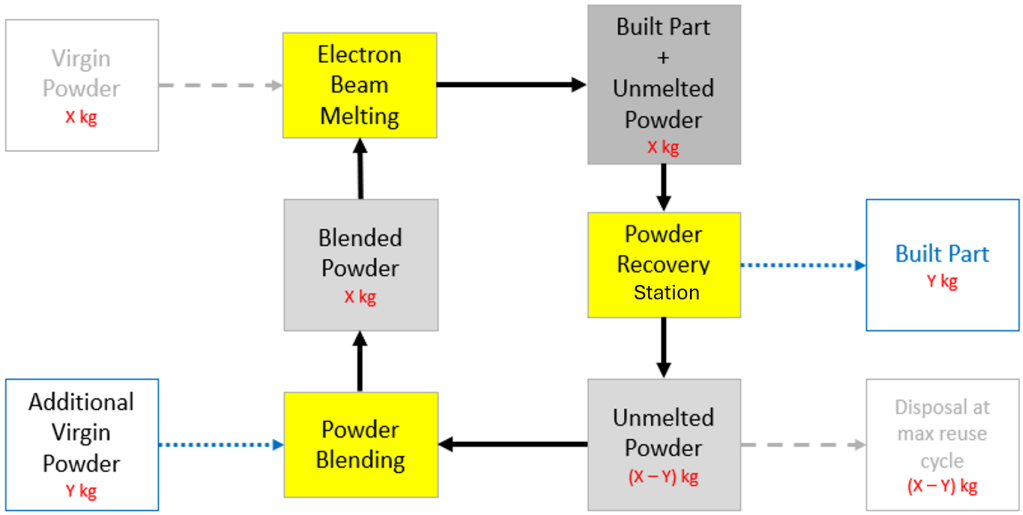

Note. Ti-6Al-4V powder cycle in EB-PBF for a production application. Initially, fully virgin powder will be used for the first build batch. Subsequent build batches will have additional virgin powder added to the unmelted powder from the previous build batch while ensuring the oxygen content is within specifications. The unmelted powder is also disposed of after maximum reuse times. Own work.

The Ti-6Al-4V powder particle shape and surface texture change with reuse cycles due to the exposure to high thermals during processing and mechanical impact from blasting in the PRS. Popov et al. (2018) observed shape and surface texture defects on the powder reused for 69 cycles, as shown in Figure 2.13. Quintana et al. (2018) found that after the 17th reuse cycle, the powder has fewer satellites, and the particle surface is rougher. The reduction of satellites was credited to the authors' higher flowability of the reused powder. Carrion et al. (2019) also reported a drop in satellites in the powder after powder reuse of 15 cycles and found that the flowability also improved with reused powder. Satellites, as shown in Figure2.13(c), in the powder are noted to be present from the supplied virgin powder and not due to the recycling of powder (Popov et al., 2018). Although the particle shape change of reduction of satellites in reuse powder has been observed to improve flowability, the number of reuse cycles is low. It is noted that the other types of particle shape defects are only more prominent in a higher number of cycles, as mentioned by Alamos et al. (2020), the morphology change in Ti-6Al-4V powder is only significant after 20 or

more reuse cycles. Thus, the effect of particle shape defects on flowability is only noticeable at higher reuse cycles, as mentioned by Popov et al. (2018). However, these are based on a power cycle that utilises a single powder batch without adding virgin powder between cycles. On the other hand, the study done by Denti et al. (2019) with a reuse cycle of 100 cycles and adding virgin powder between cycles found that the flowability did not decrease with such high reuse cycles but improved. They also observed the presence of satellite particles and agglomerated powder post-PRS. Tap density was examined by Quintana et al. (2018) and Tang et al. (2015), and both found that the tap density decreases with powder reuse of 31 and 21 cycles, respectively. The effect on tap density of the reused powder was not tested by Denti et al. (2019).

Figure 2.13
Morphological Changes and Defects in Reused Powder

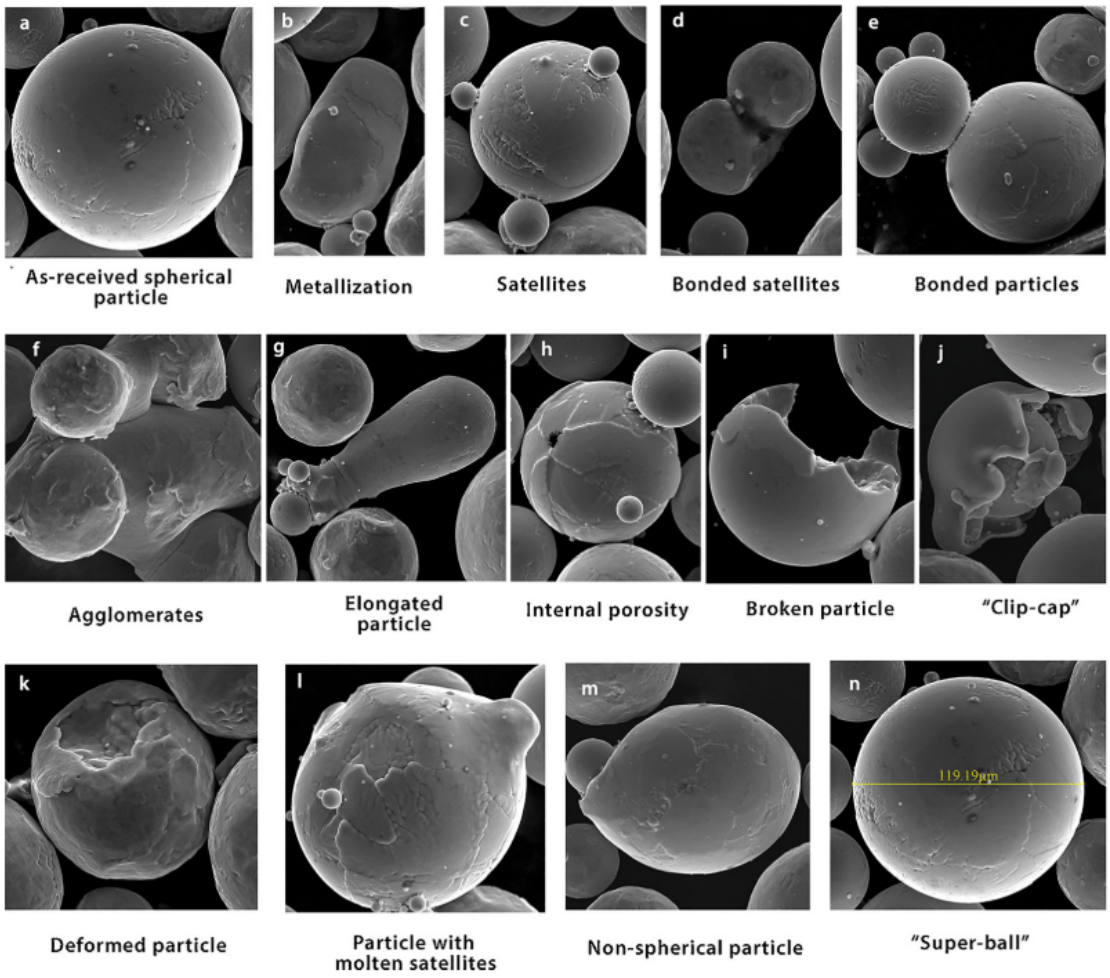

Note. Types of morphological changes and defects observed in reused powder by Popov et al. (2018).

Microstructure and chemical composition change. Montelione et al. (2020) compared the microstructure of Ti-6Al-4V virgin power and reused powder of 30 cycles. They found that the virgin powder contains α' martensite, which is similar to forged Ti-6Al-4V with annealing and

quenching, while the reused powder shows microstructures of α' and coarse $\alpha + \beta$. The change in some of the reused powder is attributed to exposure to the thermal cycle during printing. However, the powder's microstructure does not significantly affect the final microstructure of the built part, as the PBF is a melting process. The change in the powder's chemical composition is more significant than that of the powder microstructure, affecting the printed part's microstructure and chemistry composition. Two types of chemical composition change in reused PBF powder are bulk chemistry and surface chemistry. In Ti-6Al-4V, the chemical composition change is expected to occur mostly on the surface of the recycled powder particle.

Figure 2.14

Chemical Composition Change of Reused Ti-6Al-4V Powder in EB-PBF

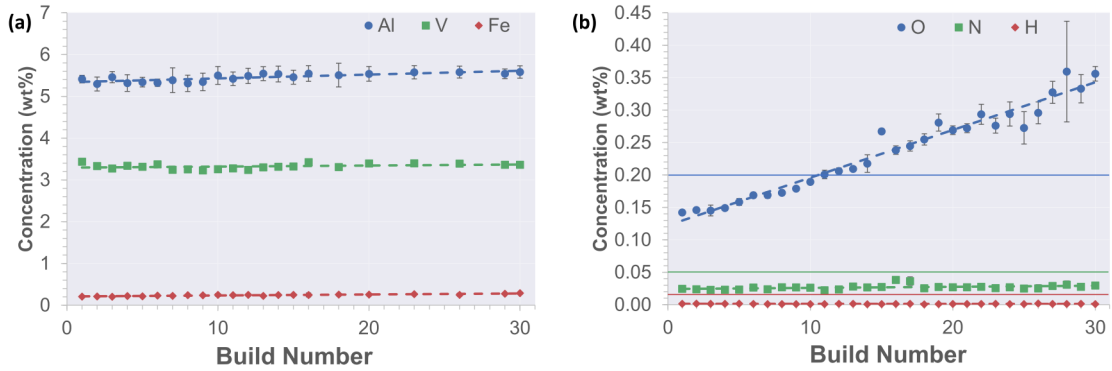

Note. Chemical composition change of the Ti-6Al-4V powder over the number of builds in EB-PBF (Ghods et al., 2020).

Titanium alloys, like Ti-6Al-4V, have a high affinity with oxygen to form titanium dioxide, TiO_2, on the surface (Lütjering & Williams, 2007). Grell et al. (2017) noted that an oxygen-rich α case forms on the Ti-6Al-4V powder particle after artificially oxidising it for four hours in the air at 650 °C. However, the α case was not visible in particles with five cycles of powder reuse due to the slight increase in oxygen content of 0.032 wt.% from 0.11 wt.%, compared to the high levels of 0.340 wt.% and 0.525 wt.% for the artificially oxidised powders. It is known that for Ti-6Al-4V powder, the composition of aluminium and vanadium alloying elements and interstitial elements, other than oxygen, remains relatively stable after powder reuse cycles. Tang et al. (2015) have looked into the change of powder composition with reuse times of up to 21 in EB-PBF and found that the V and Al content remained relatively stable, while the oxygen content increased from 0.08 wt.% to 0.19wt.%. A similar observation was also noted by Ghods et al. (2020), where not only vanadium and aluminium but also iron, hydrogen and nitrogen compositions remained relatively the same for over 30 reuse cycles, and only oxygen content increased significantly after each reuse cycle (Figure 2.14). For Ti-6Al-4V in L-PBF, similar element changes with powder reuse were

also observed. An increase in oxygen and no change in nitrogen, aluminium and vanadium was reported by Quintana et al. (2018).

The increase of oxygen content in reused Ti-6Al-4V powder is attributed to the exposure of the powder to moisture from atmospheric air during handling outside of the vacuum build chamber and during its processing of the PRS. The oxygen in the moisture then interacts with the powder particles when the powder is reused in the PBF machine. Thus, the oxygen content will rise as the total number of reuse cycles increases. Consequently, the printed part will also have a higher oxygen content than the initial oxygen levels of the powder before the build process, as seen by Quintana et al. (2018) and Tang et al. (2015). Therefore, for the industrial production powder cycle mode of Ti- 6Al-4V, blending the additional virgin powder with reused powder will result in the built part with a lower oxygen level than the initial reused powder and can still conform to the industry standard requirement levels.

Effects of oxygen content on the tensile properties of the Ti-6Al-4V EB-PBF part were studied. Generally, it was reported that the yield strength and ultimate tensile strength increase with higher oxygen levels, while elongation and reduction of area decreases (Amin Yavari et al., 2013; Popov et al., 2018; Tang et al., 2015). This was also true for the tensile test on the Ti-6Al-4V EB-PBF part with increased oxygen content heat-treated by hot isostatic pressing (HIP) (Popov et al., 2018). Impact toughness properties were also studied by Grell et al. (2017), and it was found that the Charpy absorbed impact energy dropped intensely when the oxygen level increased from 0.13 wt.% to higher than 0.27 wt.%. The same researchers also conducted a hardness test, and the hardness rose as the oxygen level increased.

Reusing unmelted powder can contribute to the variation between build batches in an industrial production setting based on the change in morphology, microstructure and chemical composition of the Ti-6Al-4V powder. Therefore, this EB-PBF batch variation effect should be examined, especially for Ti-6Al-4V parts with very small features, such as the porous lattice structure.

2.2.2 EB-PBF Printing Parameters

The electron beam melting and build process in the EB-PBF involves an e-beam as its heat source for melting, and an illustration of it is shown in Figure 2.15. The e-beam is accelerated with a constant voltage acceleration, U, of 60 kV and together with the beam current, I, constitutes the e-beam power, P. Another e-beam parameter is the beam diameter, $\varnothing$ and is controlled by the focusing lens in the e-beam column. The beam diameter controls the sharpness of the beam, whereas the smaller beam diameter has a sharper and focused beam energy. Conversely, a larger

beam diameter will have a less focused and diffused beam energy. The control setting for this in the Arcam EBM Q10plus machine is the focus offset (*FO*), and this is a relative setting that does not correspond directly to the actual beam diameter (Equation 2.44). The unit value of this setting is in mA, and the minimum setting of 0 mA is the relative smallest and sharpest e-beam diameter.

$$FO = f(\varnothing) \tag{2.44}$$

$$SF = f(v, I) \tag{2.45}$$

Figure 2.15
Illustration of the Melt and Build Process of EB-PBF

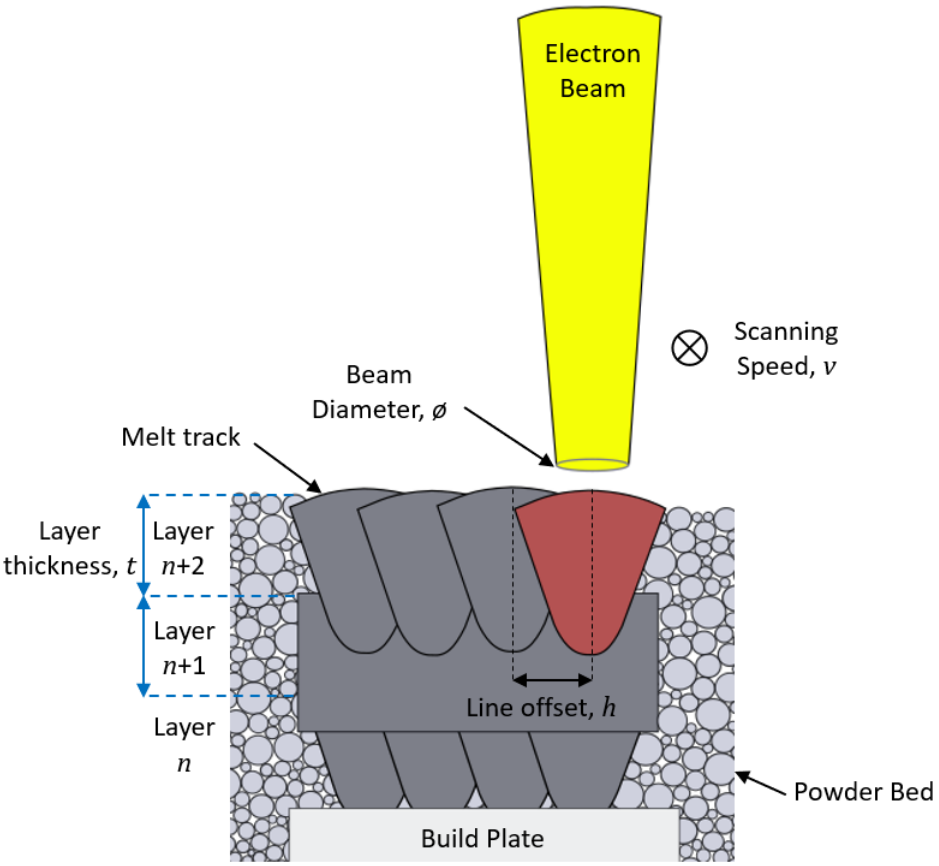

Note. EB-PBF melting and build process parameters. The illustration shows a 90° scan strategy for its scan line for the melting process. Own work.

To melt the powder, the e-beam scans the predetermined shape in overlapping lines called the melt track or scan line. The distance between the edges or centres of the two consecutive scan lines is the line offset, h and the speed at which the e-beam moves along the scan line is the scanning speed, v. Similar to the beam diameter setting of *FO*, the scanning speed is also controlled by a relative setting of Speed Function (*SF*) in the Arcam EBM Q10plus machine. Unlike *FO*, *SF* does not have a unit value and is the relative setting that simultaneously controls both the scanning

speed, v and beam current, I (Equation 2.45)

The height of fresh powder spread on the subsequent layer is layer thickness, t and is determined by the height at which the build plate lowers. The scan line direction is altered after each layer to avoid delamination and improve fusion between successive layers, which is the scanning strategy. The scanning strategy shown in the illustration in Figure 2.15 is a 90° raster scan, where the scanning lines are rotated by 90° for each subsequent new build layer. Other than the rotation of the scan lines, the scanning strategy also involves different scanning patterns. The snake and raster scans are two of the most common, illustrated in Figure 2.16. The schematic illustration of the melt pool during a scan melt process in EB-PBF is shown in Figure 2.17. The melt pool forms when the combination of e-beam parameters of I and FO is set to the melt values by the EB-PBF machine controller, and the melt pool moves together with the e-beam that moves at the scanning speed set by the SF parameter. As the melt pool moves, the melt track left behind begins to cool down and solidify. The melt pool geometry is defined by its width w_m and depth h_m.

Figure 2.16
Illustration of the Types of Scan Strategies for EB-PBF

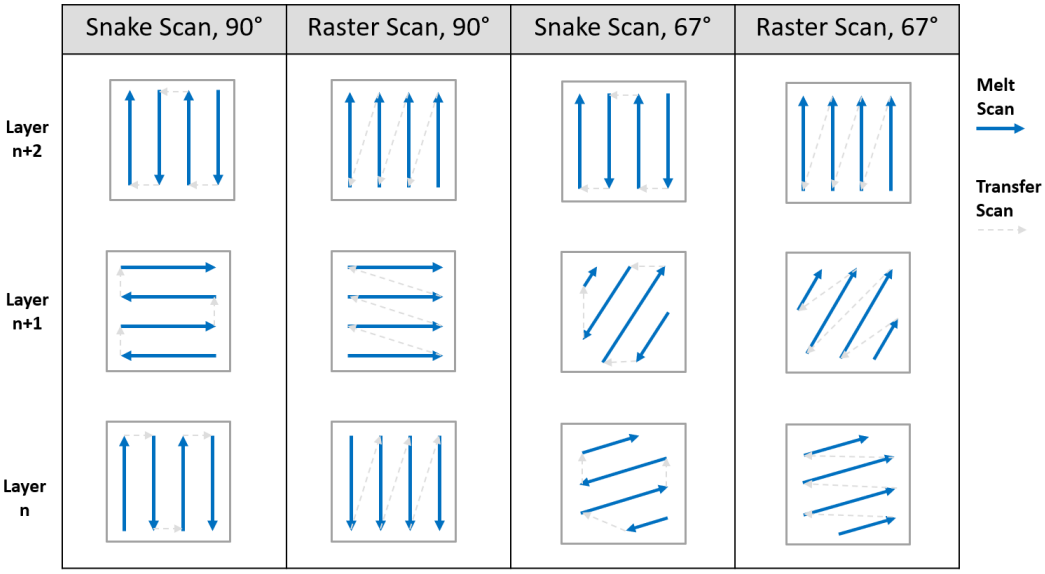

Note. Common scan strategy used in scan lines for the melt process in EB-PBF. Own work.

Assuming the smallest printable strut size, d_s by EB-PBF for osteoconductive lattice structures, only one pass of scan line by the e-beam would be required for melting the strut for a given build layer. Therefore, the melt pool's width is the minimum strut size, $d_{s\text{-}e}$. However, the resulting strut size is always larger than the melt pool width due to powder partially melting at the boundary of the melt pool and sticking to the resolidifying melt track. The partially melted powder at the boundary of the melt pool also causes the surface roughness of the strut. The inconsistency

of the melt pool width affects the actual strut size and can be significantly smaller than the outer strut size, $d_{s\text{-}o}$. Therefore, melt pool geometry control becomes crucial for determining the final geometry of the strut and its surface profile (surface roughness), especially for strut sizes that are equal to or less than double the minimum beam diameter.

Besides the melt pool width, its depth also contributes to the resultant printed strut size. The melt pool depth is affected by the e-beam current (and power), beam diameter (*FO*) and scanning speed (*SF*), and usually is less than the melt pool width (Riedlbauer et al., 2017). Like the melt pool width, the melt pool depth can be irregular and is affected by the melt pool stability. The actual strut size or effective strut diameter, $d_{s\text{-}e}$ is the minimum strut size that is fully solid, and the outer strut size, $d_{s\text{-}o}$, is the largest strut size for a given strut length (Figure 2.17). The scanning speed, v (*SF*), also influences the melt pool geometry. The study by (Jamshidinia et al., 2012) found that increasing the v decreases the melt pool width and depth. This is attributed to reduced heat energy input as the e-beam has less dwell time for a particular spot, and the heat energy is distributed over a longer scan line. Conversely, a lower v will increase the melt pool width and depth.

Figure 2.17
Illustration of the Melt Scan Process for EB-PBF

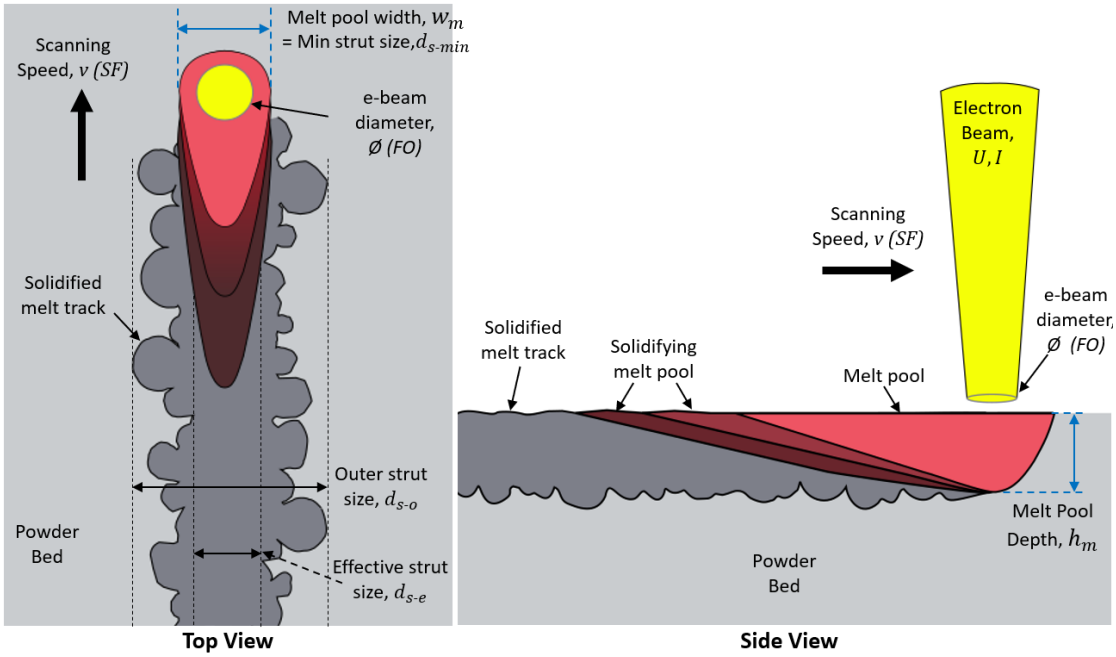

Note. EB-PBF melt scan process parameters, showing a single scan line or melt track for a small strut from the top and side views. Own work.

The staircase effect is another factor other than melt pool stability, which affects the surface roughness and print quality of the lattice structures with small struts printed with EB-PBF. The

staircase effect occurs when the printed part has an inclined feature or surface that causes the melt for each build layer to be slightly shifted due to the resolution of the build layer thickness. Typically, the staircase effect is not pronounced when printing parts using PBF because the part's dimensions are much larger than the jagged melted layers at the inclined surfaces. The surface of the large part might be a little rough, but the overall dimension of the printed part is still relatively accurate. However, the staircase effect becomes significant when printing small features such as struts with small d_s, as found by Harrysson et al. (2008) and shown in Figure 2.18.

Figure 2.18
Illustration of the Staircase Effect for PBF Strut Printing

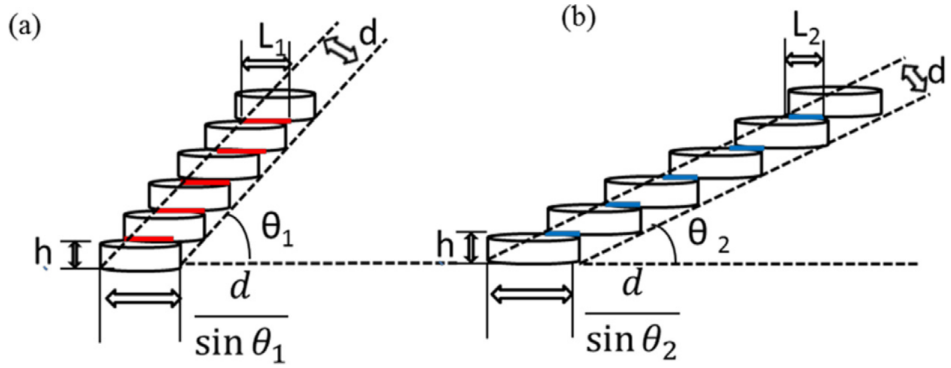

Note. Staircase effect when printing small-size struts using PBF due to the layer-by-layer building process by X. Z. Zhang et al. (2018), based on the study by Harrysson et al. (2008). The strut in (a) is at a higher angle relative to the build plate than the strut in (b).

The small strut size required for osteoconductive lattice structure makes it a challenging print for the EB-PBF due to the more significant influence of the dynamic melt pool parameters and the staircase effect. The surface roughness and print quality of the lattice structure would be much more sensitive to the slight variations in the dynamics of the melt pool parameters during the printing in EB-PBF, as well as the orientation of the unit cell or strut relative to the build direction due to the staircase effect. Therefore, the variation between batches or the batch variation effect for osteoconductive lattice structures needs to be examined for its effect on mechanical behaviour.

2.2.3 Batch Variation in Ti-6Al-4V Printing with EB-PBF

The factors contributing to batch variation for osteoconductive lattice structures have been discussed in Section 2.2.1 and Section 2.2.2. The combination of the unit cell and lattice parameter limitation to meet the requirements for osteoconductive lattice has made it challenging to print with EB-PBF. The summary of the factors that make the batch variation factor crucial for osteoconductive lattice is as follows.

- Powder reuse is integral for industrial production settings when using EB-PBF, which causes changes in morphology and chemical composition variation in the powder.
- The effects of Ti-6A-4V powder reuse are known to affect the mechanical properties of printed solid parts from chemical composition changes and more internal defects.
- The osteoconductive lattice structures printed by EB-PBF can be assumed to be more affected by the Ti-6Al-4V powder reuse due to the small strut sizes.
- The small struts for osteoconductive lattice structure make the surface roughness and print quality more sensitive to melt pool parameters and staircase effect, which also relate to unit cell orientation.

Therefore, the batch variation factor is important to study for Ti-6Al-4V osteoconductive lattice structure printed by EB-PBF for its effect on the mechanical properties under quasi-static and cyclic loading.

2.3 Mechanical Behaviour of Ti-6Al-4V Lattice Printed with PBF

2.3.1 Quasi-static Compressive Behaviour

Many studies have examined the quasi-static mechanical strength of metal porous lattice structures made from electron beam powder bed fusion (EB-PBF) and laser powder bed fusion (L-PBF). There is no standard currently available for the mechanical testing of lattice structures. Therefore, studies have adopted the standard BS ISO 13314:2011, which is a guide for compressive testing of porous and cellular metals with stochastic structures (British Standards Institution, 2012). The most common specification that is followed in this standard is for the guide for the dimension of the overall lattice structure specimen, where the overall lattice diameter or the width of the rectangular specimen is at least 10 times the average pore size of the cellular structure, to minimise the edge effects, and should be not smaller than 10 mm. The length or height of the specimen, which is parallel to the loading direction, should be between one and two times the specimen's diameter or width. The specification for a cylindrical specimen, recommended over the rectangular, is shown in Figure 3.1.

The compressive loading mode of quasi-static mechanical testing is typically chosen over the tensile loading mode, most probably due to its simplicity in testing lattice structures and following the BS ISO 13314:2011 standard. Specimens for quasi-static compressive tests do not require special ends that can be attached to the machine tester to be printed with the lattice. Instead, solid

plate attachments are used on the machine tester, and compressive loads can be applied directly to the bare lattice. However, the choice for compressive loading mode may also be selected based on the intended application of the porous lattice structures, such as biomedical bone implants of hip stems that are predominantly subjected to compressive loading. The BS ISO 13314:2011 standard also specifies the constant crosshead speed for the quas-static compression test, which is calculated from the initial compressive strain rate of between 10^{-3} s^{-1} to 10^{-2} s^{-1} (British Standards Institution, 2012).

Several factors were identified by studies that affect the quasi-static compressive strength of lattice structures made with PBF. The factors are unit cell design, relative density, the material used for the lattice, build direction, print quality and defects, and post-print processing (du Plessis et al., 2022; R. Liu et al., 2023; Zadpoor, 2019). Unit cell design or cellular architecture has been well-established to have a major effect on the mechanical behaviour of the lattice structure under quasi-static compression. As discussed in Section 2.1.1, there are generally three types of unit cell designs, which are strut-based, skeletal-TPMS based, and sheet-TPMS based (Figure 2.2). Also, as mentioned in Section 2.1.2, each unit cell design will have a mix of bending and stretching deformation modes (Figure 2.4). The dominant deformation mode will dictate the mechanical performance of the unit cell design and lattice structures under quasi-static compressive loading, with the dominant stretching deformation mode being stronger and having a higher elastic modulus than bending dominated (Deshpande et al., 2001).

TPMS-based unit cell design has gained more and more attention for its potential to yield better mechanical performance than strut-based design and was explored by Alabort et al. (2019), Ataee et al. (2018), Bobbert et al. (2017), F. Liu et al. (2018), Yánez et al. (2016, 2018) and Yang et al. (2018, 2019). Their improved mechanical properties, when compared to strut-based unit cell design, are commonly attributed to the smoother transition between the nodes and struts of the skeletal-TPMS lattice structure. Although skeletal-TPMS based cell design has been found to have better mechanical performance than strut-based (Al-Ketan et al., 2018), its TPMS features can become less pronounced as the strut size and pore size are at the sub-millimetre level, especially when using EB-PBF with a minimum e-beam diameter of more than 200 μm (Ataee et al., 2018). Also, both TPMS-based cell design types of skeletal and sheet at the sub-millimetre size will fail the requirement of powder removal, as discussed in Section 2.1.5, due to their complex structure, making the powder removal difficult, especially when having pore sizes of 300 μm to 600 μm. Therefore, a simple strut-based cell design is still favourable for producing osteoconductive lattice structures with sub-millimetre strut and pore sizes using EB-PBF.

The relative density or porosity, as discussed in Section 2.1.2, is well understood to affect the overall mechanical strength of the porous lattice structure made with PBF. This relationship can be characterised using the Gibson-Ashby model (Gibson & Ashby, 1997), where the mechanical strength of the lattice structure increases as its relative density increases or the porosity decreases. The unit cell and lattice parameters of unit cell design, cell size, and strut diameter affect the relative density or porosity of the overall lattice structure. However, the relative density is usually adjusted by changing the strut size and pore size when studying the relative density effect on the mechanical strength of the lattice. Studies have shown that increasing the relative density of the lattice structure generally increases the mechanical strength as described in the Gibson-Ashby model (Ahmadi et al., 2015, 2018; Alabort et al., 2019; Barba et al., 2019; Hedayati et al., 2018; Parthasarathy et al., 2010; Yang et al., 2018; C. Zhang et al., 2020).

The relative density of the lattice structure discussed above is of the uniformly graded type, where the relative density is uniform throughout the lattice structure design. Another design technique relating to varying the relative density is by non-uniform relative density, or functional grading, which is gradually varying the relative density or porosity of the lattice structure by changing either the unit cell size, pore size or strut size, aiming to improve the overall mechanical performance. It was found that functional grading of porosity or strut thickness in the direction perpendicular to the loading direction only improves the mechanical performance, which can be attributed to the increase in the overall relative density (Surmeneva et al., 2017). While functional grading along the loading direction has a smaller effect on the mechanical strength (F. Liu et al., 2018; Wu et al., 2018) Nevertheless, the functional grading technique is challenging to apply on osteoconductive lattice structures for biomedical bone implants, as the pore sizes have to be 300 μm to 600 μm for optimum osteoconductivity.

The literature has also considered different bulk materials used to print porous lattice structures using PBF. Among the common materials studied are stainless steel 316L, AlSi7Mg, Co-Cr, IN718, NiTi, Ti-2448, CP-Ti and Ti-6Al-4V. The mechanical properties of the lattice structure generally follow the mechanical properties of its bulk material when compared with the same relative density and unit cell design (R. Liu et al., 2023). However, for lattice structures with specific applications, such as biomedical bone implants, the choice of material is limited to titanium and its alloys, such as CP-Ti and Ti-6Al-4V, with the latter being the preferred choice.

Other factors that the literature found to have an effect on the quasi-static compressive strength of lattice structures are print quality or defects, which are also related to the build direction. The print quality is the combination of the surface roughness of the lattice printed and the geometric

accuracy of the lattice relative to its design. The build direction plays a role in the print quality, where the closer the strut is angled perpendicular to the build direction, the more inaccuracy will be introduced. An angled strut relative to the build direction will also have a rougher surface due to the staircase effect. The quasi-compressive strength of lattice structures is lower when there is a higher surface roughness and defects. There are also defects, such as internal pores and unmelted voids, as discussed in Section 2.2.1, but mainly were studied for their effect on solid Ti-6Al-4V.

Lastly, the factor of post-print processing has also been found to affect the mechanical strength of the lattice structures in literature. The common post-print processing is heat treatment of the lattice structure, which is especially beneficial for lattice structures printed by L-PBF. This is due to the characteristics of the L-PBF process, where the printed parts will have residual stress due to the lack of preheating. Unlike the EB-PBF process, where there is a preheating process that helps relieve the residual stress. Therefore, lattice structures made with L-PBF will have better mechanical properties after heat treatment.

2.3.2 Compression-Compression Fatigue Behaviour

Literature has also examined the fatigue behaviour of porous lattice structures made with electron powder bed fusion (EB-PBF) and laser powder bed fusion (L-PBF). More studies have been done for the quasi-static compressive mechanical test than the fatigue test (Benedetti et al., 2021). Similar to the quasi-static compressive studies, no current standard is available for performing force-controlled constant amplitude axial fatigue tests on metal porous lattice structures made using powder bed fusion. The same BS ISO 13314:2011 standard is adopted as a guide for the specimen dimensions of the lattice structure for the fatigue test study, as shown in Figure 3.1. A large percentage of the fatigue test studies were done in compression-compression mode and similar to the favouring of quasi-static compressive tests, this is also most likely due to the simplicity of compression-compression fatigue tests that do not need the printing of extra ends that can be gripped by the test machines for tensile cyclic loading.

Although more and more recent studies have begun to examine the fatigue strength of lattice structures with fully reversible fatigue loading and tensile-tensile loading mode. It is argued that the tension loads would cause an opening type of fatigue crack growth, which would be much more detrimental to the fatigue strength of the lattice. However, a fatigue test with a tensile loading component of either tension-tension or tension-compression is more complicated than compression-compression due to the tendency of the lattice structure to fracture at the struts that are directly attached to the solid ends, which is caused by the stress concentration at the abrupt

change from solid to porous structures (Zadpoor, 2019). This can be resolved by applying a $\bar{\rho}$ grade or a gradual change of $\bar{\rho}$ between the lattice structure and the solid ends so that the change between the solid and lattice is not abrupt, as shown in Figure 2.19. However, it will complicate the analysis and make it difficult for the results to be applied to a uniform or non-graded lattice structure.

Figure 2.19
Graded Lattice Specimens CAD for Tension-Tension Fatigue

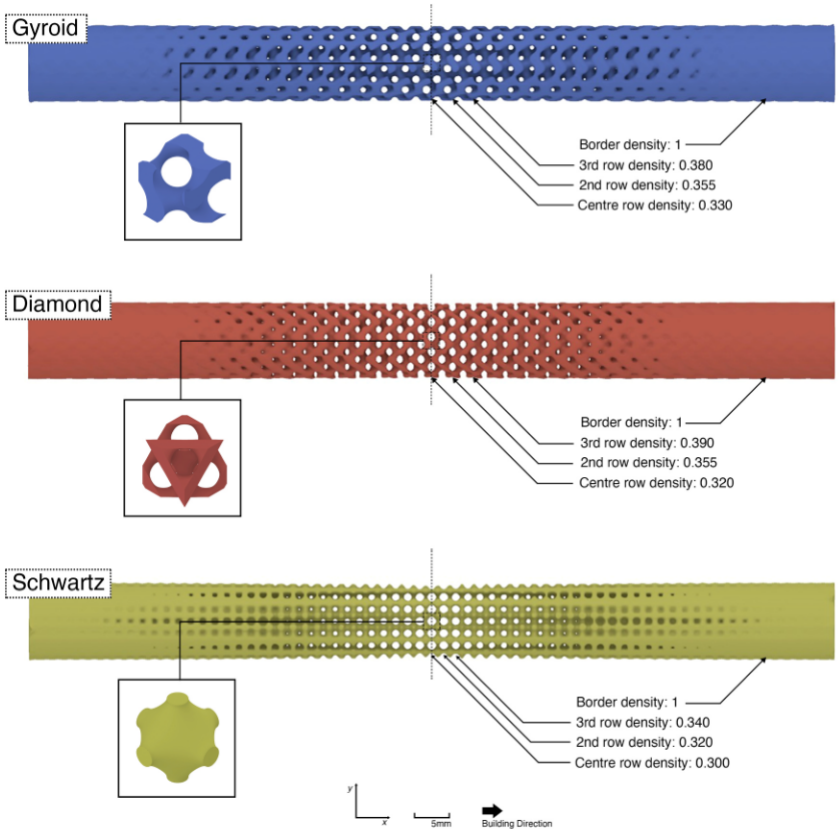

Note. Lattice specimens CAD with solid ends for tension-tension fatigue test by Soro et al. (2021).

The fatigue cycle frequency used for the fatigue tests in literature was between 10 Hz and 50 Hz and was generally done in air with ambient temperature. Studies typically perform quasi-static loading tests to characterise the lattice specimen's ultimate compressive strength and yield strength before performing fatigue tests. The maximum stress applied for the fatigue test is generally calculated at about 80 % of the yield strength or compressive strength and reduced until cycles to failure of above 10^6 are achieved to create the S-N curve of the lattice structure. The stress ratio R used is 0.1, where the maximum stress applied is 10 times the minimum stress. The common failure criterion for the compression-compression fatigue test in literature is either a target maximum reduction of stiffness or a cumulative displacement amount corresponding to a

selected maximum strain. The typical maximum reduction of stiffness selected is 90 % (Kolken et al., 2021; Xiong et al., 2020; Yánez et al., 2020). The cumulative displacement of the lattice structure specimens under fatigue loading was either recorded to calculate the cumulative strain for analysis or noted as the failure criteria. To record the cumulative displacement, the common methods used are using a linear variable displacement transducer (LVDT) and using a digital image correlation (DIC) (Benedetti et al., 2021; Zadpoor, 2019).

Figure 2.20
Stages of Fatigue Damage for Compression-Compression Fatigue

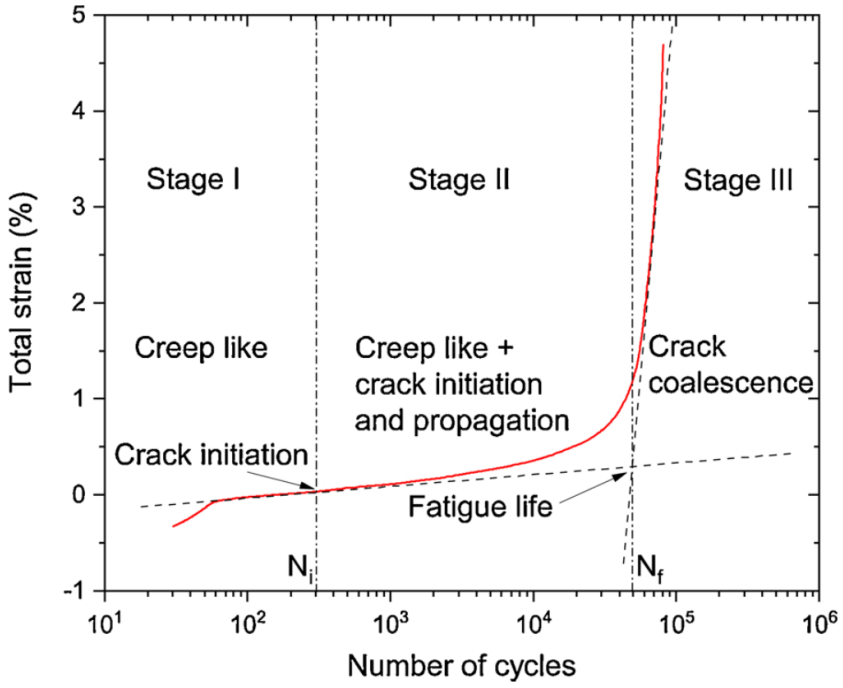

Note. Fatigue damage stages of porous metallic materials during compression-compression fatigue test by Benedetti et al. (2021) and adapted from Lefebvre et al. (2009) and Özbilen et al. (2016).

Benedetti et al. (2021) explained the stages of damage due to the compression-compression fatigue loading on porous metallic materials as shown in Figure 2.20, which was adapted from the studies by Lefebvre et al. (2009) and Özbilen et al. (2016). This would also apply to the Ti-6Al-4V lattice structures made using PBF. The fatigue damage is divided into three stages. The first stage is when the specimen goes through a stabilisation phase under fatigue loading, where the weak location within the structure undergoes localised plastic deformation, which is observed as the initial sharp rise of total strain. Subsequently, the localised stresses are redistributed, which causes the total strain to increase linearly at a much slower rate. In this second phase of stage I, the lattice structure would be ratcheting or slowly accumulating inelastic strain. Stage II starts when the total strain stops increasing linearly, and the lattice structure is said to have crack initiation and

propagation damage. Stage III of fatigue damage is when the lattice structure has a catastrophic failure due to the joining of several cracks that lead to a fracture. The exact number of cycles for the start of stage III is defined as the point of intersection between the linear increase of total strain or the ratcheting line and the linear line fitted after the sudden increase of total strain at the catastrophic failure.

The factors that affected the compressive strength of Ti-6Al-4V lattice structures made using PBF were also found to influence the fatigue strength under compression-compression loading generally. The main factors found to affect fatigue strength were topological design and relative density, from the studies reviewed by Zadpoor (2019) and also found by Amin Yavari et al. (2015). In general, the higher the $\bar{\rho}$ of the lattice structure, the higher its compressive strength and the higher the fatigue strength will be, following the Gibson-Ashby model (Gibson & Ashby, 1997) as found by the review of studies by Benedetti et al. (2021). The topological design factor, which is also known as the unit cell design factor, that was stated to affect the fatigue strength should be related to the dominant deformation modes, which are known to influence the compressive strength of the lattice structures under quasi-static loading, as explained by Deshpande et al. (2001). However, it is not clearly stated that this is the case, as the fatigue crack initiation and propagation may behave differently to the fracture behaviour of the lattice structure under quasi-static compression loading.

TPMS-based unit cell design has been gaining more attention for improving the fatigue strength of the Ti-6Al-4V lattice made with PBF due to the theoretically lower stress concentration at the smoother strut and node connections. Yánez et al. (2020) examined the fatigue strength of the gyroid unit cell design, a skeletal-based TPMS made from Ti-6Al-4V using EB-PBF. They found that the strut surface roughness and defects acted as the crack concentrators and crack initiation sites, negating the theoretical benefit of smoother strut and node connections. This would be even more problematic when the lattice parameters of the skeletal-based TPMS unit cell are at a smaller scale, like those required in osteoconductive lattices. The smooth features at smaller scales will be challenging to replicate and print by the EB-PBF machine and might result in poorer print quality.

Applying heat treatment on the lattice specimen post-print is another method investigated to improve the fatigue strength of the Ti-6Al-4V lattice made with PBF. Heat treatment is more common in studies using L-PBF than EB-PBF due to the inherent residual stresses that exist in L-PBF printed specimens due to the lack of preheating of the powder bed during the print process, like in the EB-PBF. Yuan et al. (2018) examined the effect of heat treatment of annealing by heating the Ti-6Al-4V lattice specimen between 750 °C and 950 °C for one and a half hours in a vacuum. The

lattice specimens were made with EB-PBF using a simple cubic unit cell design. They found that the heat treatment improved the fatigue strength compared to the AB specimens, which was attributed to the improved ductility through the microstructure change after heat treatment. Although this may be an excellent method to improve the fatigue strength of Ti-6Al-4V lattice structures made with EB-PBF, it is preferable to have an AB lattice structure that has a sufficient fatigue strength without post-print heat treatment as this will add cost to production and negate one of the main advantages of EB-PBF over L-PBF.

Similar to quasi-static mechanical behaviour studies for the Ti-6Al-4V lattice structure made with PBF, applying grading on the lattice structure was also explored for improving fatigue strength. Grading can be applied by varying the unit cell size, strut diameter, and pore diameter of the unit cell, which also essentially changes or grades the relative density of the lattice structure. The lattice grading direction can be parallel or perpendicular to the loading direction. Grading the lattice parallel to the loading direction will result in the weakest layer experiencing damage first when loaded and may not improve the overall mechanical behaviour. This grading direction is also used to examine a uniform lattice with graded regions that end with fully solid regions for gripping in fatigue test with a tension loading component (Lietaert et al., 2018; Soro et al., 2021). On the other hand, grading perpendicular to the loading direction will have a different effect where the strongest layer will first experience damage from the fatigue loads, followed by the middle strength layer and lastly, the weakest layer, as found by Zhao et al. (2018). They examined the functional grading effect on the fatigue strength of rhombic dodecahedron Ti-6Al-4V lattice structure made with EB-PBF, where the graded structure consists of three layers of varied unit cell size and strut diameter and from their testing of additional uniform lattice specimen with the cell size and strut diameter each of the graded layer, identified which layer was the strongest to the weakest. Their compression-compression fatigue test found that the fatigue strength of the graded lattice was lower than the uniform lattice with the parameters of the strongest layer but higher than the other two layers. Zhao et al. (2018) concluded that grading the lattice might result in a high fatigue strength and energy absorption compared to a uniform lattice. However, this may not increase the overall fatigue strength of the lattice compared to a uniform lattice with the parameters of the strongest layer in the graded lattice.

2.3.3 Unit Cell Orientation and Batch Variation Effect

Based on the examination of the literature in Section 2.3.1 and Section 2.3.2, the main factors that affect the mechanical properties of Ti-6Al-4V lattice structure can be divided into three general

categories of unit cell design (also known as topological design), relative density (or porosity) and material (which includes microstructures, build direction, print quality and defects, and post-print processing). Porous lattice structures for biomedical bone implants have specific requirements on the lattice parameters for the Ti-6Al-4V lattice structure to be osteoconductive, and this limits the unit cell design and relative density, which leaves the factors of unit cell orientation and material for searching for the lattice structure parameters with the right mechanical behaviour.

Unit cell orientation effect. The unit cell design or topological design effect on the mechanical behaviour of the Ti-6Al-4V lattice structure was related to the dominant deformation mode of the lattice structure, where the stretching-dominated formation lattice structure is significantly stronger than the bending-dominated deformation structure. Most studies have explored different unit cell designs, including TPMS-based ones, and have resulted in either one of these deformation modes. Looking further into this, the type of dominant deformation is related to how load-supporting struts are angled relative to the load. Unit cell designs with struts at sharper angles or parallel to the loading direction generally show stretching-dominated deformation under mechanical loading. The load-supporting struts experience compressive stress internally and will eventually buckle. Struts with higher relative angles to the loading direction generally behave with a bending-dominated deformation under compressive loading. However, looking at the relative angle factor to predict the type of deformation under loading may not always be true, especially when having small struts like those required in osteoconductive lattice structures.

Cuadrado et al. (2017) examined the load orientation effect on the quasi-static compression behaviour of Ti-6Al-4V lattice structures with the unit cell designs of BCC, simple cubic and simple cubic fabricated at 45°, made using EB-PBF (Figure 2.21). The porosity of the lattice specimens was varied at 70 %, 80 % and 90 %, and the struct diameter was about 0.65 mm. The loading orientation factor in this study is similar to the unit cell orientation factor, as the unit cell orientation is defined relative to the loading direction applied to the lattice structure specimen. Cuadrado et al. (2017) found that the simple cubic lattice structure without rotation and the load-supporting struts being parallel to the loading direction had the best quasi-static mechanical properties and was attributed to the buckling mechanism during deformation under load, which is also considered as a stretching dominated deformation. The other unit cell designs experienced bending-dominated deformation under loading and were weaker in compressive strength and elastic modulus. Thus, the unit cell orientation that results in either the deformation mode of stretching or bending will affect the resulting lattice structure's mechanical behaviour, even for the same unit cell design. Although the study discussed lattice structures for biomedical bone implants, the selection of their

unit cell and lattice parameters did not consider the osteoconduction factors, and the pore size is too large, with estimated sizes of above one millimetre.

Figure 2.21
Unit Cell Designs and Lattice Specimens for Load Orientation Effect Study

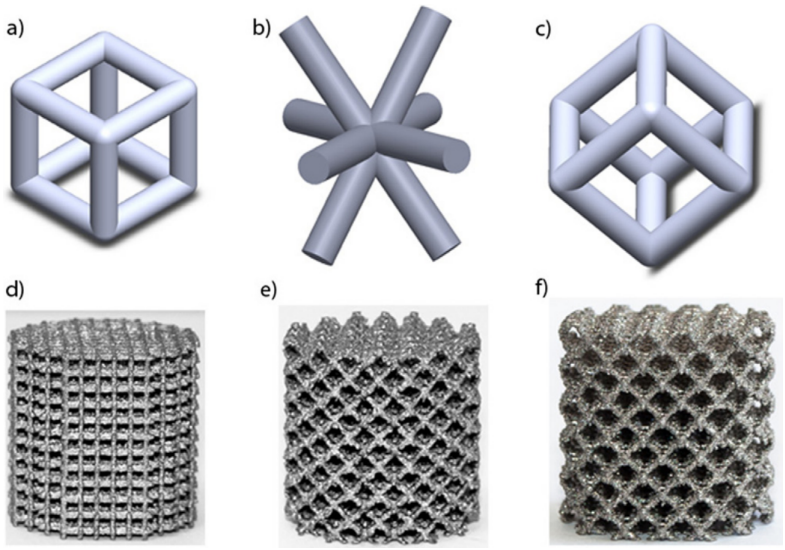

Note. Unit cell designs of (a) simple cubic, (b) BCC and (c) simple cubic fabricated at 45°, and printed lattice specimens used in the study of load orientation effect by Cuadrado et al. (2017).

Weißmann et al. (2016) also studied the unit cell orientation effect on the quasi-static compressive strength using an uncommon twisted unit cell design with various rotation combinations at the x-axis and y-axis and rotation angles of 45° and 90° (Figure 2.22). The unit cell sizes used were not cubic and had all three lengths of their sides varied. The strut diameters of the lattice specimen were larger at 0.9 mm and 1.1 mm. The lattice specimens were printed with Ti-6Al-4V using L-PBF and tested AB. They found that the twisted unit cell's unit cell orientation affected the lattice specimens' mechanical properties under quasi-static compression loading, which they attributed to the angles of the struts relative to the loading direction and build direction of the strut itself. T1-I and T2-I unit cell orientations of 0° rotation had the highest compressive strength and elastic modulus compared to the other unit cell orientations within their orientation type group. Their struts are of the smallest angles relative to the loading direction. Therefore, it can be said that within a bending-dominated deformation structure of the same unit cell design, the unit cell orientation will affect the lattice's overall mechanical strength depending on the strut's relative angle with the loading direction.

Based on the reviewed literature, the factors that contribute to the unit cell orientation effect on the quasi-static mechanical behaviour of Ti-6Al-4V lattice structures made with PBF can be

categorised into three, which are load-supporting strut angle, unit cell design, and build direction. All the directions of these factors are relative to the loading direction applied to the lattice structure. More studies have been done on the quasi-static mechanical behaviour of Ti-6Al-4V lattice structures made with PBF than its fatigue behaviour. Therefore, the unit cell orientation effect of the Ti-6Al-4V lattice structure made with PBF has yet to be considered for its effect on fatigue strength in the literature. The unit cell designs are the closest factor to unit cell orientation studied for fatigue behaviour. The unit orientation effect should be investigated for its effect on the fatigue strength of the Ti-6Al-4V lattice structure, especially with osteoconductive lattice parameters made with EB-PBF.

Figure 2.22
Unit Cell Orientation Effect Study of Twisted Unit Cell Design

Orientation type	T 2 - I	T 2 - II	T 2 - III	T 2 - IV	T 2 - V	T 1 - I	T 1 - IV	T 1 - V
Orientation	0°	45°– y-axis	45°– y-axis 45°- x-axis	90°-y-axis	90°- y-axis 45°- x-axis	0°	90°– y-axis	90°- y-axis 45°- x-axis
Unit cell	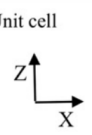							
Scaffold		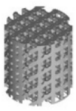						

Note. Unit cell orientation of twisted unit cell designs of T1 and T2 for lattice specimen in the study by Weißmann et al. (2016).

The unit cell orientation is an essential factor affecting the quasi-static mechanical behaviour of the Ti-6Al-4V lattice structure made with PBF. Even with the existing understanding of deformation-dominated architecture effects adapted from the understanding of foam topology by Deshpande et al. (2001) for Ti-6Al-4V lattice structures made with PBF, further examination is still needed for Ti-6Al-4V lattice structure made with EB-PBF, especially for lattice parameters with small features that are osteoconductive. The unit cell orientation of a lattice structure with a simple unit cell design, like the simple cubic, which has features that are suitable for meeting the osteoconductive lattice parameters and still having good powder removal and EB-PBF printability properties, should be examined for its mechanical behaviour with the unit cell orientation factor. It is unclear if the simple cubic Ti-6Al-4V lattice structure made using EB-PBF with osteoconductive lattice parameters will behave following the dominant deformation types for similar unit cell orientations as observed in the study by Cuadrado et al. (2017). It is also unknown if the simple

cubic unit cell is rotated twice by 45° on the x-axis and y-axis each, similar to the rotations in Weißmann et al. (2016), or if the simple cubic is orientated where the one of the vertex is directly pointing upwards, will result in a lattice structure that is stronger than the single 45° rotation on the x-axis, due to three struts being load-supporting for the former, compared to only two in the latter. It is also unknown how these simple cubic orientations may affect its fatigue strength.

Batch variation effect. The current literature has not examined the batch variation effect on the mechanical behaviour of Ti-6Al-4V lattice structures made with PBF. The batch variation effect refers to the variation that is inherent when printing the Ti-6Al-4V lattice structure in an industrial production setting, which may affect the mechanical behaviour. The effect of Ti-6Al-4V powder reuse, as discussed in Section 2.2.1, is the major factor contributing to batch variation. The current literature has examined the effects of T-6Al-4V powder reuse. It mainly focused on its effect on the mechanical properties and microstructures in fully solid printed parts, not on porous lattice structures (Petrovic & Niñerola, 2015; Quintana et al., 2018; Schur et al., 2020). Based on the reviewed literature, the factors potentially contributing to the batch variation effect on lattice structure from the Ti-6Al-4V powder reuse are the morphological, microstructure and chemical composition change. These changes depend on the number of powder reuse times. The higher the reuse times, the greater the changes in the powder characteristic. These changes in powder characteristics affected the mechanical behaviour of Ti-6Al-4V solid parts printed with PBF, as discussed in Section 2.2.1. However, it is unknown how the same changes in power characteristics will affect the mechanical behaviour of Ti-6Al-4V lattice structures, especially with osteoconductive lattice parameters made with EB-PBF.

2.4 Literature Gaps and Research Questions

The review of the relevant literature on the effect of unit cell orientation and batch variation on the mechanical behaviour of Ti-6Al-4V lattice structures with osteoconductive lattice parameters made by EB-PBF can be summarised below.

- Many studies have been done for studying the quasi-static mechanical behaviour of Ti-6Al-4V lattice structures made by PBF, especially for the application of biomedical bone implants. However, these studies have neglected to consider the factors of lattice parameters for osteoconductivity, cell design with good unmelted powder removal and printability with EB-PBF when designing their lattice specimen.

- The dominant deformation mode effect on the quasi-static mechanical behaviour for differ-

ent unit cell designs of Ti-6Al-4V lattice made with PBF has been studied and understood to follow the Gibson-Ashby model. However, the dominant deformation mode effect has not been fully understood with the unit cell orientation relative to the loading direction factor, especially for structures with osteoconductive lattice parameters of small strut sizes made with EB-PBF. This is also the same for the fatigue behaviour.

- Ti-6Al-4V powder reuse is unavoidable in an industrial production setting, and studies have found that powder reuse affects the mechanical properties of solid Ti-6Al-4V parts printed with PBF. However, the effects of powder reuse on the mechanical behaviour of Ti-6Al-4V lattice structures printed with EB-PBF are still unclear, especially for osteoconductive lattice structures. The powder reuse effect can be combined into the batch variation effect, where the overall variation between batches of builds in an industrial production setting is considered for its effect on the mechanical properties of both quasi-static and fatigue for Ti-6Al-4V lattice structures made by EB-PBF, which is also lacking in the current literature.

The following research questions are raised based on the literature gaps identified above.

1. How does the orientation of the simple cubic unit cell relative to the loading direction affect the overall mechanical strength of its Ti-6Al-4V lattice structure with osteoconductive lattice parameters made by EB-PBF under quasi-static compression and cyclic compression-compression loading?

2. What is the effect of the batch variation inherent in a production operation utilising the EB-PBF process in an industry setting on the mechanical strength of the simple cubic Ti-6Al-4V lattice structure with osteoconductive lattice parameters under quasi-static compression and cyclic compression-compression loading?

Chapter 3

Experimental Design and Procedures

This third chapter will present and detail the experimental designs and procedure for testing the mechanical strength of the simple cubic Ti-6Al-4V lattice. The details of the simple cubic lattice specimen design are first outlined with the details of the EB-PBF machine and the batch processing. Next, examining the lattice structure using scanning electron microscopy is specified. Then, the experimental mechanical testing for the quasi-static compressive test and compression-compression fatigue test are detailed. Lastly, the numerical analysis of the quasi-static compressive test is described.

3.1 Specimen Design and Printing

3.1.1 Simple Cubic Ti-6Al-4V Lattice

The simple cubic unit cell is the unit cell design selected for this study's lattice specimens. An example of the simple cubic unit cell design is shown in Figure 2.1. The simple cubic unit cell design was selected due to its simple structure with uniform strut length and perpendicular struts, which gives it good powder removal properties and ease of adjusting the unit cell parameters to meet the pore diameter and porosity requirements for osteoconductive lattice structures.

The BS ISO 13314:2011 standard was also adopted as a guide for the overall dimensions specifications of the lattice specimens used in this study (British Standards Institution, 2012), which is the common standard referred to in literature for PBF porous lattice structures studies. Adapting the standard specification, the overall lattice specimen diameter, D_o for cylindrical specimens must be at least 10 times the average pore diameter, d_a and should not be smaller than 10 mm, while the specimen height, H_o should be one to two times the D_o, as shown in Figure 3.1. Therefore, the cylindrical simple cubic lattice specimen printed for this study has dimensions of 20 mm in height

and 10 mm in diameter. An example of the CAD for the simple cubic lattice specimen is shown in Figure 3.2. The overall dimension of the lattice structure is also referred to as the volume of interest (VOI), as the generation of the lattice specimen CAD involves taking a VOI, in this case, a cylindrical VOI, within a large simple cubic lattice and using the combine command with the common volume. The lattice specimen CAD was created using the Materialise Magics software in the standard triangle language (STL) form.

Figure 3.1
BS ISO 13314:2011 Porous Cellular Specimen Specification

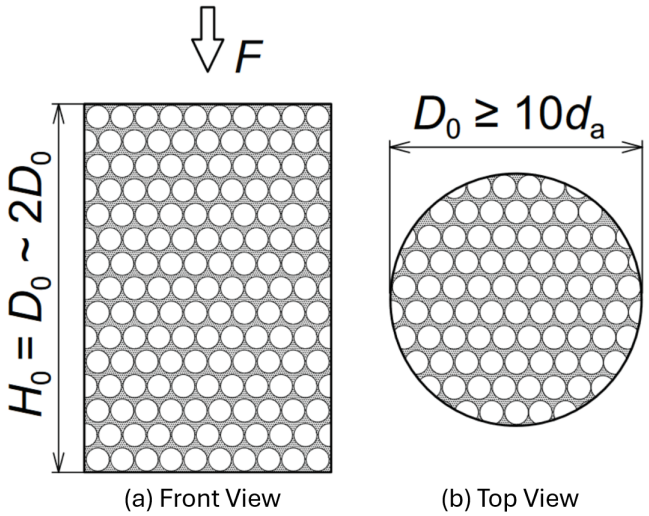

Note. Cylindrical cellular specimen dimension specification according to BS ISO 13314:2011 (British Standards Institution, 2012). The diameter of the cellular specimen, D_o, must be at least 10 times the average pore diameter, d_a and should be at least 10 mm. The cellular specimen height, H_o, must be one to two times the D_o. The compressive loading direction is along the specimen height.

All simple cubic lattice specimens have the same cell size, l_c of 1.1 mm, strut diameter, d_s of 0.5 mm and pore diameter, d_p of 0.6 mm, as shown in Table 3.1 and in Figure 3.3(f). The relative density of the lattice specimens is in the range of 35 % to 36 %. The build direction of the lattice specimens is parallel to the loading direction and along the length of the lattice structure specimen. The intended application of the simple cubic lattice specimens in this study is for biomedical bone implants, especially for hip stems. As the major loading mode for the hip stem implant in the femur is compressive loading, thus the specimen is designed and tested for mechanical compressive loading mode. Therefore, the specimens were printed with solid caps at the ends, as shown in Figure 3.4, to ensure the compressive loading applied is distributed on the simple cubic lattice structure. The gauge length of the specimens is the height of the porous lattice structure, H_o, which is also the height of the VOI of 20 mm. The diameter of the specimen, D_o, is

10 mm and is used to calculate the specimens' cross-sectional area, A_o, which is 78.54 mm^2.

Figure 3.2
Simple Cubic Lattice Specimen CAD Example

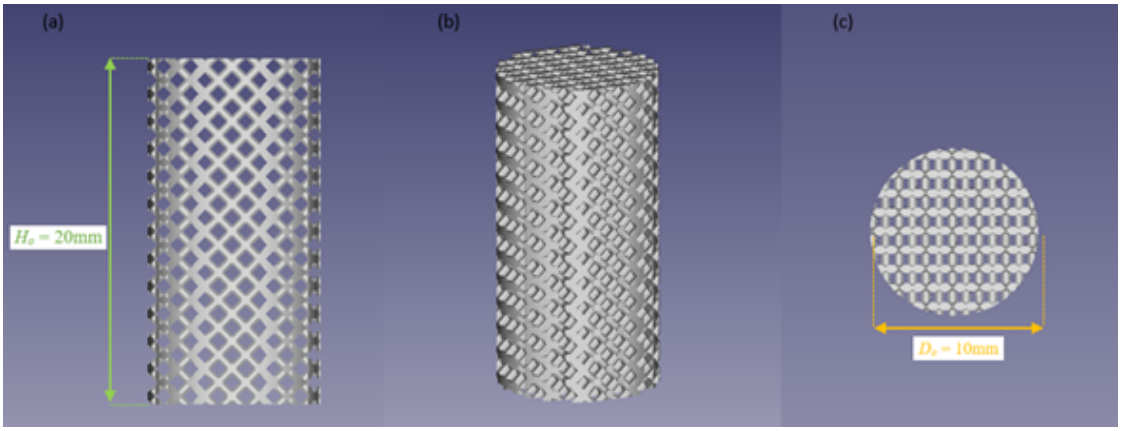

Note. Cylindrical simple cubic lattice specimen with a height, H_o of 20 mm and diameter, D_o of 10 mm. (a) Front view, (b) 3D view and (c) top view of the lattice specimen.

Table 3.1
Lattice Parameters of Simple Cubic Ti-6Al-4V Lattice Specimens

Orientation	Cell Size, l_c (mm)	Strut Diameter, d_s (mm)	Pore Diameter, d_p (mm)	Relative Density, $\bar{\rho}$ (%)	Dimension D_o; H_o (mm)	Cross-section Area, A_o (mm^2)
[001]	1.1	0.5	0.6	35.39	10; 20	78.54
[011]	1.1	0.5	0.6	35.64	10; 20	78.54
[111]	1.1	0.5	0.6	35.48	10; 20	78.54
[$\sqrt{1/2}$ $\sqrt{1/2}$1]	1.1	0.5	0.6	35.41	10; 20	78.54

Note. Lattice structure parameters for the simple cubic Ti-6Al-4V specimens printed using Arcam EBM Q10plus.

To study the effects of the unit cell orientation relative to the loading direction, the simple cubic unit cell was rotated according to the vector orientations in Figure 3.5 and obtained four orientations of [001], [011], [111] and [$\sqrt{1/2}$ $\sqrt{1/2}$1]. The simple cubic unit cell with [001], [011], and [$\sqrt{1/2}$ $\sqrt{1/2}$] orientation are shown in Figure 3.3(a), Figure 3.3(b) and Figure 3.3(c). The simple cubic unit cell with [111] orientation looks almost similar to Figure 3.3(c) with three struts equally facing upwards and another three downwards.

The vector orientations in Figure 3.5 are used in this thesis to express the simple cubic unit cell orientation for simplicity. The vector orientation is based on a cube with one vertex at the origin point of (0,0,0), and its whole volume is in the positive region of all three axes. The origin point (0,0,0) is the rotation centre for all orientations. The unit cell's [001] orientation is without

rotation and is the typical orientation used when examining the simple cubic lattice structure in literature. The loading axis or direction passes through the top and bottom faces at normal and is parallel to the z-axis, the [001] vector. The other orientation vectors are expressed relative to the [001] orientation.

Figure 3.3
Simple Cubic Unit Cell Design

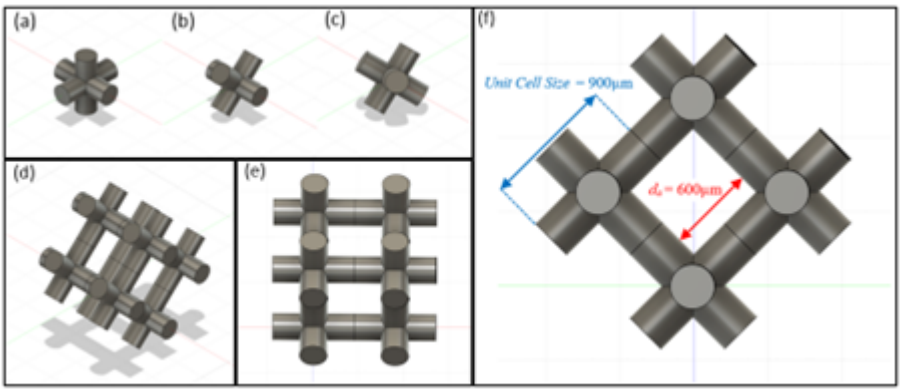

Note. Simple cubic unit cell with orientations of (a) [001], (b) [011] and (c) [$\sqrt{1/2}$ $\sqrt{1/2}$1]. (d) 3D view, (e) side view and (f) front view of a lattice example with $2 \times 2 \times 2$ simple cubic cells. Simple cubic with [111] orientation is almost similar to (c).

Figure 3.4
Simple Cubic Ti-6Al-4V Lattice Specimens

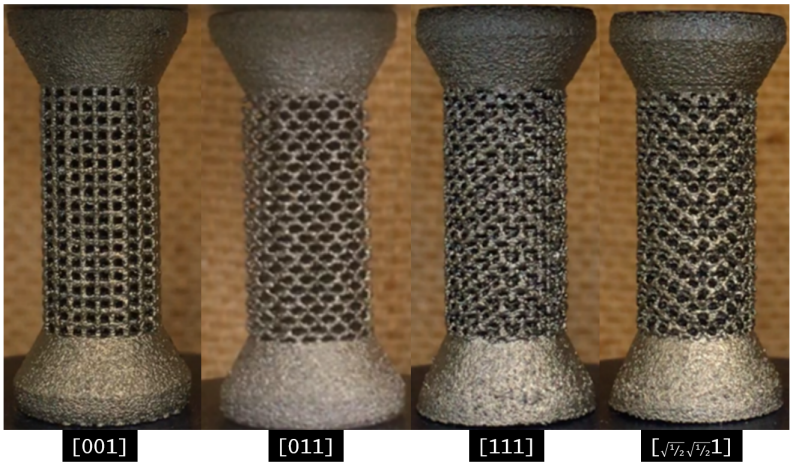

Note. Simple cubic Ti-6Al-4V lattice specimens with solid end caps printed using EB-PBF for this study. Specimens shown with different unit cell orientations of [001], [011], [111] and [$\sqrt{1/2}$ $\sqrt{1/2}$1].

The second unit cell orientation of [011] was created by rotating the cube unit cell around the x-axis (roll) by $-45°$ and with the centre of rotation at (0,0,0). The rotated cube will have top and bottom edges aligned at the x-axis and y-axis and perpendicular to the z-axis. The resulting

loading axis passes through both edges perpendicularly and is parallel to the rotated cube, which has the [011] vector. The simple cubic unit cell's [011] orientation makes two load-supporting struts at each node with angles of 45° relative to the loading direction.

Figure 3.5
Illustration of Unit Cell Orientation Vectors

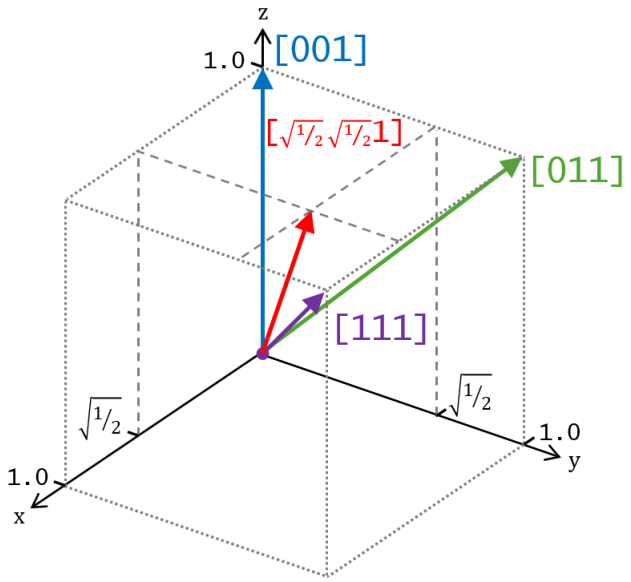

Note. Vectors of unit cell orientations of [001], [011], [111] and [$\sqrt{1/2}$ $\sqrt{1/2}$1] are illustrated relative to a unit cell with no rotation. The loading direction is parallel and opposite to the unit cell orientation vectors. The unit cell is orientated by rotating the unit cell until the vectors align with the z-axis or loading direction.

The third unit cell orientation of [$\sqrt{1/2}$ $\sqrt{1/2}$1] was created by rotating the cube unit cell −45° around the x-axis (roll) and 45° around the y-axis (pitch). The rotated cube will have a vertex at the top and bottom that offset each other when looking along the z-axis. The resulting loading axis with the bottom vertex as the origin point, relative to the z-axis, is the vector of [$\sqrt{1/2}$ $\sqrt{1/2}$1], where the loading axis passes through one face of the rotated cube and one vertex at the bottom. This also applies to the other vertex on top of the rotated cube, which has a parallel loading axis that goes through the face of the rotated cube facing down. The [$\sqrt{1/2}$ $\sqrt{1/2}$1] orientation is a simple 45° rotation at the x-axis and y-axis that makes one node have three load supporting struts, with two struts have the same angle and the third having another angle relative to the loading direction.

For the fourth and last unit cell orientation of [111], the cube unit cell with the centre of rotation at (0,0,0) is first rotated −45° around the x-axis (roll) and the angle of approximately 34.26° or $\theta = \tan^{-1}(\sqrt{2})$ around the y-axis (pitch). The rotated cube will have a vertex at the top and bottom that is aligned along the z-axis. Three faces of the rotated cube will be visible as equal rhombuses when viewed from the top or bottom parallel to the z-axis. The resulting loading axis

parallel to the z-axis has the vector of [111], which passes through the bottom vertex to the top vertex of the rotated cube. The [111] orientation is different from the [$\sqrt{1/2}$ $\sqrt{1/2}$1], where the three load supporting strut for each node have equal angles relative to the loading direction.

3.1.2 EB-PBF Machine and Ti-6Al-4V Powder

The simple cubic lattice specimens in this study were made using the EB-PBF machine of Arcam EBM Q10plus (Figure 3.6). The powder feed-stocks used were Ti-6Al-4V grade 5 powder supplied by AP&C, GE Additive and certified to the standard ASTM F2924-14 (ASTM International, 2014b). The build layer thickness was 50 μm. The build chamber was kept in a vacuum chamber with a continuous small amount of helium gas feed during the print, which provided an inert atmosphere during the melting and resolidification process. This makes the EB-PBF advantageous for printing reactive alloys like Ti-6Al-4V for biomedical bone implant applications. No post-print heat treatment was done on the specimens.

Figure 3.6
Electron Beam Powder Bed Fusion Machine

Note. EB-PBF machine of Arcam EBM Q10plus machine by General Electric (2024).

The net theme melt program was used for the simple cubic lattice, and the standard melt theme was used for the solid ends of the lattice specimens. After printing, the non-melted powder was removed from the internal spaces of the printed specimen using the powder recovery station (PRS), and a visual inspection was performed to confirm that no unmelted powder had remained. All specimens were tested as-built. The lattice specimens were all printed with the length, H_o,

orientated along the build direction or normal to the build plate. This keeps the build direction factor constant for all specimens with different unit cell orientations.

3.1.3 EB-PBF Batch Processing

The specimens were printed in batches subjected to the collaborating company's production schedule to study the batch variation effect on the simple cubic Ti-6Al-4V lattice under industrial production settings. Therefore, the powder used to print the specimens was a different mix of virgin and reused powders for each batch. The specimens were also printed with other solid parts as scheduled for production.

The lattice specimens used in this study were from six build batches, and each batch has a varying number of orientation types available, as shown in Table 3.2. There are four types of orientations of [001], [011], [111] and [$\sqrt{1/2}$ $\sqrt{1/2}$1]. The printing and availability of these specimens depended greatly on the collaborating company, where batch samples can only be printed when there is a scheduled build with the availability of space within the build volume. This is because the printing of specimens is done together within the production process of the collaborating company, which is the only financially viable way for the specimen to be made without costing the collaborating extra production time for machine setup and turnover. Therefore, the number of specimens in each batch and the unit cell orientations also differ.

The net theme is a melting program used in the EB-PBF machine of Arcam EBM Q10plus. It is a different melting program when compared to the standard melting process or melt theme for solid parts. The net theme is used especially for small and fine features on parts like porous lattices with sub-millimetre features. The EB-PBF machine manufacturer does not disclose the exact details of the net theme. The only detail available about the net theme is that the melting process does not follow a melt path or electron beam (e-beam) scanning track like the regular melt theme for a solid part and instead has a pseudo track that is smaller than the actual part feature to account for the resolidified melt pool at the contours that will cause the printed part to be slightly larger.

Two net themes were used for printing the specimens for this study, as shown in Table 3.2. Net theme A is the original net theme used for production when the specimens of batches 0932, 0937, 0950 and 1013 were printed, whereas specimens from batches 1123 and 1170 were printed after the net theme was updated to B. The differences between these net themes cannot be disclosed, and net theme B is supposed to be slightly better than the original net theme A. Therefore, in this study, the batch variation effect on the quasi-static mechanical strength is examined through two

Table 3.2
Simple Cubic Ti-6Al-4V Lattice Printed Specimens

Batch	Net Theme	Orientation	Number of Tested Specimens	
			Quasi-static Compressive	Compressive Fatigue
0932	A	[011]	1	6
0937	A	[011]	6	2
0950	A	[011]	3	8
1013	A	[001]	3	-
		$[\sqrt{1/2}\ \sqrt{1/2}1]$	4	15
1123	B	[001]	4	-
		[111]	5	-
		$[\sqrt{1/2}\ \sqrt{1/2}1]$	3	-
1170	B	[001]	3	-
		[011]	3	-
		[111]	3	-
		$[\sqrt{1/2}\ \sqrt{1/2}1]$	3	-

Note. Batch, orientation and net theme details for simple cubic Ti-6Al-4V lattice specimens made with EB-PBF. The number of specimens tested for quasi-static compressive and compressive fatigue experiments is detailed.

groups of batch specimens of net themes A and B, where the batch variation effect within the same net theme is examined. On the other hand, the unit cell orientation effect is compared within and between the net theme groups.

3.2 Scanning Electron Microscope Analysis

The lattice specimens were examined using a scanning electron microscope (SEM) to study their strut irregularities of notches, melt imperfections, and partially melted powder and estimate their effective strut diameter or thickness. The fatigue fracture of the compressive fatigue specimens was also examined to compare their fracture characteristics at different cycles to failure range. These were used to help understand the mechanical strength response from the quasi-static compressive and compressive fatigue tests. The SEM machine used in this study is the Hitachi SU-70 field emission SEM. An acceleration voltage of 5 kV to 15 kV was used to observe the lattice specimens. The estimation of the effective strut diameter, $d_{s\text{-}e}$, was performed using the ImageJ software on the SEM images of the lattice specimens.

3.3 Mechanical Testing

3.3.1 Quasi-static Compressive Test

A quasi-static compressive experiment was carried out to investigate the effect of unit cell orientation and batch variation on the compressive strength of the simple cubic Ti-6Al-4V lattice. A compression load test was selected instead of a tensile because this study's intended application of the simple cubic lattice is for biomedical bone implants, especially for the hip stem. Thus, a compression load test would be better in mimicking the application. Although the tensile loading test is the common material testing mode for both quasi-static and fatigue, for porous lattice structures, compressive loading will also generate tensile and compressive stresses within the struts of the lattices. Compressive loading is also more common in studies examining the mechanical strength of porous lattice structures made with PBF.

Figure 3.7
Quasi-static Compressive Test Setup

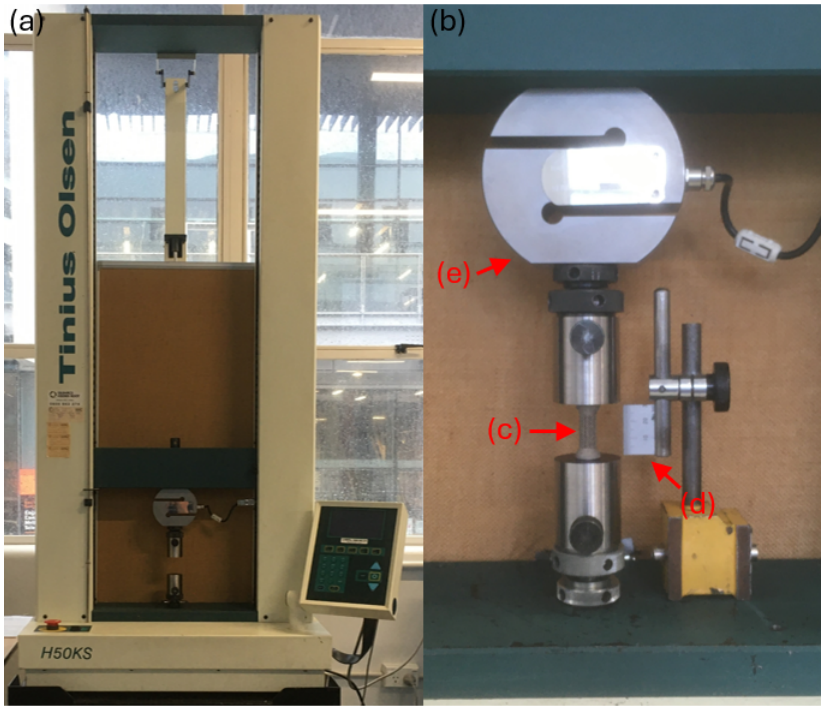

Note. Test setup for quasi-static compressive test using the (a) Tinius Olsen H50KS universal testing machine with a (e) load cell of 50 kN. A (d) ruler is used as a reference gauge in the video recording of the test.

The mechanical testing machine used was the Tinius Olsen H50KS universal testing machine with a load cell of 50 kN, as shown in Figure 3.7(a). The crosshead travel speed for the quasi-static compressive test was based on the adapted BS ISO 13314:2011 standard, which specifies that the constant crosshead speed must result in an initial compressive strain rate of between 10^{-3}

s^{-1} to 10^{-2} s^{-1} (British Standards Institution, 2012). The crosshead travel speed was set to 1.2 mm/min based on the calculation using the lattice specimen gauge length H_o of 20 mm. The test was conducted at ambient temperature. The quasi-static compressive test was stopped when the recorded force dropped significantly or when the lattice structure specimen had a catastrophic fracture collapse. The testing machine recorded the force and displacement results over time.

Figure 3.8
Example of Force vs Displacement Result Graph

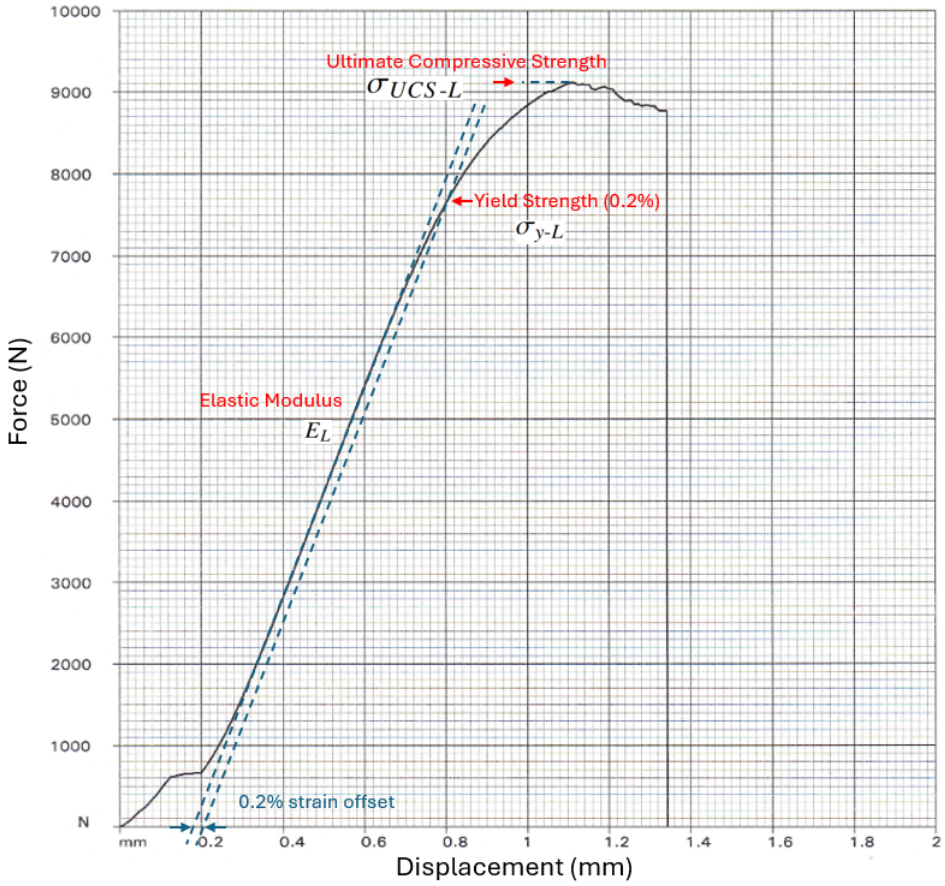

Note. Example of the printed force versus displacement result recorded by the Tinius Olsen H50KS universal testing machine for the quasi-static compressive test. The ultimate compressive strength $\sigma_{UCS\text{-}L}$, yield strength $\sigma_{y\text{-}L}$, and elastic modulus E_L were measured and calculated from the graph.

An example of the force versus displacement results printed from the Tinius Olsen H50KS universal testing machine is shown in Figure 3.8. The lattice specimen's strain was measured by referring to the crosshead travel based on the recorded displacement. The compressive stress was calculated using Equation 3.1, where A_o is the cross-sectional area of the lattice specimen with a diameter of 10 mm and the force is the compressive force recorded from the test. The ultimate compressive strength of the lattice specimen, $\sigma_{UCS\text{-}L}$, is the highest force recorded before a drop. The elastic modulus of the lattice specimen, E_L, is estimated from the linear region of the force

vs displacement graph. From the estimated E_L line, a displacement offset corresponding to 0.2 % strain was applied to obtain the yield strength, $\sigma_{y\text{-}L}$ of the lattice.

$$\sigma = \frac{F}{A_o} \tag{3.1}$$

3.3.2 Compression-Compression Fatigue Test

A constant amplitude fatigue loading experiment was carried out to examine the effect of unit cell orientation and batch variation on the fatigue strength of the simple cubic Ti-6Al-4V lattice. The fatigue test was performed using the MTS Landmark Servo-hydraulic Test System with a load cell of 25 kN, as shown in Figure 3.9(a). The fatigue test will be in compression-compression mode with a stress ratio, R of 0.1, and the stress cycle will follow a sinusoidal waveform with a frequency of 20 Hz (Figure 3.10). The compression-compression mode was selected because the lattice's intended application in this study is for biomedical bone implants, especially for the hip stem. Therefore, a non-reversible compression-compression fatigue test would be better suited to mimic the application.

The specimen lattice tested for the fatigue test has the same lattice parameters and dimensions as the specimen lattice in the quasi-static compressive test, which means that the specimen lattice for the fatigue test also follows the adapted BS ISO 13314:2011 standard (British Standards Institution, 2012). The maximum stress, σ_{max}, was calculated using the lattice specimen cross-sectional area or VOI cross-sectional area, A_o of 78.54 mm^2 (Equation 3.2). The minimum stress σ_{max} is then calculated using the stress ratio, R of 0.1 (Equation 3.3).

The initial σ_{max} and maximum force, F_{max} were calculated based on about 60 % of the compressive yield strength, and the subsequent σ_{max} was reduced by 20 % each time on both sides to obtain the fatigue strengths across the cycles to failure range. The test was terminated when the stiffness decreased by 10 % from the initial stiffness at the maximum compressive force applied or when the runout cycle count of 10^6 is achieved, similar to the fatigue tests termination criteria by Ahmadi et al. (2018) and Dallago et al. (2018). The fatigue test was carried out in the air with ambient temperature.

$$\sigma_{max} = \frac{F_{max}}{A_o} \tag{3.2}$$

$$R = \frac{\sigma_{min}}{\sigma_{max}} = 0.1 \tag{3.3}$$

Figure 3.9
Compression-Compression Fatigue Test Setup

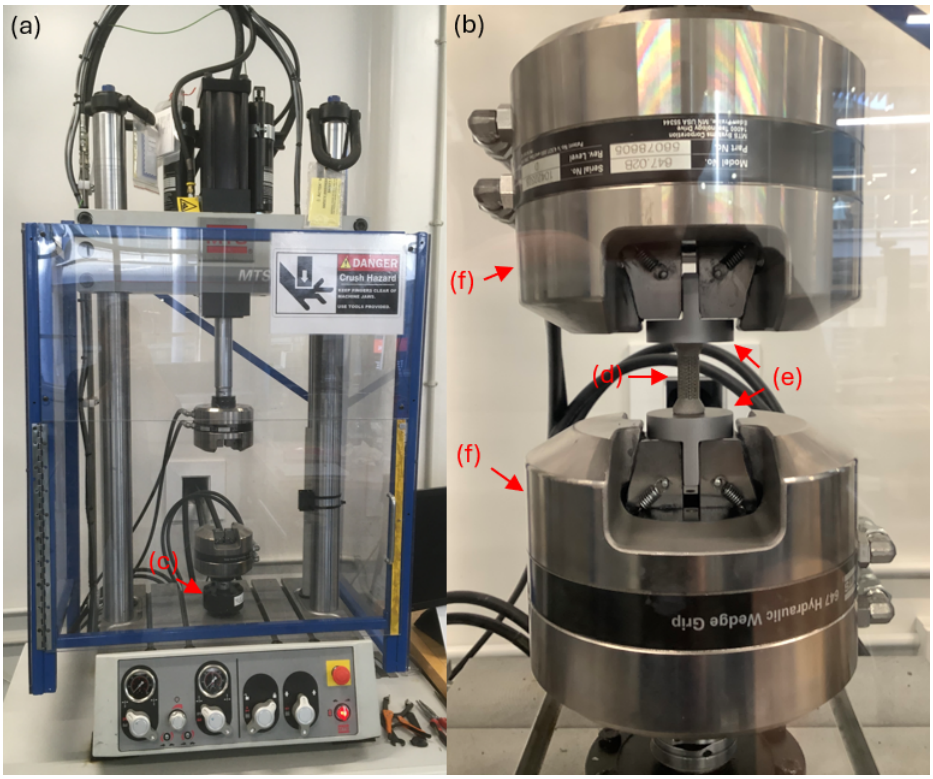

Note. Test setup for compression-compression fatigue of Ti-6Al-4V lattice specimens using the (a) MTS Landmark servo-hydraulic test system with (c) 25 kN load cell. The (d) lattice specimens are tested between two (e) cylindrical plates with vertical posts that are held by the (f) wedge grips.

Figure 3.10
Non-reversible Compression-Compression Stress Cycle

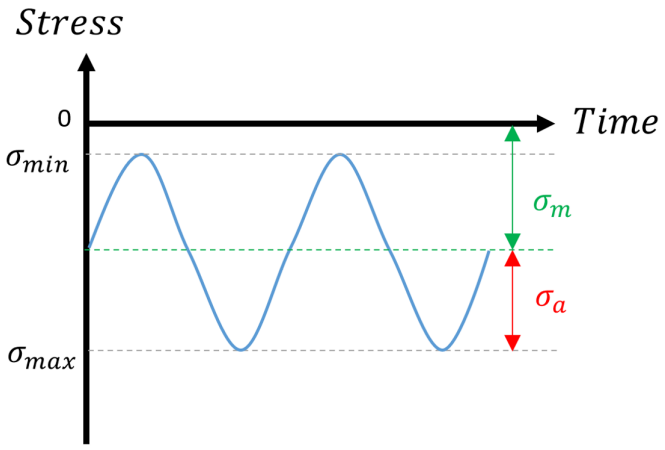

Note. The stress cycle illustrated for the non-reversible constant amplitude compression-compression fatigue loading. The maximum stress, σ_{max}, was first calculated, and the minimum stress, σ_{min}, was calculated using the stress ratio, R. The σ_m and σ_a are the mean stress and stress amplitude.

3.4 Numerical Analysis of Quasi-static Compressive Test

A numerical analysis of the quasi-static compressive test was carried out to understand the unit cell orientation effect on the compressive strength of the simple cubic Ti-6Al-4V lattice without the influence of the strut irregularities. The software ANSYS Mechanical ADPL R1 20.1 was used for the simulation analysis. Lattice specimens CAD with the parameters listed in Table 3.3 were first created in Solidworks before being transferred to ANSYS. The lattice specimen CAD was made by first creating a very large lattice of simple cubic unit cells rotated to the required orientation. Then, a cylinder volume of interest (VOI) with the dimensions of diameter D_o of 10 mm and height H_o of 20 mm was created. After positioning the VOI within the large simple cubic lattice, the lattice specimen CAD was created using the combined command with the common volume. To ensure that the lattice structure at the ends of the lattice specimen CAD behaves like the printed specimens, cylindrical plates were added at the top and bottom of the specimen and combined as a single body. The bottom plate was applied with a fixed boundary condition, and the top plate was applied with an axial displacement boundary condition. A mesh sensitivity analysis was performed, and a mesh size of 0.2 mm was selected. The bi-linear elastic-plastic material properties of solid Ti-6Al-4V alloy were used. The yield strength, $\sigma_{y\text{-}L}$ and elastic modulus, E_L of the lattice specimen CAD were calculated using the strain-stress curves obtained.

Table 3.3
Lattice Specimens Parameters for Quasi-static Compression Simulation

Orientation	Cell Size, l_c (mm)	Strut Diameter, d_s (mm)	Relative Density, $\bar{\rho}$ (%)	Dimension D_o; H_o (mm)	Cross-section Area, A_o (mm^2)
[001]	1.1	0.5	35.39	10; 20	78.54
[011]	1.1	0.5	35.64	10; 20	78.54
[111]	1.1	0.5	35.48	10; 20	78.54
[$\sqrt{1/2}$ $\sqrt{1/2}$1]	1.1	0.5	35.41	10; 20	78.54

Note. Lattice structure parameters for CAD specimen generation used in the quasi-static compression simulation.

Chapter 4

Results and Discussion

In this chapter, the results of the experiments conducted, as stated in the previous chapter, are presented and discussed in two sections to understand how this answers the research questions outlined in the second chapter. The first section presents the data and analysis from the quasi-static compression experiment with the simulated test data, followed by the discussion of findings and comparison with similar simple cubic Ti-6Al-4V lattice quasi-static compressive data from existing studies. The second section presents the experimental data and analysis for the compressive fatigue test. A discussion of the findings with compressive fatigue test data from current literature follows at the end of the chapter.

4.1 Orientation and Batch Variation Effect on Compressive Strength of Simple Cubic Ti-6Al-4V Lattice

4.1.1 Quasi-static Compressive Experiment Data

The quasi-static compressive test data of ultimate compressive strength $\sigma_{UCS\text{-}L}$, yield strength $\sigma_{y\text{-}L}$ and elastic modulus E_L of the lattice specimens obtained from the experiment done are shown in Table 4.1, Table 4.2 and Table 4.3 respectively. There are four unit cell orientations of [001], [011],[111] and [$\sqrt{1/2}$ $\sqrt{1/2}$1], and there are five batches of 0932, 0937, 0950, 1123 and 1170. However, batch 0932 has only one tested specimen, as the specimens were limited and primarily used in the compressive fatigue test. Thus, only one specimen was tested for quasi-static compression for a data point for its mechanical strength. The graphical representation of the quasi-static compressive data is shown in Figure 4.4, Figure 4.5 and Figure 4.6 with the mechanical properties against the unit cell orientation to look at the batch variation factor, whereas Figure 4.1, Figure 4.2 and Figure 4.3 are presented with the same mechanical properties against batch variation variable

to examine the unit cell orientation factor.

Table 4.1
Ultimate Compressive Strength Data for Quasi-static Compressive Test

		Ultimate Compressive Strength, $\sigma_{UCS\text{-}L}$ (MPa)						
Orientation	Batch	1	2	3	4	5	6	Mean±SD
[001]	1013	153	148	152	-	-	-	151 ± 3
[001]	1123	239	222	232	239	-	-	233 ± 8
[001]	1170	236	237	238	-	-	-	237 ± 1
[011]	0932	55	-	-	-	-	-	-
[011]	0937	44	45	45	54	46	47	47 ± 4
[011]	0950	21	37	38	-	-	-	32 ± 10
[011]	1170	111	105	111	-	-	-	109 ± 4
[111]	1123	113	113	120	110	108	-	113 ± 4
[111]	1170	113	112	116	-	-	-	114 ± 2
[$\sqrt{1/2}$ $\sqrt{1/2}$1]	1013	62	59	59	60	-	-	60 ± 2
[$\sqrt{1/2}$ $\sqrt{1/2}$1]	1123	116	118	116	-	-	-	117 ± 1
[$\sqrt{1/2}$ $\sqrt{1/2}$1]	1170	109	113	116	-	-	-	113 ± 3

Note. Ultimate compressive strength data of simple cubic Ti-6Al-4V lattice specimens with different orientations and batches.

Table 4.2
Yield Strength (0.2 %) Data for Quasi-static Compressive Test

		Yield Strength (0.2 %), $\sigma_{y\text{-}L}$ (MPa)						
Orientation	Batch	1	2	3	4	5	6	Mean±SD
[001]	1013	115	108	104	-	-	-	109 ± 6
[001]	1123	187	180	178	188	-	-	183 ± 5
[001]	1170	183	185	183	-	-	-	184 ± 2
[011]	0932	49	-	-	-	-	-	-
[011]	0937	40	41	44	49	40	44	43 ± 4
[011]	0950	20	34	32	-	-	-	29 ± 8
[011]	1170	91	91	94	-	-	-	92 ± 2
[111]	1123	100	101	104	98	92	-	99 ± 4
[111]	1170	102	100	104	-	-	-	102 ± 3
[$\sqrt{1/2}$ $\sqrt{1/2}$1]	1013	54	49	49	52	-	-	51 ± 2
[$\sqrt{1/2}$ $\sqrt{1/2}$1]	1123	102	106	101	-	-	-	103 ± 2
[$\sqrt{1/2}$ $\sqrt{1/2}$1]	1170	98	99	99	-	-	-	99 ± 1

Note. Yield strength (0.2 %) data of simple cubic Ti-6Al-4V lattice specimens with different orientation and batches.

Table 4.3
Elastic Modulus Data for Quasi-static Compressive Test

		Elastic Modulus, E_L (GPa)						
Orientation	Batch	1	2	3	4	5	6	Mean±SD
[001]	1013	4.1	4.6	4.6	-	-	-	4.4 ± 0.3
[001]	1123	5.3	4.2	5.2	5.1	-	-	5.0 ± 0.5
[001]	1170	5.0	5.0	5.2	-	-	-	5.1 ± 0.1
[011]	0932	2.1	-	-	-	-	-	-
[011]	0937	1.3	1.6	1.5	1.8	1.9	1.8	1.7 ± 0.2
[011]	0950	0.7	1.3	1.5	-	-	-	1.1 ± 0.4
[011]	1170	3.0	2.9	3.0	-	-	-	2.9 ± 0.1
[111]	1123	3.1	3.0	2.5	3.3	3.3	-	3.0 ± 0.3
[111]	1170	3.0	3.0	3.1	-	-	-	3.0 ± 0.04
$[\sqrt{1/2}\ \sqrt{1/2}1]$	1013	2.0	2.0	2.1	2.0	-	-	2.1 ± 0.1
$[\sqrt{1/2}\ \sqrt{1/2}1]$	1123	3.3	3.0	3.3	-	-	-	3.2 ± 0.2
$[\sqrt{1/2}\ \sqrt{1/2}1]$	1170	3.1	3.0	3.1	-	-	-	3.1 ± 0.02

Note. Elastic modulus data of simple cubic Ti-6Al-4V lattice specimens with different orientations and batches.

Table 4.4
Experimental Quasi-static Compressive Test Data Comparison

Batch	Orientation Comparison	UCS Factor	Yield Strength Factor	Elastic Modulus Factor
1013	[001]/$[\sqrt{1/2}\ \sqrt{1/2}1]$	2.52	2.14	2.10
1123	[001]/[111]	2.06	1.85	1.67
	[001]/$[\sqrt{1/2}\ \sqrt{1/2}1]$	1.99	1.78	1.56
1170	[001]/[011]	2.17	2.00	1.76
	[001]/[111]	2.08	1.80	1.70
	[001]/$[\sqrt{1/2}\ \sqrt{1/2}1]$	2.10	1.86	1.65

Note. Comparison of experimental quasi-static compressive data relative to [001] orientation for simple cubic Ti-6Al-4V lattice based on the data from Table 4.1, Table 4.2 and Table 4.3.

Orientation effect on compressive strength data. Examining the quasi-static compressive experiment data against unit cell orientation in Figure 4.1, Figure 4.2 and Figure 4.3, the orientation [001] lattice has significantly higher mechanical strength on average when compared to the other three orientations of [011], [111] and [$\sqrt{1/2}$ $\sqrt{1/2}$1], within their net theme group. Batches 0932, 0937, 0950 and 1013 were printed using the net theme A, while batches 1123 and 1170 were printed using the net theme B. The mean $\sigma_{UCS\text{-}L[001]}$ is about 2.0 to 2.5 times higher than $\sigma_{UCS\text{-}L[011]}$, $\sigma_{UCS\text{-}L[111]}$ and $\sigma_{y\text{-}L[\sqrt{1/2}\,\sqrt{1/2}1]}$, while the mean $\sigma_{y\text{-}L[001]}$ is about 1.8 to 2.1 times higher than $\sigma_{y\text{-}L[011]}$, $\sigma_{y\text{-}L[111]}$ and $\sigma_{y\text{-}L[\sqrt{1/2}\,\sqrt{1/2}1]}$. The mean $E_{L[001]}$ is stiffer by 1.6 to 2.1 times compared to $E_{L[011]}$, $E_{L[111]}$ and $E_{L[\sqrt{1/2}\,\sqrt{1/2}1]}$ (Table 4.4).

Looking within the net theme B group, the [001] lattices of batches 1170 and 1123 have significantly higher mean ultimate compressive strength $\sigma_{UCS\text{-}L}$, yield strength $\sigma_{y\text{-}L}$ and elastic modulus E_L than their counterpart of [011], [111] and [$\sqrt{1/2}$ $\sqrt{1/2}$1] orientation specimens. The orientations of [011], [111] and [$\sqrt{1/2}$ $\sqrt{1/2}$1] have about the same mean $\sigma_{UCS\text{-}L}$ (Figure 4.1). This is again seen with their yield strength, except for the [011] orientation having slightly lower mean $\sigma_{y\text{-}L}$ (Figure 4.2). The mean E_L for all three orientations [011], [111] and [$\sqrt{1/2}$ $\sqrt{1/2}$1] shows quite similar values with batch 1123 showing a wider spread of standard deviation for its [111] and [$\sqrt{1/2}$ $\sqrt{1/2}$1] orientation lattices (Figure 4.3).

On the other hand, for the other group batches with the net theme A, the $\sigma_{UCS\text{-}L}$ and E_L mean values between [011] and [$\sqrt{1/2}$ $\sqrt{1/2}$1] orientations does not show the trend of comparable values, except for between the batch 1013 and the single specimen data of 0932. The [011] lattice of the 0950 batch has the lowest values of $\sigma_{UCS\text{-}L}$, $\sigma_{y\text{-}L}$ and E_L, followed by the [011] lattice of 0937 when compared to the other batches within the net theme A group. It also has the largest standard deviation spread for its $\sigma_{UCS\text{-}L}$ and $\sigma_{y\text{-}L}$.

The quasi-static compressive experiment data analysis findings based on the unit cell orientation factor can be summarised below.

1. The lattice with orientation [001] has significantly higher $\sigma_{UCS\text{-}L}$, $\sigma_{y\text{-}L}$ and E_L than the other three orientations of [011], [111] and [$\sqrt{1/2}$ $\sqrt{1/2}$1].

2. The orientations [111] and [$\sqrt{1/2}$ $\sqrt{1/2}$1] have mechanical strength values that are comparable.

3. The orientation [011] lattice has comparable mechanical strength values with [111] and [$\sqrt{1/2}$ $\sqrt{1/2}$1] for some batches and also has the lowest mechanical strength values for other batches.

Figure 4.1
Ultimate Compressive Strength vs Batch Graph

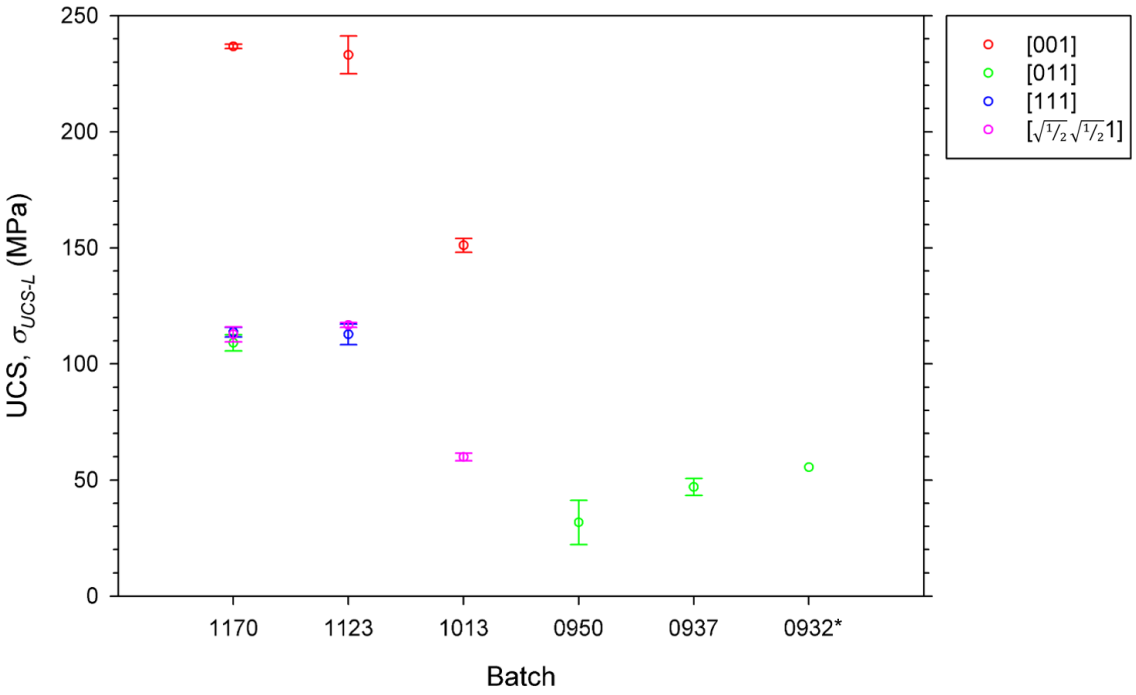

Note. Mean ultimate compressive strength versus batch graph from the data in Table 4.1. Specimen unit cell orientation is shown in legend. *Batch 0932 data point is the $\sigma_{UCS\text{-}L}$ for one specimen. Error bars represent one standard deviation of uncertainty.

Figure 4.2
Yield Strength (0.2 %) vs Batch Graph

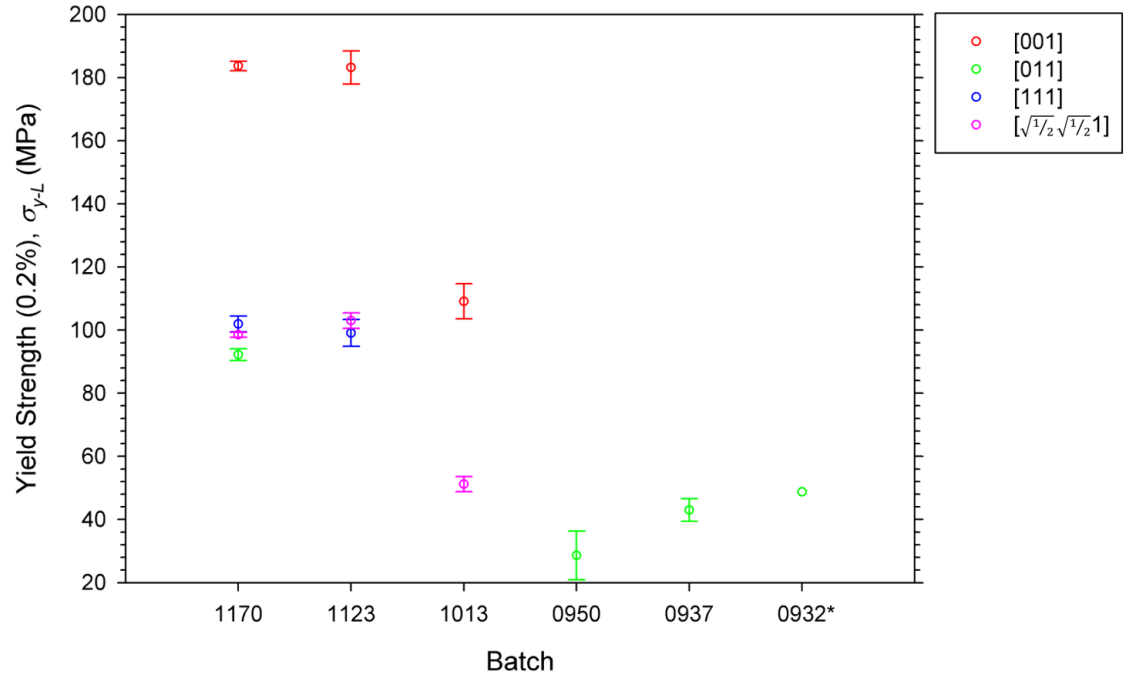

Note. Mean yield strength (0.2 %) versus batch graph from the data in Table 4.2. Specimen unit cell orientation is shown in the legend. *Batch 0932 data point is the $\sigma_{y\text{-}L}$ for one specimen. Error bars represent one standard deviation of uncertainty.

Figure 4.3
Elastic Modulus vs Batch Graph

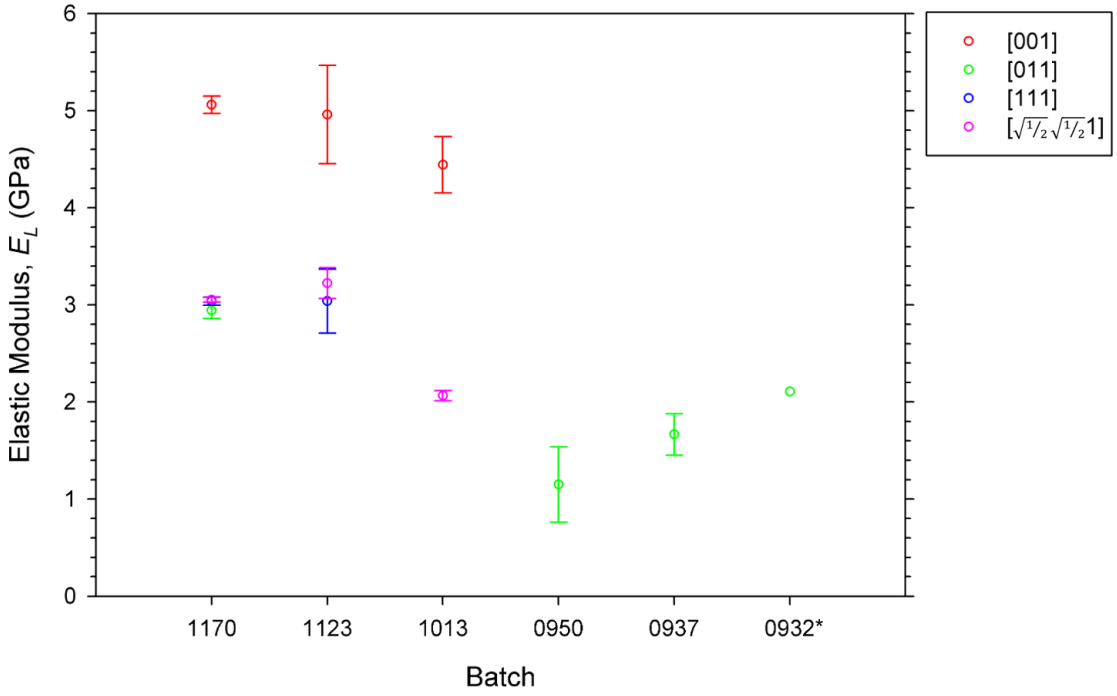

Note. Mean elastic modulus versus batch graph from the data in Table 4.3. Specimen unit cell orientation is shown in legend. *Batch 0932 data point is the E_L for one specimen. Error bars represent one standard deviation of uncertainty.

Batch variation effect on compressive strength data. The quasi-static compressive experiment data comparing for batch variation are shown in Figure 4.4, Figure 4.5 and Figure 4.6. The batches of 1170 and 1123 in the net theme B group show higher mechanical strength values of $\sigma_{UCS\text{-}L}$, $\sigma_{y\text{-}L}$ and E_L than of the specimens in the batches of 0950, 0937 and 0932 in net theme A group. This shows that the net theme B used in the EB-PBF process produces lattices with significantly stronger quasi-static compressive properties.

Comparing the batch variation within the net theme A group, it can be observed that batch 0950 is significantly weaker with a higher standard deviation spread than the other batches of 0937 and 0932, with the same [011] orientation and 1013 with [$\sqrt{1/2}\,\sqrt{1/2}1$] orientation. On the other hand, comparing the batch variation within the net theme B group of 1170 and 1123, the mean mechanical values of $\sigma_{UCS\text{-}L}$, $\sigma_{y\text{-}L}$ and E_L are pretty similar, but the batch 1123 have a larger standard deviation spread than 1170. This indicates that within the same net theme A, the lattice specimen printed shows significant variation in its quasi-static compressive properties, whereas minor variation can be observed when using the net theme B.

The quasi-static compressive experiment data analysis findings based on the batch variation factor can be summarised below.

1. The lattice specimens made using the net theme B have significantly higher $\sigma_{UCS\text{-}L}$, $\sigma_{y\text{-}L}$ and E_L than the lattice specimens made using net theme A.

2. There are variations in the quasi-static compressive values for both net themes, but net theme A has significant variation, and net theme B has minor variation.

Figure 4.4

Ultimate Compressive Strength vs Unit Cell Orientation Graph

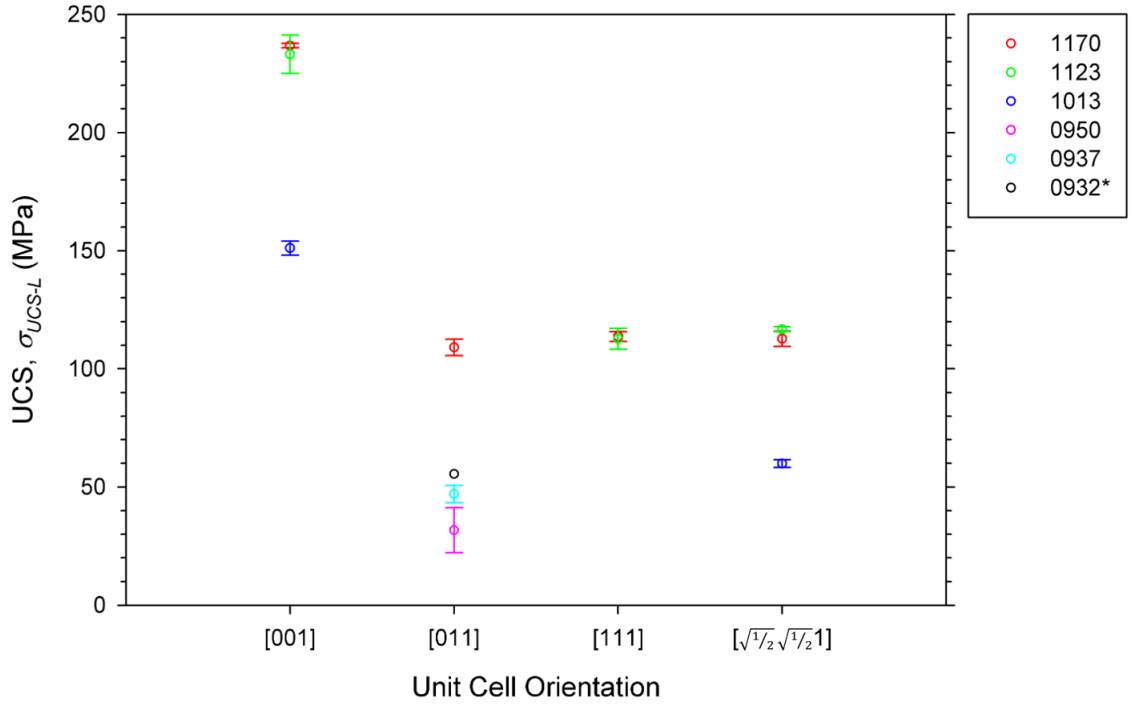

Note. Mean ultimate compressive strength versus unit cell orientation graph from the data in Table 4.1. The specimen batch is shown in legend. *Batch 0932 data point is the $\sigma_{UCS\text{-}L}$ for one specimen. Error bars represent one standard deviation of uncertainty.

Figure 4.5
Yield Strength (0.2 %) vs Unit Cell Orientation Graph

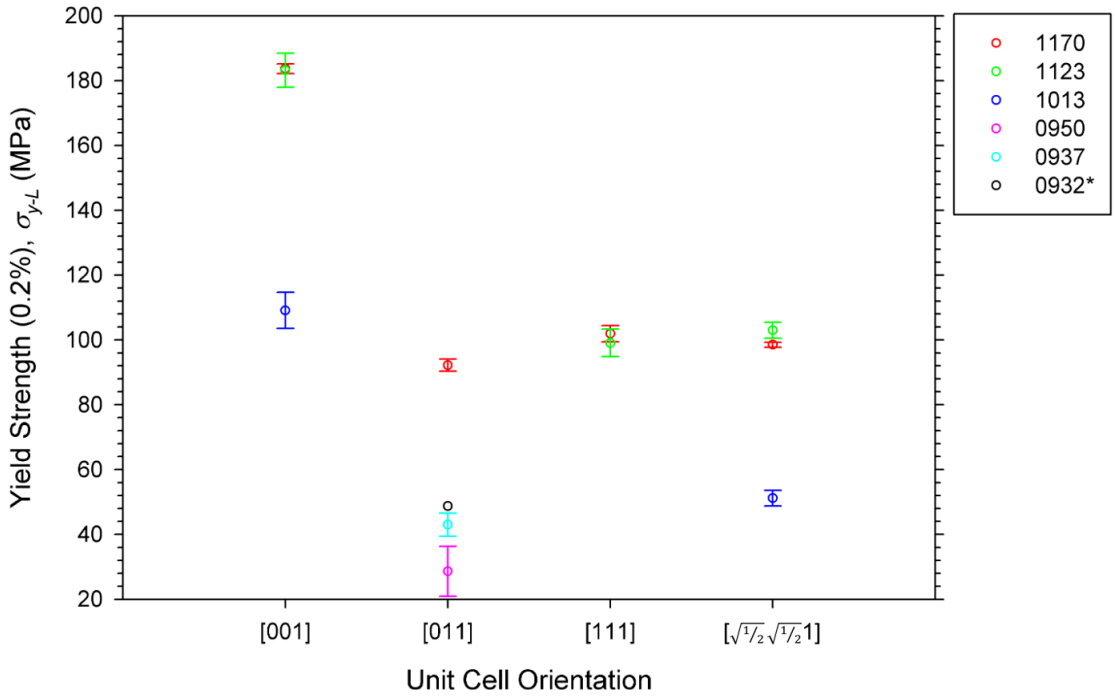

Note. Mean yield strength (0.2 %) versus unit cell orientation graph from the data in Table 4.2. The specimen batch is shown in legend. *Batch 0932 data point is the $\sigma_{y\text{-}L}$ for one specimen. Error bars represent one standard deviation of uncertainty.

Figure 4.6
Elastic Modulus vs Unit Cell Orientation Graph

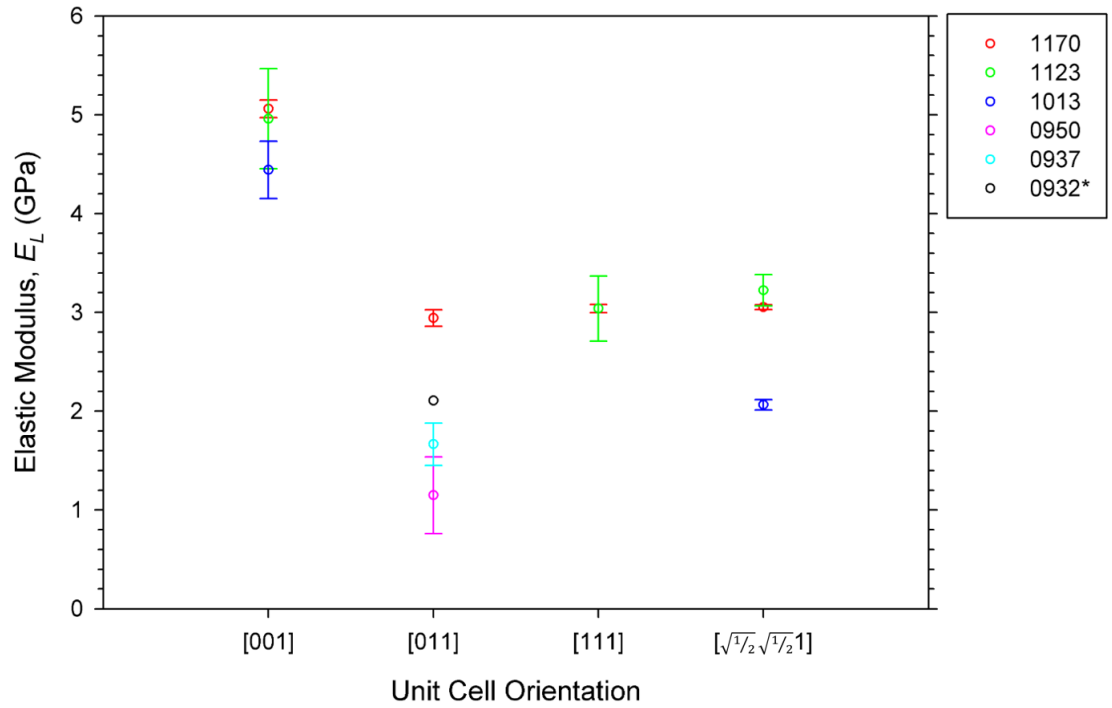

Note. Mean elastic modulus versus unit cell orientation graph from the data in Table 4.3. The specimen batch is shown in legend. *Batch 0932 data point is the E_L for one specimen. Error bars represent one standard deviation of uncertainty.

4.1.2 Quasi-static Compressive Simulation Data

Numerical analysis of quasi-static compressive was carried out on CAD lattice specimens with a simple cubic unit cell design with varied orientations to investigate the orientation effect of a perfect lattice. The simulation data of yield strength and quasi-elastic gradient for quasi-static compression of simple cubic Ti-6Al-4V lattice with varied four unit cell orientations is shown in Table 4.5 and graphically presented in Figure 4.7. The comparison of simulated quasi-static compressive data relative to the [001] and [111] orientations are shown in Table 4.6.

The simulation data shows that the orientation of [001] has a significantly higher yield strength, $\sigma_{y\text{-}SL}$ and elastic modulus, E_{SL} than the other three orientations. The yield strength of the [001] orientation, $\sigma_{y\text{-}SL[001]}$ is about 1.8 times higher than $\sigma_{y\text{-}SL[011]}$ and is about 1.5 to 1.6 times higher than $\sigma_{y\text{-}SL[111]}$ and $\sigma_{y\text{-}SL[\sqrt{1/2}\,\sqrt{1/2}1]}$. On the other hand, the elastic modulus of the [001] orientation, $E_{SL[001]}$, is about three times higher than the other three orientations.

Figure 4.7
Simulated Yield Strength (0.2 %) and Elastic Modulus vs Orientation

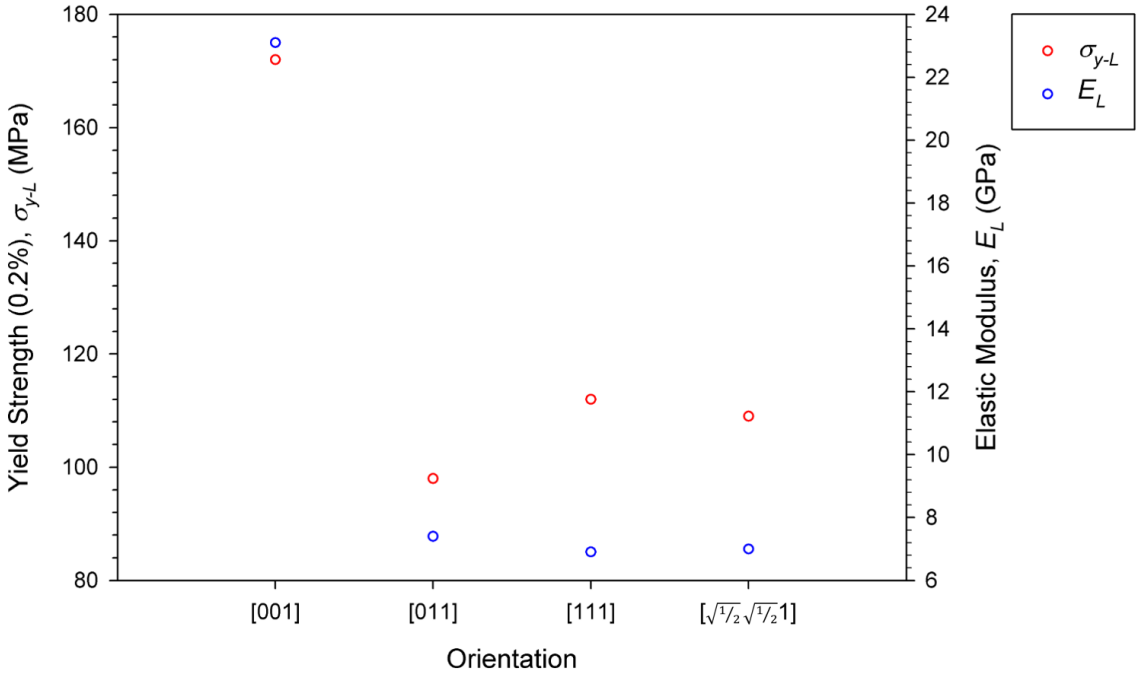

Note. Simulated yield strength (0.2 %) and elastic modulus versus orientation of unit cell based on the data from Table 4.5.

The orientation [111] has the highest yield strength compared to $\sigma_{y\text{-}SL[011]}$ and $\sigma_{y\text{-}SL[\sqrt{1/2}\,\sqrt{1/2}1]}$, which are about 1.14 and 1.03 times higher when compared respectively. However, the [111] orientation has the lowest elatic modulus compared to $E_{SL[011]}$ and $E_{SL[\sqrt{1/2}\,\sqrt{1/2}1]}$. The [011] orientation has the weakest yield strength but has a slightly higher elastic modulus compared to [111] and [$\sqrt{1/2}\,\sqrt{1/2}1$] orientations. However, when compared overall, their differences are not as signi-

ficant as those observed compared to the orientation [001].

The quasi-static compressive simulation data analysis findings based on the batch variation factor can be summarised below.

1. The lattice with [001] orientation has significantly higher $\sigma_{y\text{-}SL}$ (1.5 to 1.8 times higher) and E_{SL} (3.1 to 3.4 times higher) than the other orientations.

2. The lattice with [111] and [$\sqrt{1/2}$ $\sqrt{1/2}$1] orientations have almost similar $\sigma_{y\text{-}SL}$ and E_{SL} values.

3. The lattice with [011] orientation has a slightly $\sigma_{y\text{-}SL}$ than the other orientations but have a comparable E_{SL} value with the [111] and [$\sqrt{1/2}$ $\sqrt{1/2}$1] orientations.

Table 4.5
Numerical Analysis Data for Quasi-static Compression of Lattice

Orientation	Yield Strength (0.2 %), $\sigma_{y\text{-}SL}$ (MPa)	Elastic Modulus, E_{SL} (GPa)
[001]	172	23.1
[011]	98	7.4
[111]	112	6.9
[$\sqrt{1/2}$ $\sqrt{1/2}$1]	109	7.0

Note. Simulated quasi-static compressive data for simple cubic Ti-6Al-4V lattice with different unit cell orientations.

Table 4.6
Simulated Quasi-static Compression Data Comparison

Orientation Comparison	Yield Strength Factor	Elastic Modulus Factor
[001]/[011]	1.76	3.12
[001]/[111]	1.54	3.35
[001]/[$\sqrt{1/2}$ $\sqrt{1/2}$1]	1.58	3.30
[111]/[011]	1.14	0.93
[111]/[$\sqrt{1/2}$ $\sqrt{1/2}$1]	1.03	0.99

Note. Comparison of simulated quasi-static compressive data relative to [001] and [111] orientations for simple cubic Ti-6Al-4V lattice, based on data in Table 4.5.

4.1.3 Lattice Structure and Collapse Data

Lattice deformation and collapse modes. During the quasi-static compressive experiment, videos were taken when the specimens were loaded. From this, two images of the specimens were taken before loading and after the collapse, which is shown in Figure 4.8, Figure 4.9, Figure 4.10 and Figure 4.11. The load-bearing struts in the lattice with [001] orientation have a buckling deformation mode when under compressive loading, as observed in Figure 4.8. As the load-bearing struts deform and buckle, the weakest layer of vertical struts on a side within the lattice collapses, and the whole [001] lattice also shows a buckling behaviour as seen in the after collapse images in Figure 4.8b.

Figure 4.8
Fracture and Collapse of [001] *Lattice Specimen*

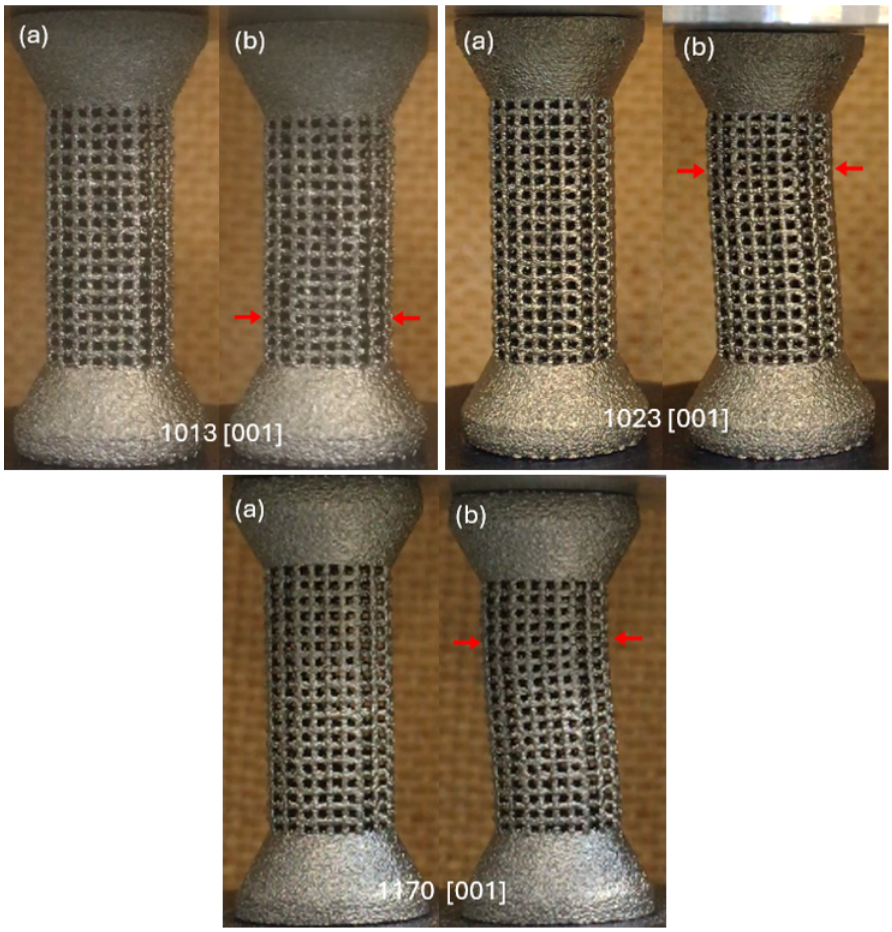

Note. Images of the [001] lattice specimens when (a) before loading and (b) after fracture and collapse. Specimens show buckling deformation in load-supporting struts before fracture and collapse. Arrows show the location with collapsed struts in the lattice specimen.

The load-bearing struts in the [011] orientation lattice specimens show a bending deformation mode when under compressive loading, as observed in Figure 4.9. As the lattice specimen is

loaded under compressive load, a plane of collapsing struts can be observed, and the plane is about the 45°, corresponding to the [011] orientation of the simple cubic unit cell in the lattice. In contrast with the [001] lattice, the [011] lattice slides as the load-bearing struts collapse like a shear effect. In this state, the specimens either fracture and slide off into halves, or the fractured lattice surfaces meet and interlock, allowing for load support to continue.

Figure 4.9
Fracture and Collapse of [011] *Lattice Specimen*

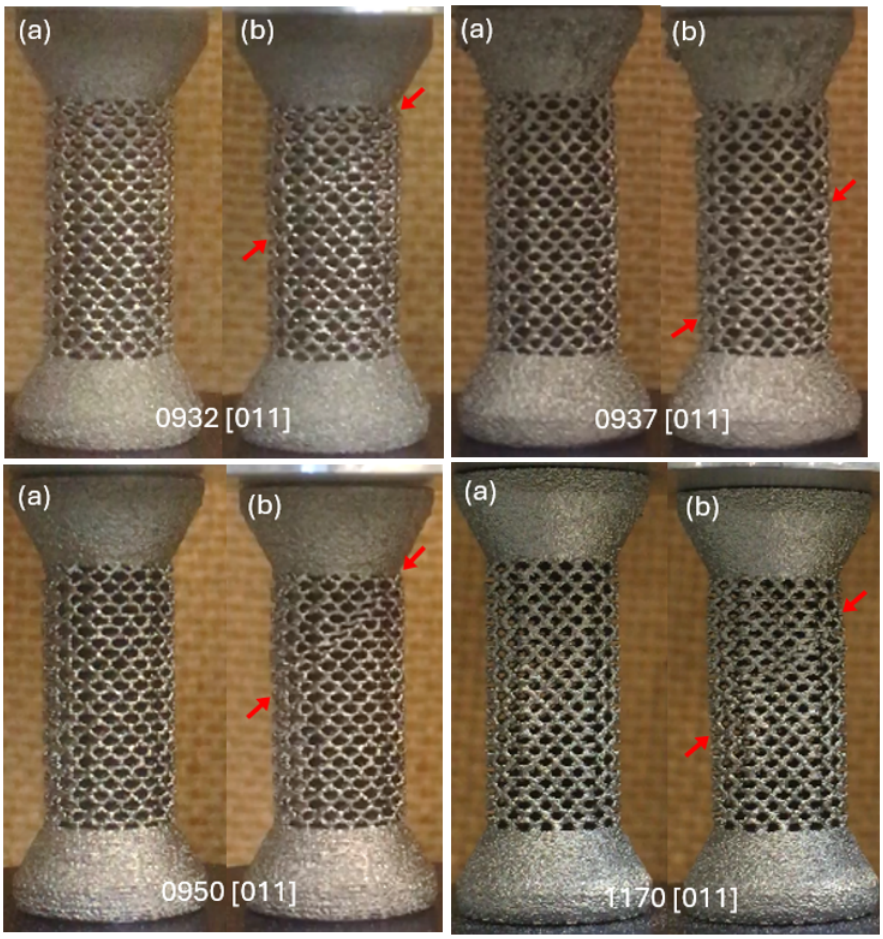

Note. Images of the [011] lattice specimens when (a) before loading and (b) after fracture and collapse. Specimens show bending deformation in load-supporting struts before fracture and collapse. Arrows show the location with collapsed struts in the lattice specimen.

For the lattice specimens with [111] and [$\sqrt{1/2}$ $\sqrt{1/2}$1] orientations, bending deformation mode can be observed as well as the lattice during the quasi-static compressive loading test (Figure 4.10 and Figure 4.11). Instead of a single plane of collapsing struts that are observed in [011], two planes of collapsing struts can be observed from one side of the lattice during the fracture of load-bearing struts in [111] and [$\sqrt{1/2}$ $\sqrt{1/2}$1] specimens. These collapsing planes form and intersect within the lattice, which results in a continuous layer of fractured load-bearing struts. A single

plane-like of the collapsing strut can also be observed for [111] lattice in Figure 4.10. However, because of the [111] orientation, a single plane of collapsed struts can not be formed. Instead, adjacent struts collapse together and form a single plane-like. Unlike the shear-like fracture and collapse seen in the [011] lattice, the [111] and [$\sqrt{1/2}$ $\sqrt{1/2}$1] lattices does not slide off after fracture and always interlock, which allows for continuous load support.

The findings of examining specimen images during the quasi-static compressive test to understand lattice deformation and collapse modes are summarised below.

1. The deformation mode of the load-bearing struts in [001] is buckling and for [011], [111] and [$\sqrt{1/2}$ $\sqrt{1/2}$1] are bending.

2. The [001] lattice specimens collapse from one side in the horizontal plane following the orientation and cause the overall lattice to buckle.

3. The specimens [011], [111] and [$\sqrt{1/2}$ $\sqrt{1/2}$1] collapse at an angle following the orientation of the lattice, with [011] showing single plane and [111] and [$\sqrt{1/2}$ $\sqrt{1/2}$1] showing multiple planes.

Figure 4.10
Fracture and Collapse of [111] *Lattice Specimen*

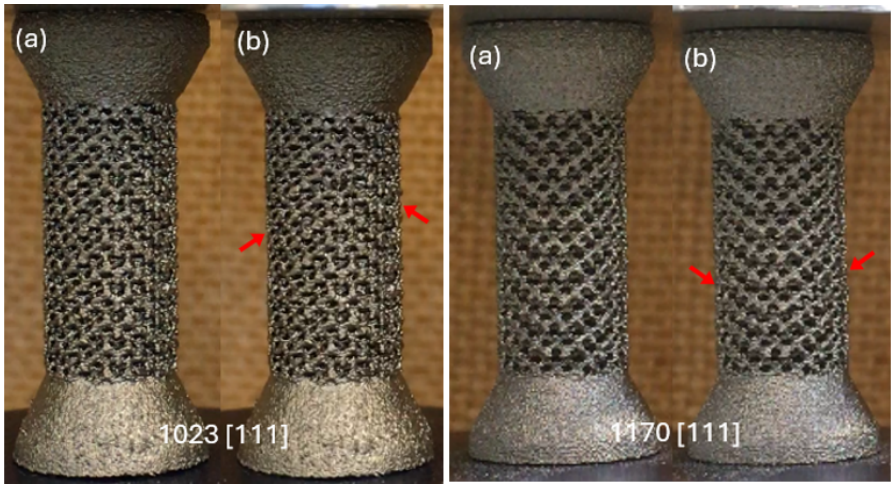

Note. Images of the [111] lattice specimens when (a) before loading and (b) after fracture and collapse. Specimens show bending deformation in load-supporting struts before fracture and collapse. Arrows show the location with collapsed struts in the lattice specimen.

Figure 4.11
Fracture and Collapse of [$\sqrt{1/2}$ $\sqrt{1/2}$1] *Lattice Specimen*

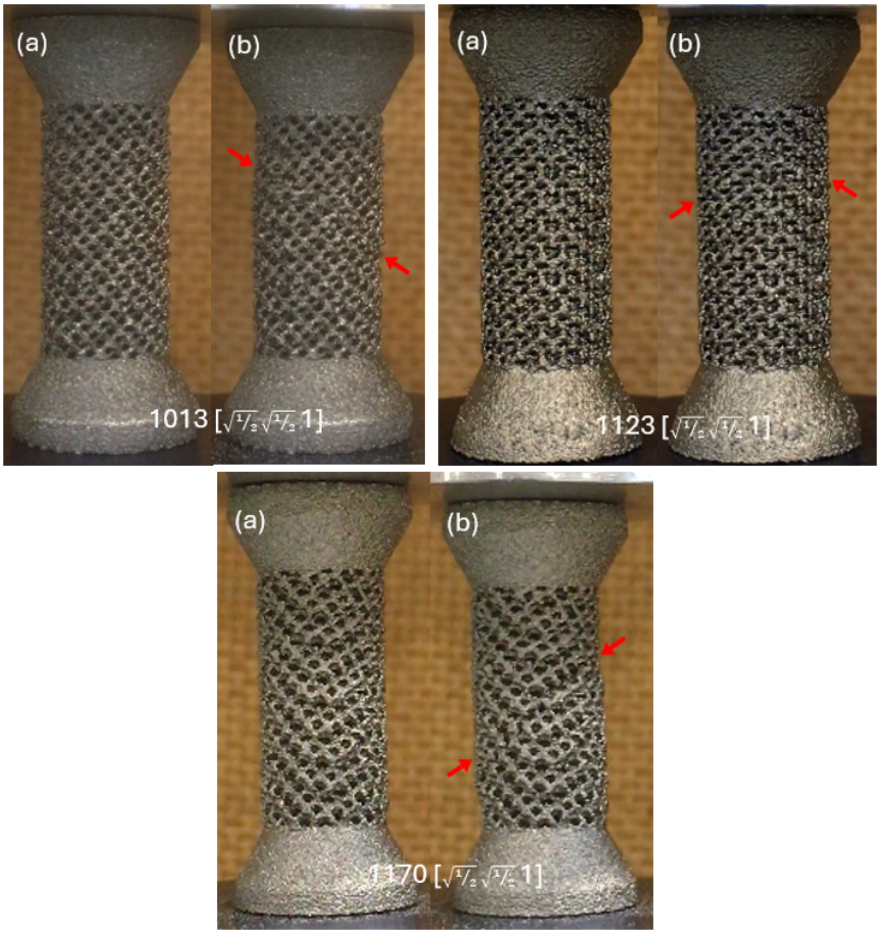

Note. Images of the [$\sqrt{1/2}$ $\sqrt{1/2}$1] lattice specimens when (a) before loading and (b) after fracture and collapse. Specimens show bending deformation in load-supporting struts before fracture and collapse. Arrows show the location with collapsed struts in the lattice specimen.

Strut thickness and irregularities. The printed lattice specimens were inspected using a scanning electron microscope to study their lattice structure, strut thickness and irregularities or defects. Figure 4.12 shows the SEM images of the lattice specimens from batches 0932, 0937, 0950 and 1013, which were all printed using the net theme A with the EB-PBF process. It can be observed that the 0950 and 0937 batches have significantly more partially melted powder all over the lattice structure than the other 0932 and 1013 batches. Their partially melted powders are mostly more spherical than the partially melted powder of 0932 and 1013, meaning that less than one-third of the powder particles were melted spherically. The 1013 and 0932 specimens can be observed to have larger struts than the other two batches.

In Figure 4.13, the SEM images of [011] lattice specimens from 0937 and 0950 are compared, and the sides of the lattice specimens are shown. Overall, the struts of the 0937 lattice are thicker than the struts of the 0950 lattice. The effective strut thickness, $d_{s\text{-}e}$, is the smallest thickness

within the strut, where stress concentration and deformation will occur when the lattice specimen is loaded. It can be observed that the smallest $d_{s\text{-}e}$ in the 0950 batch specimen is much smaller than the 0937 batch specimen. This was also observed in the estimated $d_{s\text{-}e}$ measurements data in Figure 4.14, where the batch 0950 have $d_{s\text{-}e}$ that are significantly smaller than of 0937. The $d_{s\text{-}e}$ measurement estimation is based on the SEM image, as shown in Figure 4.13, where the number indicates the location of the strut where the measurement was taken.

Figure 4.12
SEM Images of Lattice Specimens with Net Theme A

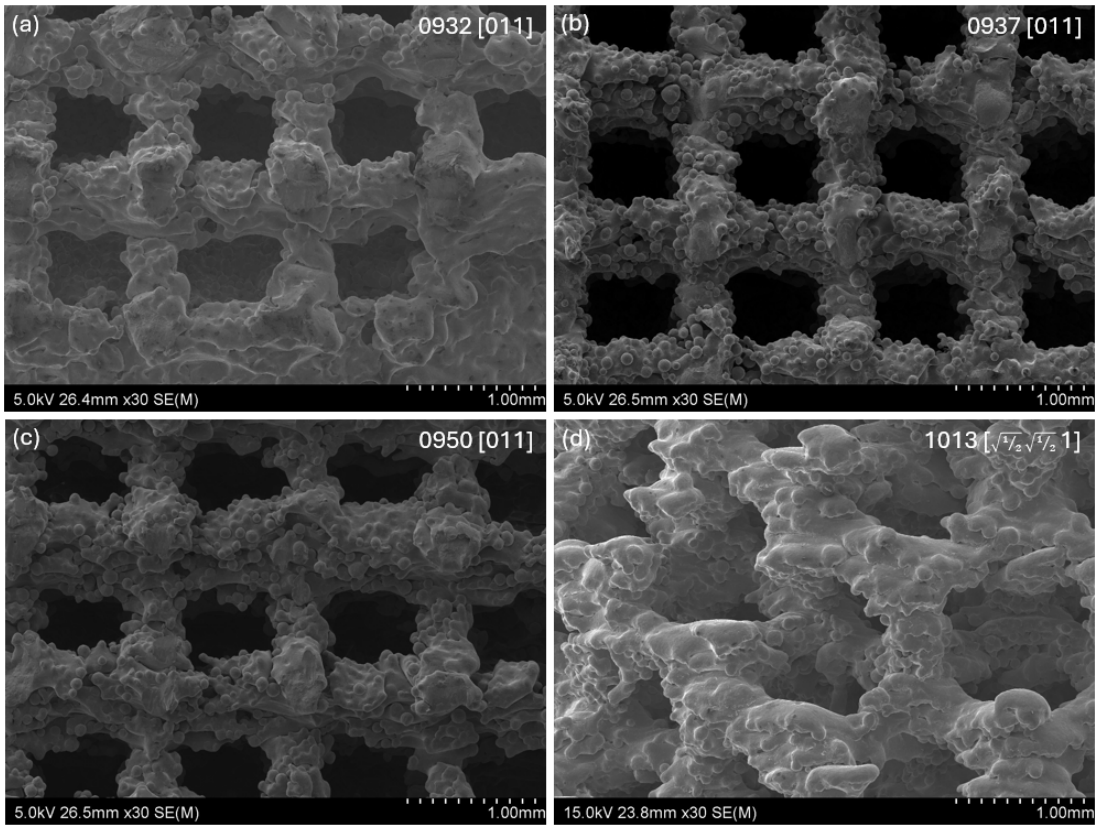

Note. SEM images of the lattice specimens from batch 0932, 0937, 0950 and 1013. The figures in (a), (b) and (c) show the [011] lattice surface of the collapsed and fractured plane. The figure (d) shows the side of the [$\sqrt{1/2}$ $\sqrt{1/2}$1] lattice specimen. The net theme A was used to print all the lattice specimens shown.

The SEM images of lattice specimens from batches 1013 and 1123 with [011] orientation are compared in Figure 4.15. The same batch of lattice specimens but with [$\sqrt{1/2}$ $\sqrt{1/2}$1] orientation are compared in Figure 4.16. The sides of the lattice specimens are shown in all figures. The batch 1013 specimens were printed using the net theme A, and the batch 1123 specimens were printed using the net theme B. Overall, the struts in the lattice specimens from batch 1123 are significantly larger than those from batch 1013. The batch 1123 struts show a more combined melt than batch 1013, where resolidified melt layers are more visible within the struts, resulting in a more irregular

strut lattice and smaller $d_{s\text{-}e}$.

The strut thickness and irregularities examination by SEM image findings are summarised below.

1. The net theme B results in lattice specimens with generally larger $d_{s\text{-}e}$ than those with net theme A.

2. The specimens with net theme B show significant variations in $d_{s\text{-}e}$ and irregularities between the batches of 0932 and 1013 with 0937 and 0950.

3. The specimen from batch 0950 has a significantly smaller $d_{s\text{-}e}$ than 0937.

Figure 4.13
SEM Images of 0937 [011] *and 0950* [011] *Lattice Specimens*

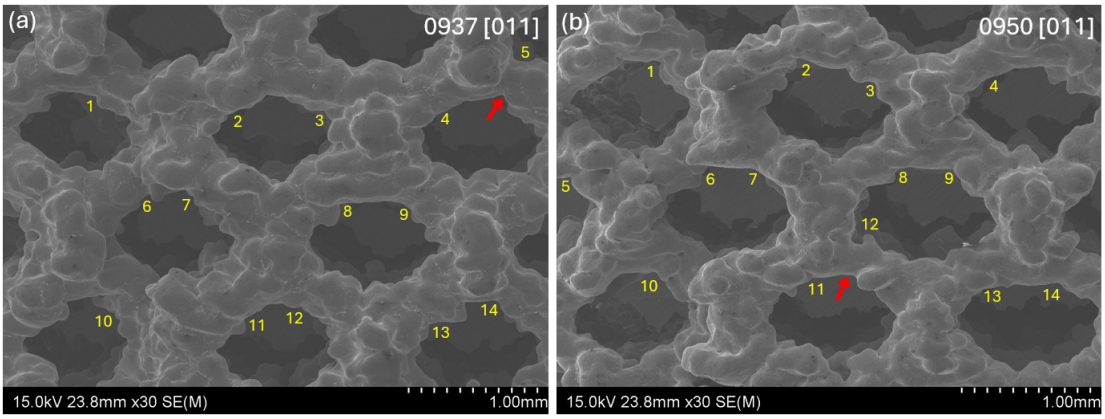

Note. SEM images of sides of the (a) 0937 [011] vs (b) 0950 [011] lattice specimens. Net theme A was used to print both specimens. Arrows showing the smallest effective strut diameter observed, which was 0.295 mm for 0937 and 0.274 mm for 0950. The numbers in yellow indicate the location of the strut measurement taken.

Figure 4.14
Effective Strut Diameter Estimation Measurements of Specimen Batch 0937 and 0950

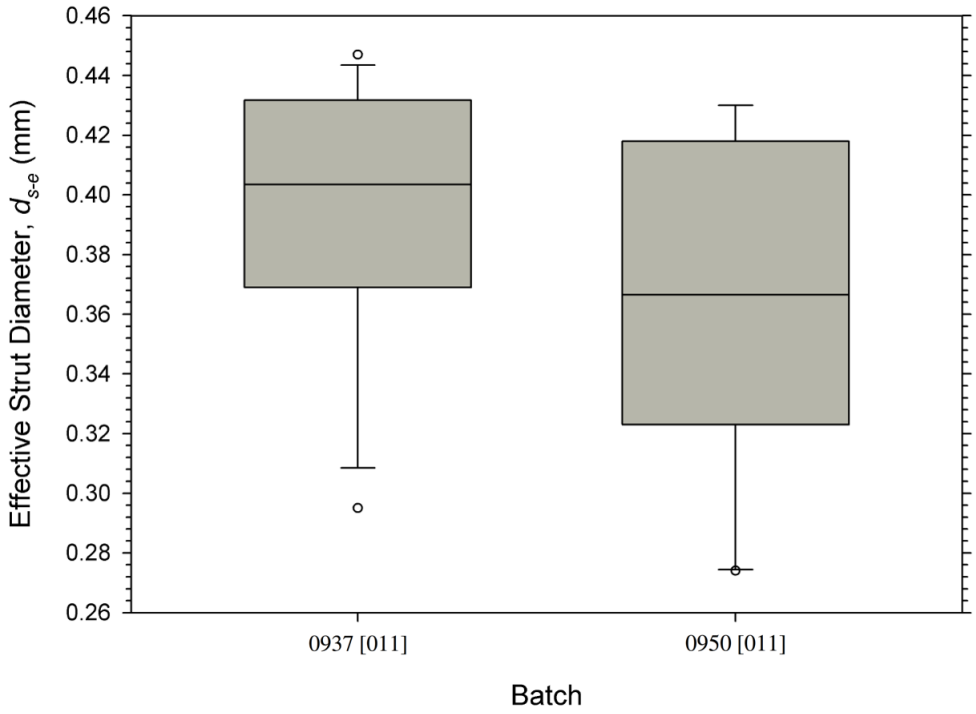

Note. Box plot of the estimated effective strut diameter or thickness, d_{s-e} measurements from the SEM images in Figure 4.13 for the specimen from batch 0937 [011] and 0950 [011]. Net theme A was used to print both specimens.

Figure 4.15
SEM Images of 1013 [001] *and 1123* [001] *Lattice Specimens*

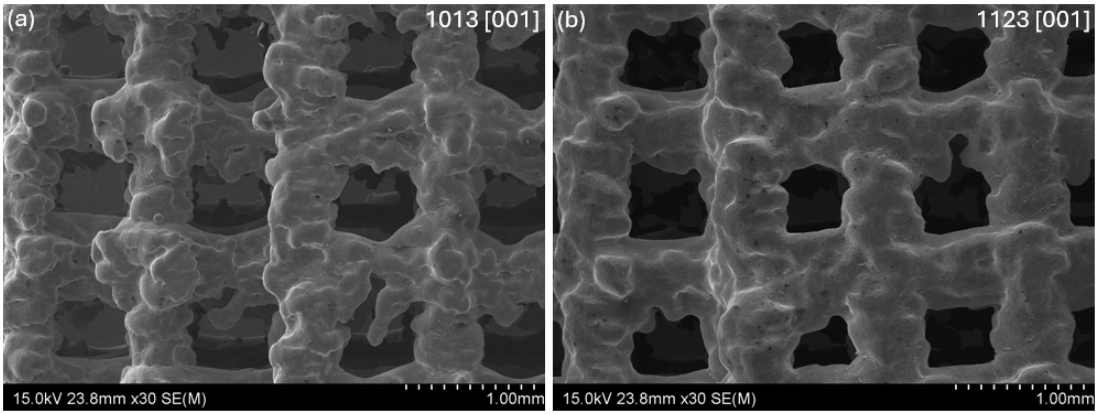

Note. SEM images of sides of the 1013 [001] and 1123 [001] lattice specimens. Net theme A was used to print the specimens from batch 1013, and net theme B was used to print the specimens from batch 1123.

Figure 4.16
SEM Images of 1013 [$\sqrt{1/2}$ $\sqrt{1/2}$1] *and 1123* [$\sqrt{1/2}$ $\sqrt{1/2}$1] *Lattice Specimens*

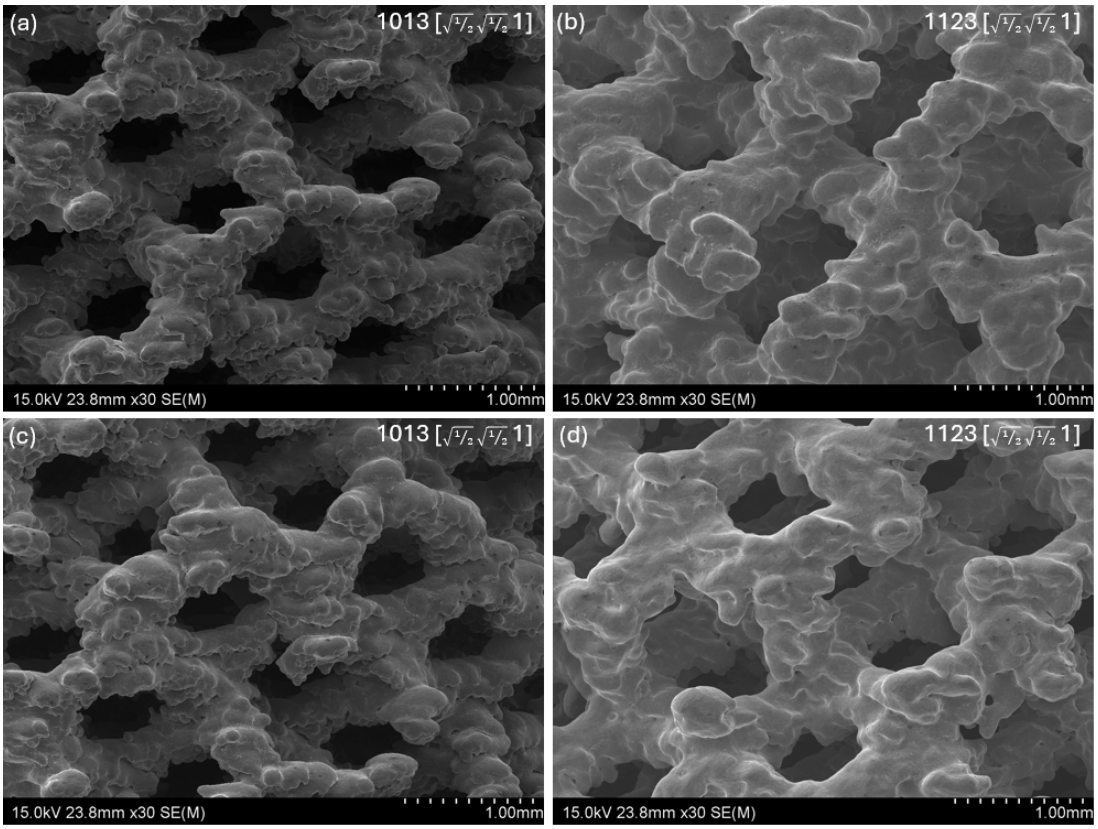

Note. SEM images of sides of the 1013 [$\sqrt{1/2}$ $\sqrt{1/2}$1] and 1123 [$\sqrt{1/2}$ $\sqrt{1/2}$1] lattice specimens. The net themes of A and B were used to print specimens 1013 and 1123, respectively.

4.1.4 Orientation Effect on Compressive Strength Analysis

The quasi-static compressive test on the simple cubic Ti-6Al-4V lattice structure made with EB-PBF has been carried out in this study, and the results are presented in Section 4.1.1. The simulation results of the quasi-static compressive test are presented in Section 4.1.2, and the collapse data of the lattice specimen with the SEM inspection of the lattice structure are presented in Section 4.1.3. This section will discuss the findings and analysis based on the unit cell orientation effect. The lattice specimens were all printed with the build direction parallel to the loading direction to isolate the unit cell orientation effect.

The [001] **unit cell orientation has the highest lattice mechanical strength**. The lattice with orientation [001] has significantly higher ultimate compressive strength $\sigma_{UCS\text{-}L}$, yield strength $\sigma_{y\text{-}L}$ and elastic modulus E_L than the other three orientations of [011], [111] and [$\sqrt{1/2}$ $\sqrt{1/2}$1] when compared within their net theme groups for the experimental data. The [001] unit cell orientation is the simple cubic unit cell without rotation with load-supporting struts parallel to the loading direction. The results from the simulation results of the quasi-static compressive test are also in agreement, where the simulation showed that lattice with [001] orientation has significantly higher yield strength $\sigma_{y\text{-}SL}$ (1.5 to 1.8 times higher) and elastic modulus E_{SL} (3.1 to 3.4 times higher) than the other orientations.

This higher compressive strength and elastic modulus can be attributed to the deformation mode of the [001] lattice. As explained by Deshpande et al. (2001) and following the Gibson-Ashby model (Gibson & Ashby, 1997), the load-bearing strut's dominant deformation mode affects the lattice's compressive strength, where a stretching-dominated deformation lattice will have a higher compressive strength and higher elastic modulus value than a lattice with bending dominated deformation. The deformation mode of the load-bearing struts in [001] is a stretching-dominated deformation where the vertical load-bearing struts buckle under a compression load, as observed in the image taken from the video capture of the specimen during the test in Figure 4.8. The [001] lattice specimens were observed to have collapsed from one side in the horizontal plane, following the orientation, and caused the overall lattice to buckle.

On the other hand, the deformation mode of the load-bearing struts in lattice specimens with the orientations of [011], [111] and [$\sqrt{1/2}$ $\sqrt{1/2}$1] are bending-dominated, as observed in Figure 4.9, Figure 4.10, and Figure 4.11, which explains the lower compressive strength and lower elastic modulus value. The specimens [011], [111] and [$\sqrt{1/2}$ $\sqrt{1/2}$1] collapse at an angle following the orientation of the lattice, with [011] showing single plane and [111] and [$\sqrt{1/2}$ $\sqrt{1/2}$1] showing multiple planes. The verticle struts in the [001] orientation specimen lattice with buckling deformation

mode will have compressive stress within the struts, while the struts at angles with the loading direction for [011], [111] and [$\sqrt{1/2}$ $\sqrt{1/2}$1] orientations specimens with bending deformation mode will have both compressive and tensile stresses.

The orientation [111] **and** [$\sqrt{1/2}$ $\sqrt{1/2}$1] **is comparable in mechanical strength**. The lattice with [111] and [$\sqrt{1/2}$ $\sqrt{1/2}$1] unit cell orientations have almost similar $\sigma_{UCS\text{-}L}$, $\sigma_{y\text{-}L}$, and E_L values obtained from the experiment when comparing within the batches in the net theme B. These experimental results also agree with the quasi-static compressive simulation results, where the $\sigma_{y\text{-}SL}$ and E_{SL} values are almost equal. The simple cubic unit cell with [111] orientation has its three struts at equal angles facing both upwards and downwards, while the [$\sqrt{1/2}$ $\sqrt{1/2}$1] has only two out of the three struts at equal angles. The [$\sqrt{1/2}$ $\sqrt{1/2}$1] angle was selected due to simplicity of rotating 45° at the x-axis and y-axis, while the [111] was selected for its equal angles.

The deformation mode of three load-bearing struts is bending dominated and is the same for both [111] and [$\sqrt{1/2}$ $\sqrt{1/2}$1] orientations with their collapse behaviour under compressive load being similar as well, with either a single plane or multiple planes that intersected, following the angle of the unit cell orientation. These would explain the minimum differences between their $\sigma_{UCS\text{-}L}$, $\sigma_{y\text{-}L}$, and E_L values, as well as their simulated $\sigma_{y\text{-}SL}$ and E_{SL} values.

The orientation [011] **has a mix of comparable and non-comparable compressive strength to** [111] **and** [$\sqrt{1/2}$ $\sqrt{1/2}$1]. The orientation [011] lattice has comparable $\sigma_{UCS\text{-}L}$, $\sigma_{y\text{-}L}$, and E_L values with the [111] and [$\sqrt{1/2}$ $\sqrt{1/2}$1] orientation for some batches and also has the lowest mechanical strength values for other batches. The mechanical strength and elastic modulus of the [011] specimens are comparable for all batches within the net theme B group and batches 1013 and 0932 within the net theme A group. The [011] specimens from 0950 and 0937 are significantly lower for $\sigma_{UCS\text{-}L}$, $\sigma_{y\text{-}L}$, and E_L values compared to 1013 and 0932 when looking at specimens within the net theme A. The [011] specimens results from 0950 and 0937 are attributed to be influenced more by their batch variation effect than the unit cell orientation effect.

Examining the quasi-static compressive simulation results (Figure 4.7), the orientation [011] lattice has a slightly lower $\sigma_{y\text{-}SL}$ value than the [111] and [$\sqrt{1/2}$ $\sqrt{1/2}$1] orientations but has a comparable E_{SL} value. The simple cubic unit cell with [011] orientation has two load-supporting struts per node, which would explain the slightly lower $\sigma_{y\text{-}SL}$ value due to one less strut supporting the load compared to [111] and [$\sqrt{1/2}$ $\sqrt{1/2}$1] orientations. These are in agreement with the experimental result when comparing the [011] specimen with [111] and [$\sqrt{1/2}$ $\sqrt{1/2}$1] specimens for batches within their own net theme groups, excluding the batch 0950 and 0937. The [011] specimens always collapse in a single plane at an angle of 45°, following the orientation of the unit

cell. The [011] orientation also has a bending-dominated deformation during loading as observed in Figure 4.9, which is why the mechanical strength values are closer to the [111] and [$\sqrt{1/2}$ $\sqrt{1/2}$1] orientations.

Unit cell orientation effect on compressive strength overall findings. Based on the analysis and discussion above, it is clear that the unit cell orientation affects the mechanical behaviour of a simple cubic Ti-6Al-4V lattice structure made with EB-PBF under compressive load. The non-rotated simple cubic unit cell of [001] orientation still behaves with a stretching-dominated deformation, even with the small strut diameter and pore diameter that follows the osteoconductive requirement. The [001] orientation of stretching-dominated deformation is significantly stronger than the [011], [111] and [$\sqrt{1/2}$ $\sqrt{1/2}$1] orientations with bending-dominated deformation, which are in agreement with the quasi-static compressive simulation results.

The simple cubic lattice specimens with [001] orientation of batch 1123 and 1170 have the mechanical strength values that could be a good match for biomedical bone implant, where the mean $\sigma_{UCS\text{-}L}$ for the lattice specimen is of about 235 MPa, which slightly exceeds the compressive strength of the cortical bone of 205 MPa (Table 2.1), ensuring the ability to support load. While the mean E_L for the lattice specimen is about 5 GPa, which is lower than the elastic modulus of the cortical bone of 17.9 GPa (longitudinal) and 10.1 (transverse) but higher than the elastic modulus of the trabecular bone of 0.44 GPa (femur), which would prevent the risk for stress shielding.

4.1.5 Batch Variation Effect on Compressive Strength Analysis

The quasi-static compressive test on the simple cubic Ti-6Al-4V lattice structure made with EB-PBF has been carried out in this study, and the results are presented in Section 4.1.1. The simulation results of the quasi-static compressive test are presented in Section 4.1.2, and the collapse data of the lattice specimen with the SEM inspection of the lattice structure are presented in Section 4.1.3. This section will discuss the findings and analysis based on the batch variation effect. The batches were printed randomly and subjected to the production schedule and the build chamber space availability. This gives the printed samples a batch variation factor that would exist with parts produced in an industrial production setting.

Batch 0950 and 0937 are significantly weaker. The lattice specimen from batch 0950 and 0937 have substantially lower $\sigma_{UCS\text{-}L}$, $\sigma_{y\text{-}L}$, and E_L values when compared to the lattice specimen from batch 1013 and 0932, which are all using the same net theme A during the EB-PBF print process. This was found to be unrelated to the unit cell orientation effect, as discussed in the previous section, as the other batches of 1013 and 0932 seem comparable and higher in mechanical

strength values. The spread in the mechanical values for 0950 and 0937 is also larger when compared to 1013 [$\sqrt{1/2}$ $\sqrt{1/2}$1].

This may be explained by examining the SEM images of the specimens from all four batches with net Theme A, as shown in Figure 4.12. The print quality for the 0950 and 0937 specimens seems worse than that of the 0932 and 1013 batches. The more partially melted powder can be observed with the 0950 and 0937 specimens than the other two. Also, the 0950 and 0937 lattice structures seem to have melt layers that are less fused with each other, especially in 0950, where melt layers are more apparent with more spaces. Since all of these batches had the same net theme A used for their printing, the print quality variation observed can be attributed to the batch variation, which may be from the powder condition due to powder reuse and the overall thermal profile of the build chamber due to the differences in parts printed together with the specimen.

Comparing the lattice specimen from the batch 0950 and 0937 for their $\sigma_{UCS\text{-}L}$, $\sigma_{y\text{-}L}$, and E_L values, the batch 0950 is much weaker than the batch 0937. It can also be observed that the spread variation or standard deviation of the mechanical strength and elastic modulus values for batch 0950 is significantly higher than for batch 0937. This can be attributed to the effective strut diameter, $d_{s\text{-}e}$ difference between the 0950 and 0937 batches. The specimen from batch 0950 can be observed to have a significantly smaller $d_{s\text{-}e}$ than 0937 in Figure 4.13. The estimated $d_{s\text{-}e}$ was measured from the SEM images and plotted in Figure 4.14, where it can be observed that the median measurement of the estimated $d_{s\text{-}e}$ for 0950 is significantly smaller than 0937, with 0950 having a much larger spread of $d_{s\text{-}e}$ and the smallest measurement of 0.274 mm, which is about half of the designed strut diameter of 0.5 mm. The tension stressed within the struts of a bending-dominated deformation lattice would concentrate at the $d_{s\text{-}e}$, where the strut is the weakest and a smaller $d_{s\text{-}e}$ would fail at a lower compressive loading, which is approximately following a lattice structure with a lower relative density, $\bar{\rho}$. The higher spread of $d_{s\text{-}e}$ for 0950 would indicate a lower melt pool stability during the printing process and would explain why the 0950 batch has a higher standard deviation for the $\sigma_{UCS\text{-}L}$, $\sigma_{y\text{-}L}$, and E_L values, compared to the 0937 batch.

Batch 1123 has a broader spread of mechanical strength values than 1170. The lattice specimen from the batch 1123 general shows a larger standard deviation value for their $\sigma_{UCS\text{-}L}$, $\sigma_{y\text{-}L}$, and E_L values when compared to the specimen from batch 1170 for all orientations. These batches were printed using the same net theme B. Although batch 1123 has a larger spread of their mechanical strength values, the mean values are very close to batch 1170, which means that the batch variation effect only caused the variation in mechanical strength but did not reduce it significantly.

Net theme B lattice specimens are stronger than net theme A lattice specimen. The lattice specimens made using the net theme B have significantly higher $\sigma_{UCS\text{-}L}$, $\sigma_{y\text{-}L}$ and E_L than the lattice specimens made using net theme A. Looking at the print quality of the specimen from batch 1123 with net theme B (Figure 4.15 and Figure 4.16) with the specimens from batch 1013 with net theme A, it can be observed that generally, the batch 1123 specimens have $d_{s\text{-}e}$ that much larger than the batch 1013 specimen. The specimens of batch 1123 are also observed to have better fusing between melt layers, as opposed to the lattice specimens of batches with net theme A, which shows more visibly distinctive melt layers, and some batches have poor fusing between melt layers. Therefore, the better mechanical strength in the batches with net theme B lattice specimens can be attributed to the generally larger $d_{s\text{-}e}$, which corresponds to having a lattice structure with a higher relative density, $\bar{\rho}$. It can be assumed that the melt program of net theme B for the Arcam EBM Q10plus EB-PBF machine results in a higher energy density e-beam that produces larger melt pools with better fusing between melt layers.

Batch variation effect on compressive strength overall findings. Based on the analysis and the discussion above, it can be concluded that the batch variation factor does affect the compressive strength behaviour of the simple cubic Ti-6Al-4V lattice structure made with EB-PBF. The specimens that were printed using both of the net themes A and B showed that they had been affected by the batch variation of either increasing the spread of the $\sigma_{UCS\text{-}L}$, $\sigma_{y\text{-}L}$ and E_L values or decrease their mean values. The batch variation in net theme A were more significant in affecting the compressive strength of the printed lattice specimens.

4.1.6 Compressive Strength of EB-PBF Strut-based Ti-6Al-4V Lattice

In this section, a comparison of the quasi-static compressive strength data from the experiment done in this study and the data from the literature for compressive strength data of EB-PBF strut-based Ti-6Al-4V lattice was carried out as shown in Figure 4.17 and Figure 4.18. Most of the compressive strength test data from the literature did not have their yield strength data. Therefore, only ultimate compressive strength, $\sigma_{UCS\text{-}L}$ and elastic modulus, E_L data are compared. The mechanical strength of lattice structures depends on their relative density or porosity. Thus, to make the literature data and experimental data comparable, the $\sigma_{UCS\text{-}L}$ and E_L values were plotted against their relative densities, $\bar{\rho}$. As the $\bar{\rho}$ increases, it is expected that the $\sigma_{UCS\text{-}L}$ and E_L values also increases. The $\bar{\rho}$ or porosity, ϕ values are either the designed CAD or the measured value.

Figure 4.17 shows the $\sigma_{UCS\text{-}L}$ versus $\bar{\rho}$ graph for literature and experimental data. The range of $\bar{\rho}$ of the data from literature is 0.06 for the lowest to 0.05 for the highest. The most common unit

cell designs selected are the rhombic dodecahedron (r-dodecahedron) and simple cubic. A general trend of increasing $\sigma_{UCS\text{-}L}$ as $\bar{\rho}$ increases can be observed, which follows the Gibson-Ashby model (Gibson, 2003). However, the experimental data from two other data points in the literature does not follow this general trend.

Figure 4.17
Ultimate Compressive Strength vs Relative Density for Literature and Experiment

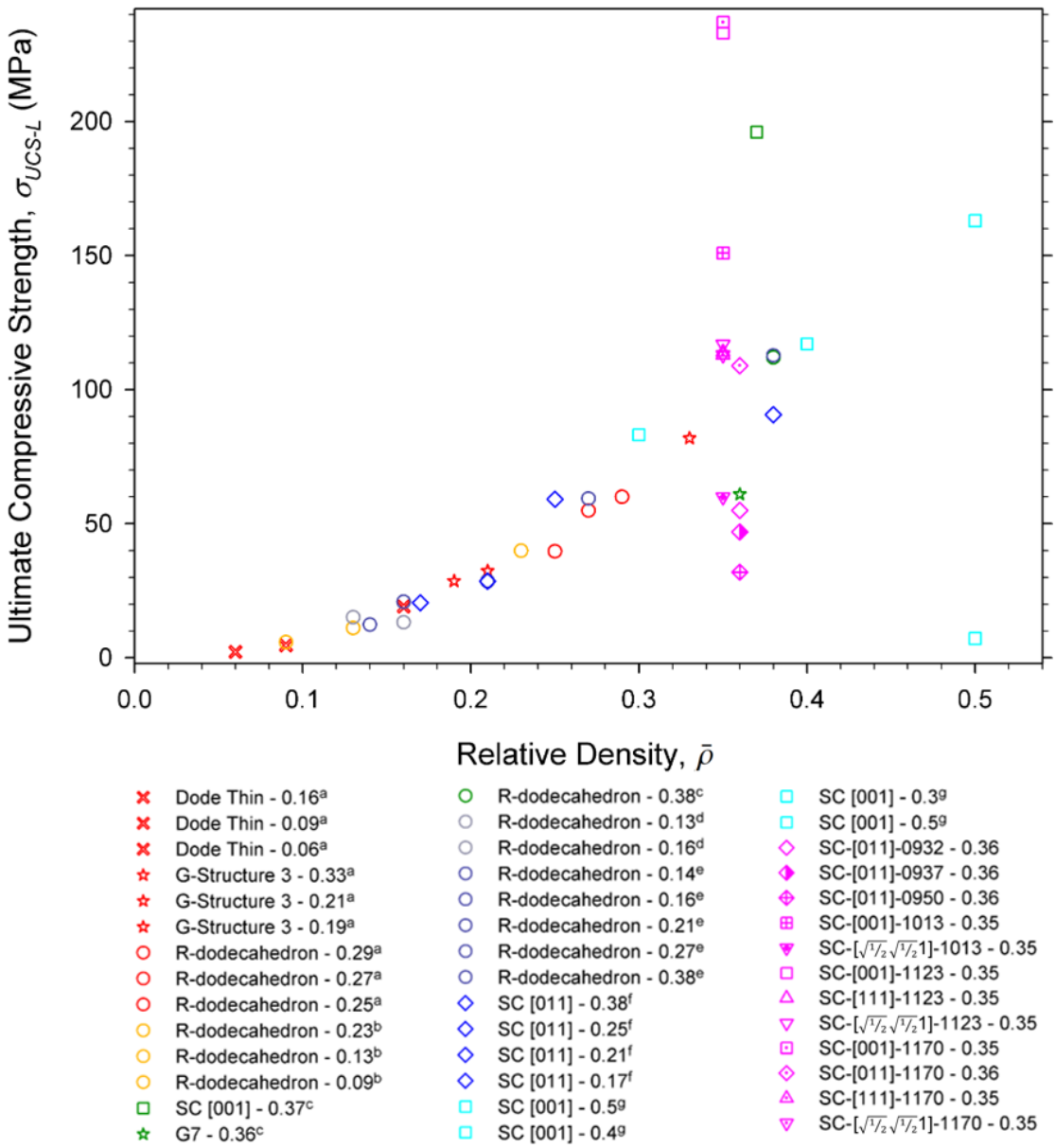

Note. Ultimate compressive strength, $\sigma_{UCS\text{-}L}$ versus relative density, $\bar{\rho}$ graph based on the data in Table 4.1 and the studies of [a]Del Guercio et al. (2021a), [b]Epasto et al. (2019), [c]Zhao et al. (2016), [d]Xiao et al. (2015), [e]Cheng et al. (2012), [f]Li et al. (2012) and [g]Parthasarathy et al. (2010). The legend shows "unit cell design/orientation" and "relative density". Relative density values are either from CAD design values or measured values. All lattice specimens are Ti-6Al-4V made with EB-PBF and are in as-built condition.

Figure 4.18
Elastic Modulus vs Relative Density for Literature and Experiment

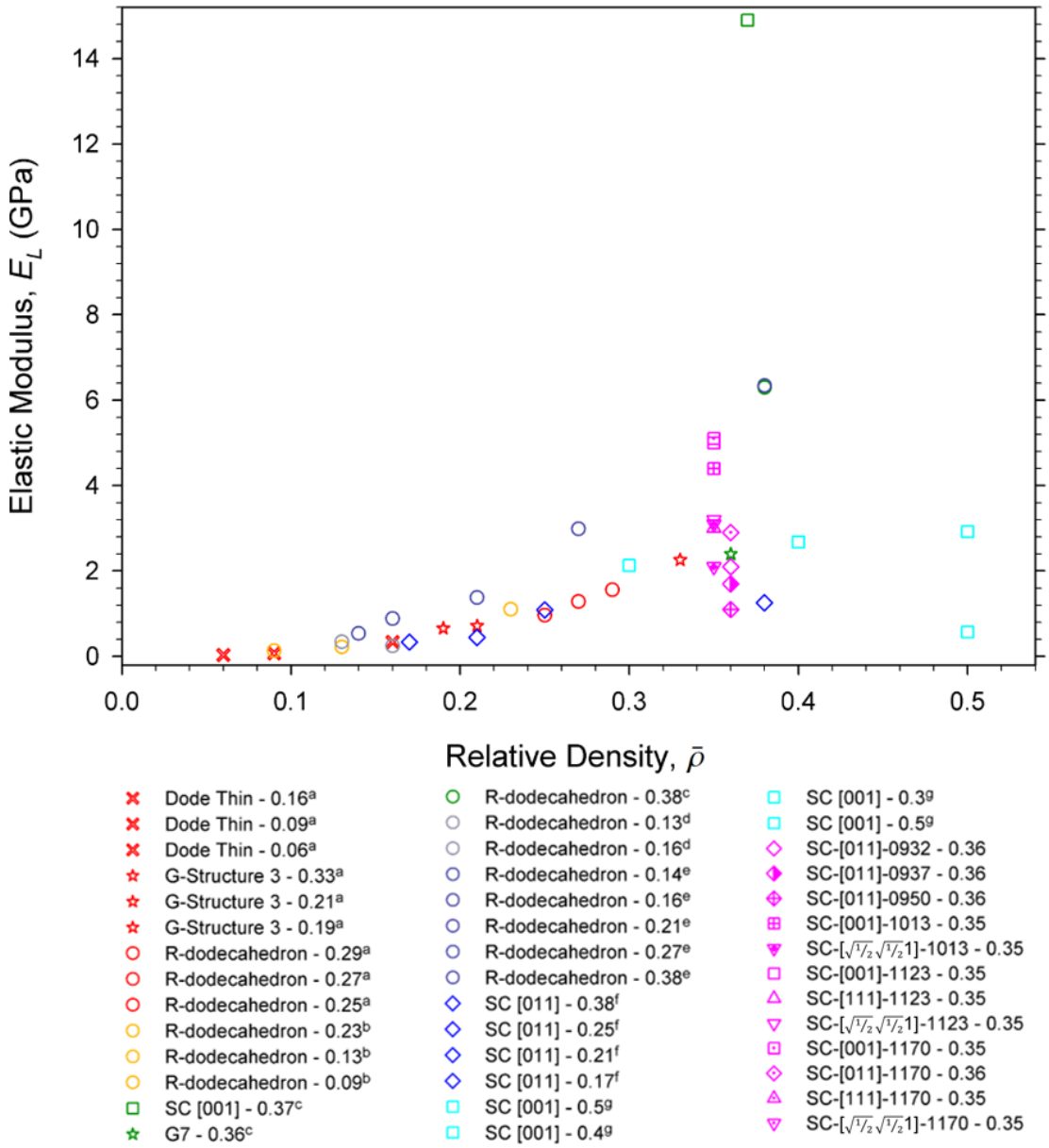

Note. Elastic modulus, E_L versus relative density, $\bar{\rho}$ graph based on the data in Table 4.3 and the studies of [a]Del Guercio et al. (2021a), [b]Epasto et al. (2019), [c]Zhao et al. (2016), [d]Xiao et al. (2015), [e]Cheng et al. (2012), [f]Li et al. (2012) and [g]Parthasarathy et al. (2010). The legend shows "unit cell design/orientation" and "relative density". Relative density values are either from CAD design values or measured values. All lattice specimens are Ti-6Al-4V made with EB-PBF and are in as-built condition.

One of the outliers is the SC [001] data point from the study by Parthasarathy et al. (2010). They reported having two specimens with the $\bar{\rho}$ of about 0.50, each with a large and small strut thickness or diameter, d_s of 0.94 mm and 0.47 mm, respectively. They attributed the difference of about 94 % in $\sigma_{UCS\text{-}L}$ to the strut thickness difference, even though the relative density remains relatively the same. Another outlier data point from the literature is an SC [001] by Zhao et al. (2016). They reported that the strut thickness for the [001] specimen is about 0.61 mm. There

were no additional discussions about its $\sigma_{UCS\text{-}L}$.

For the experimental data from this study, the outliers from the general trend are all the specimens with [001] orientation and the specimens with [011] orientation from batches 0937 and 0950. The other specimens seem to be relatively close to the general trend when considering an increase in the $\sigma_{UCS\text{-}L}$ spread of about 20 MPa from the centre of the trend at higher $\bar{\rho}$ of above 0.35.

Unit cell designs and deformation modes effect. Examining the unit cell designs of the data in Figure 4.17, the SC [001] is the only unit cell that has vertical struts which are parallel to the loading direction (LD) that will be load-bearing during compressive loading and has a buckling dominant deformation mode. The deformation mode would make the SC [001] as a stretching-dominated deformation lattice. This means that the $\sigma_{UCS\text{-}L}$ of the SC [001] specimen lattice is expected to be significantly higher than the other unit cell designs with load-bearing struts that are not parallel to the loading direction and will be in bending dominant deformation mode, as found in Section 4.1.4. Therefore, the data points from the SC [001] specimen by Zhao et al. (2016) and the [001] specimens from 1013, 1123 and 1170 batches are expected to be significantly higher than the general trend from bending deformation mode specimens. However, this does not explain the SC [001] specimen by Parthasarathy et al. (2010), which has three data points that agree with the general trend. This will be explained in the following.

Build direction effect on SC [001] **lattice**. Looking into the SC [001] lattice specimens from both the study of Zhao et al. (2016) and Parthasarathy et al. (2010), there is a difference in the build direction relative to the loading direct and unit cell orientation observed. The SC [001] lattice specimen by Zhao et al. (2016) is shown to be parallel to the loading direction and unit cell orientation as observed in Figure 4.19(a), which is similar to the [001] specimens from 1013 (Figure 4.19(c)), 1123 and 1170 batches. On the other hand, the SC [001] lattice specimen by Parthasarathy et al. (2010) shows a build direction that is at an angle of about 45° relative to the unit cell orientation and loading direction. This means the vertical load-bearing struts have overlapping melts of 45° to the loading direction instead of overlapping melts perpendicular to the loading direction. This difference in the build direction most likely resulted in a bending dominant deformation mode during compressive loading and may explain the significantly lower $\sigma_{UCS\text{-}L}$ than the other SC [001] specimens and the three data points that agree with the general trend.

Figure 4.19
Comparison of Build Direction for SC [001] *Lattice in Literature and Experiment*

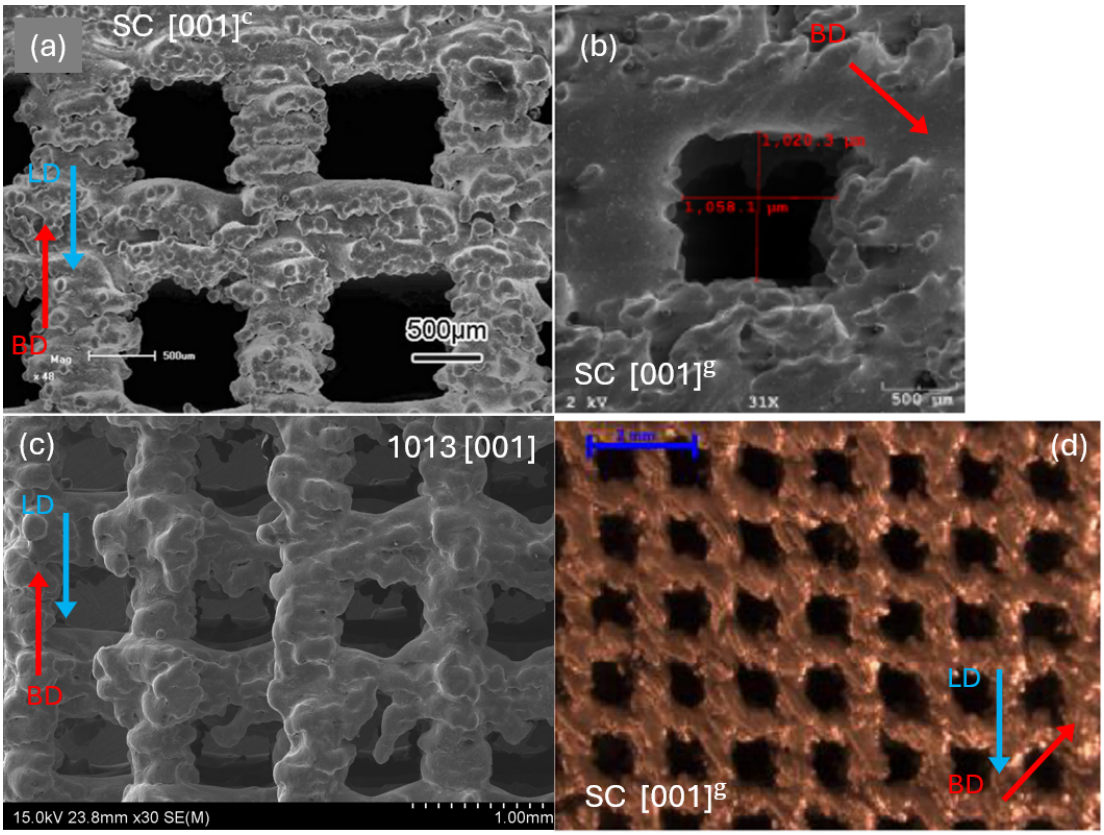

Note. Build direction comparison for the SC [001] lattice. The build direction, unit cell orientation and loading direction are parallel for the specimen by (a) [c]Zhao et al. (2016) and (c) the [001] specimen from batch 1013. The SC [001] lattice by [g]Parthasarathy et al. (2010) in (b) and (d) have the build direction at an angle of about 45° relative to the unit cell orientation and loading direction.

Batch variation effect on 0937 and 0950. As discussed previously in Section 4.1.5, the lattice specimens from batches 0950 and 0937 were found to be significantly weaker than the other two batches of 0932 and 1013 due to their smaller $d_{s\text{-}e}$ that is attributed to the batch variation effect. Therefore, the lattice specimens from batches 0950 and 0937 having significantly lower $\sigma_{UCS\text{-}L}$ and E_L for a $\bar{\rho}$ of about 0.355 than the general trend can also be attributed to the same factor of smaller $d_{s\text{-}e}$ due to batch variation, as the batches 0932 and 1013 specimens are closer to the general trend. In addition, the specimen batches with the net theme A most likely have a lower $\bar{\rho}$ than the designed $\bar{\rho}$ value of about 0.355 since the estimated $d_{s\text{-}e}$ measured for 0950 and 0937 batches have a median value of 367 µm and 404 µm respectively, which is significantly lower than the d_s design value of 500 µm. This is further supported by the observation that the specimens from batches 1123 and 1170, which were made using net theme B and have thicker $d_{s\text{-}e}$, have $\sigma_{UCS\text{-}L}$ and E_L values that are comparable with the general trend. Their thicker $d_{s\text{-}e}$ would suggest that their $\bar{\rho}$ is closer or slightly higher than the design $\bar{\rho}$ of about 0.355.

4.2 Orientation and Batch Variation Effect on Fatigue Strength of Simple Cubic Ti-6Al-4V Lattice

4.2.1 Compression-Compression Fatigue Experiment Data

Fatigue tests on the Ti-6Al-4V lattice specimen were carried out with a constant amplitude fatigue loading of compression-compression mode and with a stress ratio R of 0.1. The compressive fatigue experiment data of cycles to failure with the corresponding maximum stress for specimen orientation and batch are tabulated in Table 4.7. There are four batches of specimens tested, namely batch 0932, 0937, 0950 and 1013, and two types of unit cell orientation, [011] and [$\sqrt{1/2}$ $\sqrt{1/2}$1]. Only two specimens were tested for batch 0937 due to the limited number of specimens, most of which were tested in the quasi-static compressive experiment. The compressive fatigue experiment data is also presented graphically in Figure 4.20 and Figure 4.21, with regression lines for the batches 0932, 0950 and 1013, excluding specimens with run-out cycles. Table 4.8 shows the fatigue strength data based on the regression lines in Figure 4.21 for the intervals of cycles to failure.

Batch 1013 shows the highest fatigue strength at the low fatigue cycles (LCF) of below 10^4 cycles, followed by batches 0932 and batch 0950 being the lowest (Figure 4.20). Looking at the regression line for the fatigue strength data points in Figure 4.21, the fatigue strength at LCF for batch 0932 and 1013 is quite close, and batch 0950 is significantly lower. Batch 0937, with two specimen data points, shows an estimated fatigue strength range close to batches 0932 and 1013.

At the higher fatigue cycle range of 10^5 to 10^6 cycles, the fatigue strength difference between the batches decreases significantly, with about 4 MPa to 5 MPa of fatigue strength difference at 10^5 cycles for batch 1013 and 0932 versus batch 0950 and about 0.6 MPa to 1.1 MPa difference at 10^6 cycles (Table 4.8). The fatigue strength of all specimen batches shows a trend that converges at about 10.5 MPa of maximum stress when passing the 10^6 cycles range.

The compressive fatigue experiment data analysis findings can be summarised below.

1. Batch 1013 has the highest fatigue strength, followed by 0932 and 0950.
2. The difference in fatigue strength is more significant at the LCF region and becomes much smaller when passing 10^5 cycles.
3. The fatigue strengths of all batches 1013, 0932 and 0950 converge at about 10.5 MPa after passing 10^6 cycles.

Table 4.7
Cycles to Failure Data for Compression-Compression Fatigue Test

Orientation	Batch	Max Force, F_{max} (N)	Max Stress, σ_{max} (MPa)	Cycles to Failure, N_f
[011]	0932	2 222	28.29	5 965
		1 777	22.63	19 519
		1 421	18.09	66 257
		1 137	14.48	87 732
		910	11.59	1 048 369
		728	9.27	1 245 153*
[011]	0937	1 777	22.63	9 113
		1 421	18.09	134 162
[011]	0950	2 220	28.27	118
		1 421	18.09	1 157
		1 421	18.09	11 679
		1 300	16.55	3 335
		1 300	16.55	19 861
		1 150	14.64	6 490
		1 150	14.64	28 664
		1 000	12.73	64 750
[$\sqrt{1/2}$ $\sqrt{1/2}$1]	1013	4 320	55.00	433
		2 749	35.00	6 826
		2 200	28.01	8 374
		2 200	28.01	18 020
		1 900	24.19	18 008
		1 900	24.19	27 906
		1 600	20.37	56 280
		1 600	20.37	37 400
		1 300	16.55	113 856
		1 300	16.55	133 196
		1 000	12.73	298 760
		1 000	12.73	495 504
		700	8.91	1 920 543*
		700	8.91	1 525 607*
		700	8.91	5 925 442*

Note. Fatigue test data for simple cubic Ti-6Al-4V lattice with stress ratio $R = 0.1$ and compression-compression loading mode. *Cycles run-out.

Table 4.8
Fatigue Strength at N Cycles

		Fatigue Strength at N Cycles, σ_N (MPa)			
Orientation	Batch	σ_{10^3}	σ_{10^4}	σ_{10^5}	σ_{10^6}
[011]	0932	37.2	24.8	16.5	11.0
[011]	0950	20.4	16.0	12.6	9.9
[$\sqrt{1/2}$ $\sqrt{1/2}$1]	1013	47.8	28.9	17.5	10.5

Note. Fatigue strength at cycle intervals based on regression lines in Figure 4.21 for batch 0932, 0950 and 1013.

Figure 4.20
Maximum Stress vs Cycles to Failure Graph

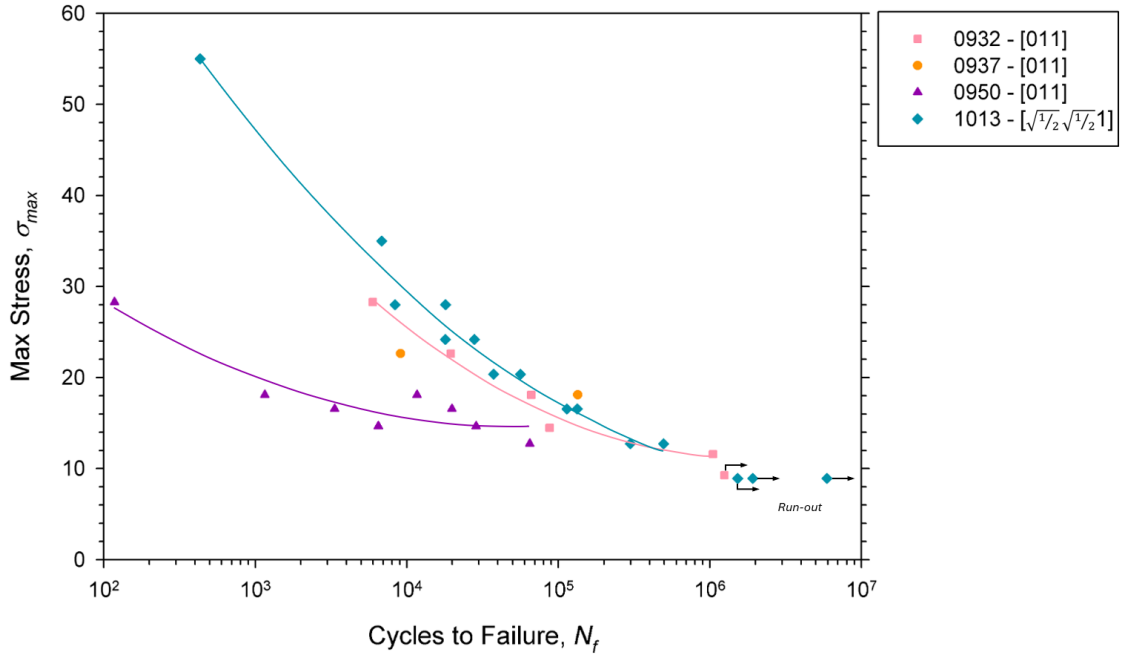

Note. Maximum compressive stress versus cycles to failure graph from the data in Table 4.7. Specimen batch and unit cell orientation are shown in legend. The stress ratio is $R = 0.1$, and the loading mode is compression-compression.

Figure 4.21
Maximum Stress (log) vs Cycles to Failure Graph

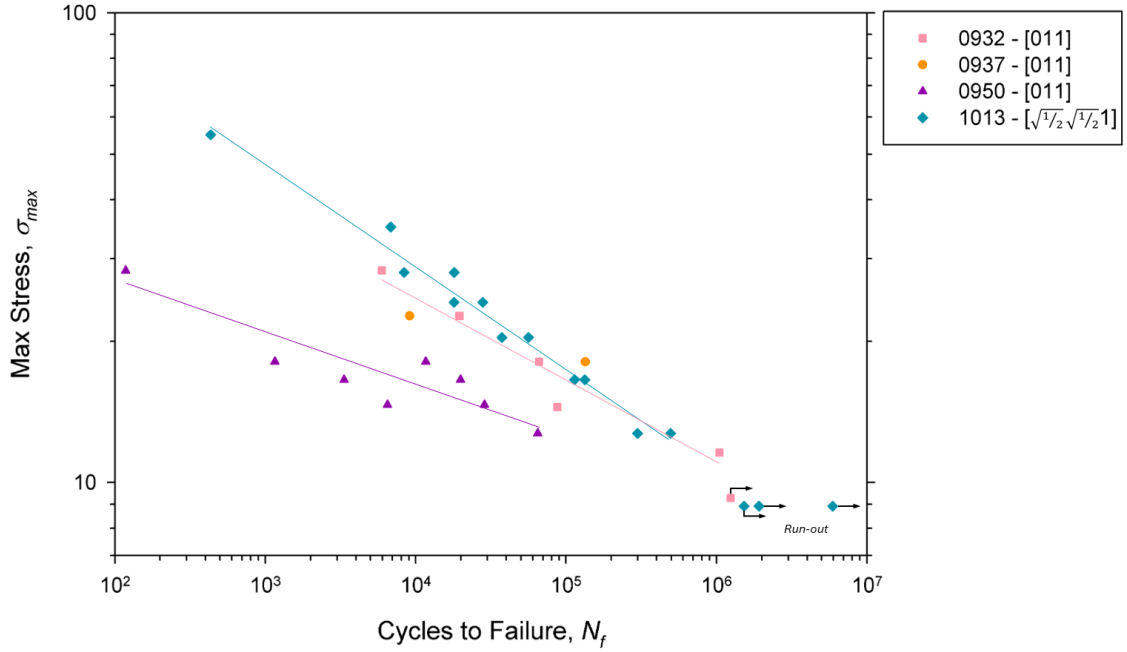

Note. Maximum compressive stress (log) versus cycles to failure graph from the data in Table 4.7. Specimen batch and unit cell orientation are shown in legend. The stress ratio is $R = 0.1$, and the loading mode is compression-compression.

4.2.2 Strut Fatigue Fracture Data

The tested specimens in the compressive fatigue experiment were inspected using SEM after testing to examine the fatigue fracture characteristics for different cycles to failure. Specimens from the 1013 batch were selected with cycles to failure of 433 cycles, 18,008 cycles and 1,920,543 cycles (run-out).

The SEM images of the strut fracture for 1013 [$\sqrt{1/2}\,\sqrt{1/2}1$] specimen with σ_{max} of 55 MPa and N_f of 433 cycles are shown in Figure 4.22. This specimen is considered to be at the very low range of the LCF range. The arrow in Figure 4.22(a) shows the notch or melt imperfection that acted as the site for crack initiation. Fracture is only visible after moving upwards from the arrow, as observable in Figure 4.22(b). The fatigue fracture is quite jagged, with the crack growth going in a few directions at several points and growing into a few fractures, as seen in Figure 4.22(c).

Figure 4.23 and Figure 4.24 show the SEM images of the strut fracture for 1013 [$\sqrt{1/2}\,\sqrt{1/2}1$] specimen with σ_{max} of 24.2 MPa and N_f of 18,008 cycles. This specimen is considered to be at the end of the LCF range (10^4 cycles). The arrow in Figure 4.23(a) and Figure 4.24(a) shows the notch that acted as the site for crack initiation. The observed fatigue fracture is jagged, but the crack growth only created one continuous fracture.

The SEM images in Figure 4.25 show the strut fracture for the 1013 [$\sqrt{1/2}\,\sqrt{1/2}1$] specimen with σ_{max} of 8.9 MPa and N_f of 1,920,542 cycles, which was a run-out specimen and did not meet the failure criteria when the fatigue test was stopped. This specimen is in the HCF range of past 10^6 cycles. The arrow in Figure 4.25(a) shows the notch or melt imperfection, which acted as the crack initiation site. The fatigue fracture observed in Figure 4.25(b) and (c) shows a smooth fracture that follows the general direction of the melt imperfection shape. Looking closer at the fatigue fracture in Figure 4.25(d), striation marks following the crack growth are visible. The findings of the fatigue fracture examination by SEM analysis can be summarised below.

1. The strut fatigue fracture of the LCF specimens with N_f of 433 cycles and 18,8008 cycles are quite jagged and have multiple fractures.

2. The strut fatigue fracture of the HCF specimen with N_f of 1,920,542 cycles is smoother, with striation marks visible and the crack growth following the general shape of the melt imperfection.

3. All strut fatigue fractures observed seem to have initiated at the notch or melt imperfections of the strut.

Figure 4.22
Fatigue Fracture for Low Cycle Fatigue Specimen

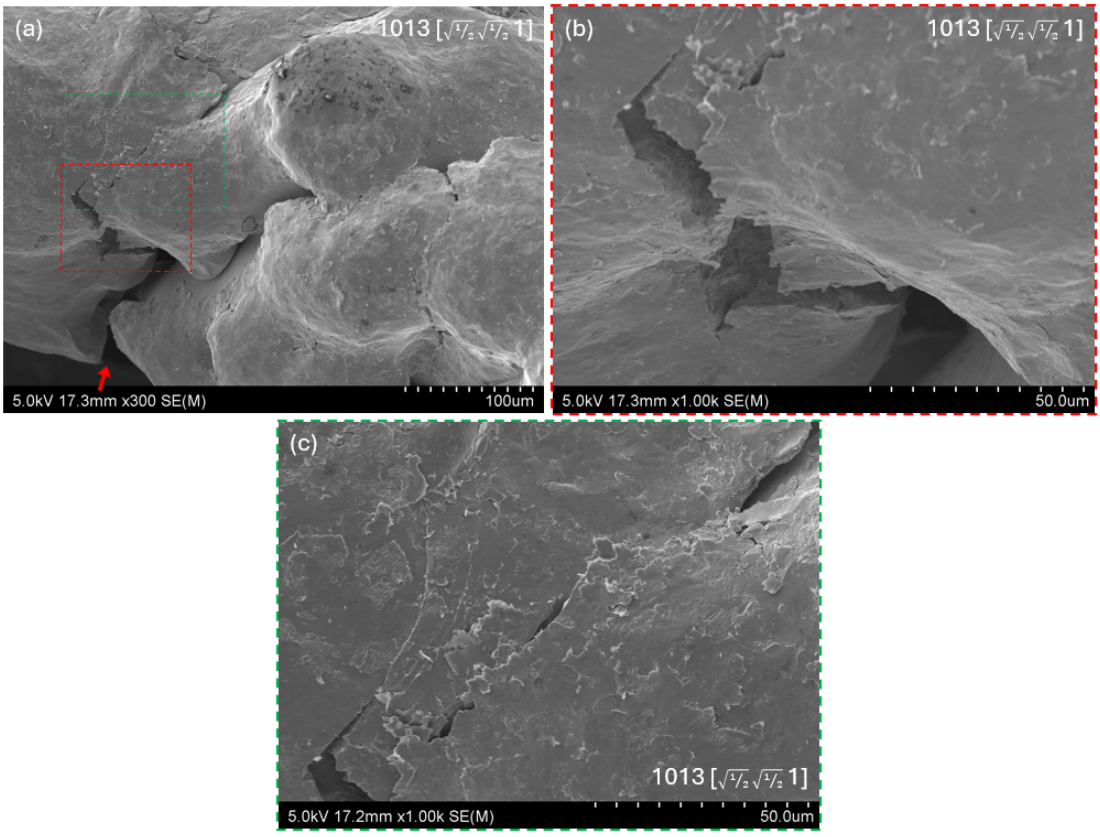

Note. SEM images of fatigue fracture for LCF specimen 1013 [$\sqrt{1/2}\,\sqrt{1/2}1$] with σ_{max} of 55 MPa and N_f of 433 cycles. Fracture initiated from melt imperfection or notch on the strut.

Figure 4.23
Fatigue Fracture for Low Cycle Fatigue Specimen

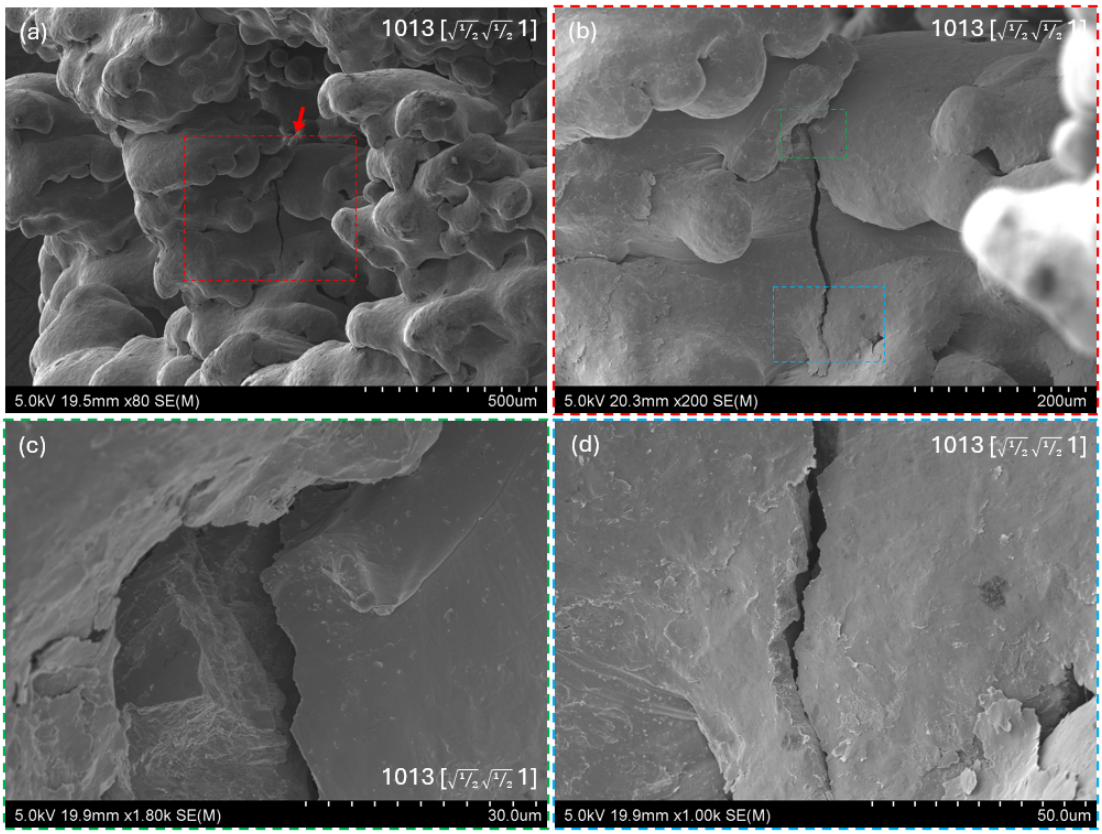

Note. SEM images of fatigue fracture for LCF specimen 1013 [$\sqrt{1/2}\ \sqrt{1/2}1$] with σ_{max} of 24.2 MPa and N_f of 18,008 cycles. Fracture initiated from melt imperfection or notch on the strut.

Figure 4.24
Fatigue Fracture for Low Cycle Fatigue Specimen

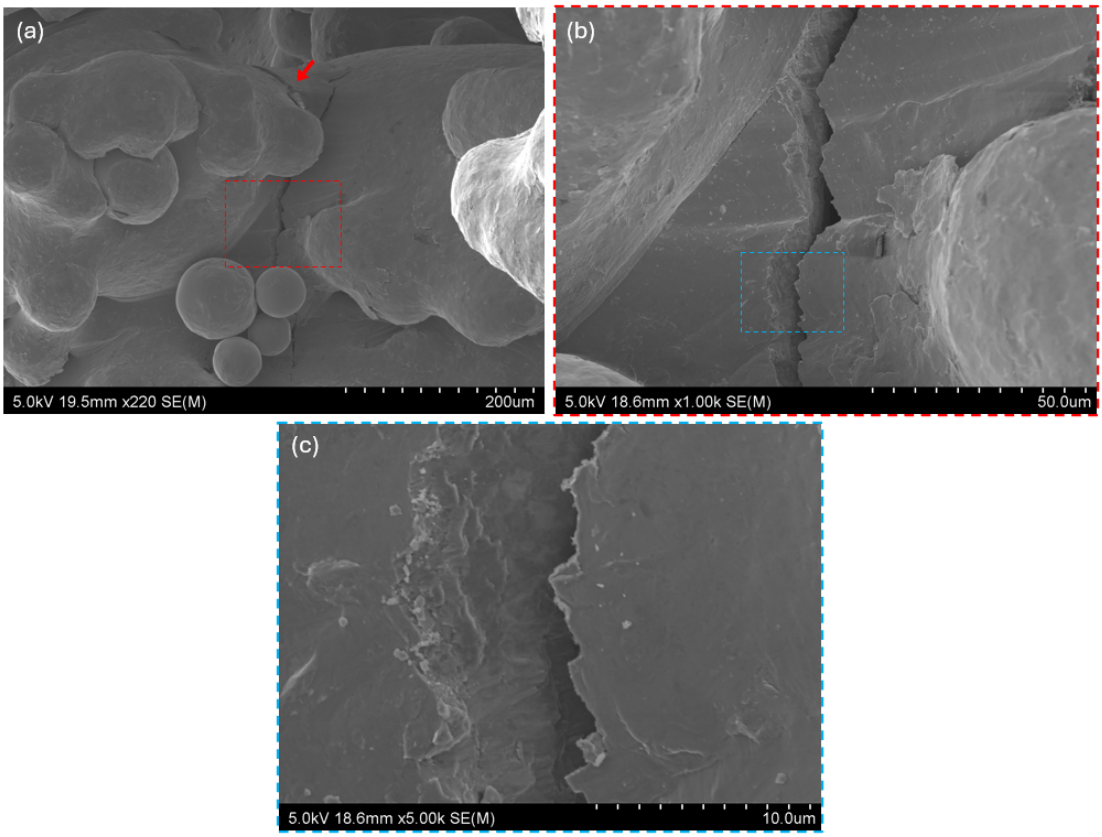

Note. SEM images of fatigue fracture for LCF specimen 1013 [$\sqrt{1/2}\ \sqrt{1/2}1$] with σ_{max} of 24.2 MPa and N_f of 18,008 cycles. Fracture initiated from melt imperfection or notch on the strut.

Figure 4.25
Fatigue Fracture for High Cycle Fatigue Specimen

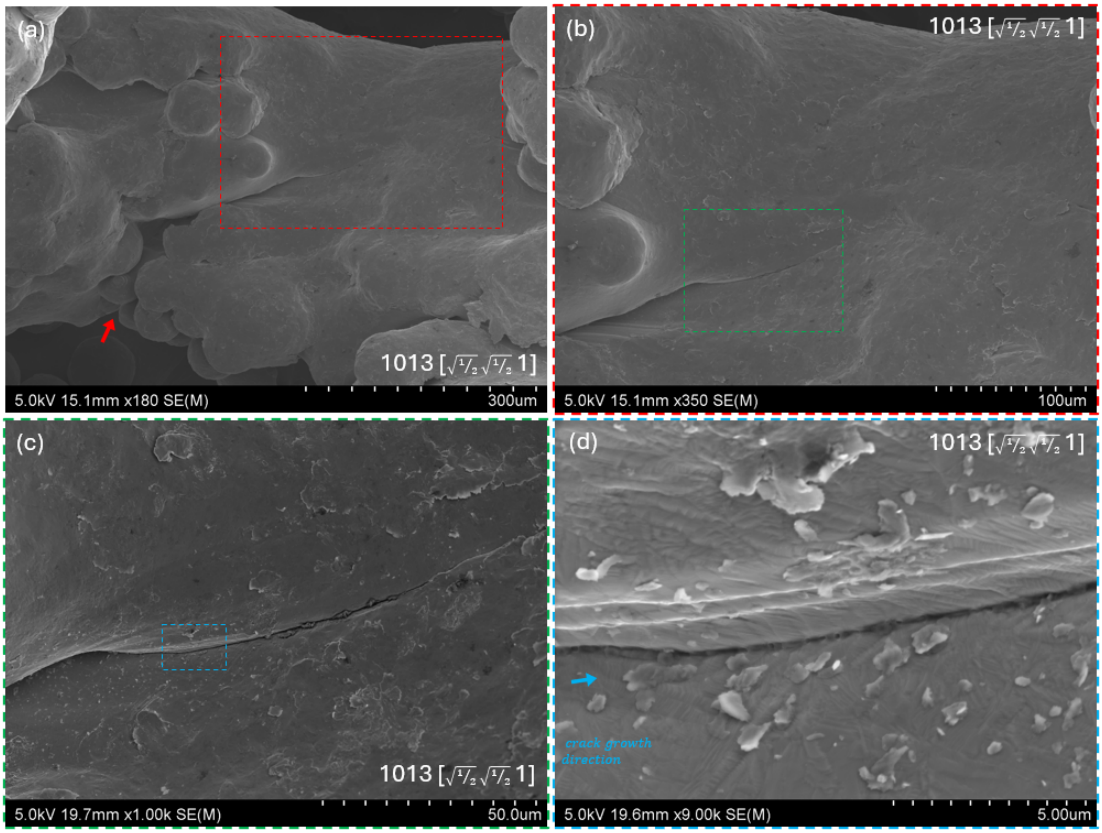

Note. SEM images of fatigue fracture for HCF specimen with σ_{max} of 8.9 MPa and N_f of 1,920,543 cycles (run-out). Fracture initiated from melt imperfection or notch on the strut. (d) Striation marks can be observed at fracture. (a) The crack initiated and grew in a direction that roughly followed the melt imperfection or notch.

4.2.3 Orientation Effect on Fatigue Strength Analysis

The compression-compression fatigue test on the simple cubic Ti-6Al-4V lattice structure made with EB-PBF has been carried out in this study, and the results are presented in Section 4.2.1. The strut fatigue fracture data inspected using SEM is given in Section 4.2.2. This section will discuss the findings and analysis based on the unit cell orientation effect. This study was only able to examine the orientation effect on the compressive fatigue strength experimentally for two orientations of [011] and [$\sqrt{1/2}$ $\sqrt{1/2}$1] of the Ti-6Al-4V simple cubic lattice due to limited specimen availability.

The orientation [011] **has a comparable fatigue strength with** [$\sqrt{1/2}$ $\sqrt{1/2}$1]. The lattice specimen from batch 1013 has the highest fatigue strength, followed by 0932 and 0950 (Fatigue 4.21). Similar to the trend observed in the quasi-static compressive experiment results, the fatigue strength data also showed a comparable value for the specimens with orientation [011] and [$\sqrt{1/2}$ $\sqrt{1/2}$1] for the batch of 1013 and 0932, while the [011] orientation specimen of the 0950 batch has a significantly lower value. Therefore, the fatigue strengths can be assumed to follow the compressive strength of the lattice specimen, where a higher compressive strength will result in higher fatigue strength and also follow the compressive strength from the unit cell orientation effect, based on the [011] 0932 and [$\sqrt{1/2}$ $\sqrt{1/2}$1] 1013 specimens. The significantly lower fatigue strength of the 0950 batch specimens is also attributed to their lower compressive strength due to the batch variation effect and not the unit cell orientation effect.

Unit cell orientation effect on fatigue strength overall findings. Based on the analysis and discussion above, the unit cell orientation of [011] and [$\sqrt{1/2}$ $\sqrt{1/2}$1] does affect the fatigue strength of simple cubic Ti-6Al-4V lattice structure made with EB-PBF under cyclic compression-compression loading. The fatigue strength generally follows the compressive strength of the lattice structure. Even though there is no lattice specimen with [001] orientation tested in the experiment, Section 4.2.5 examined the available fatigue strength data from the literature for simple cubic Ti-6Al-4V lattices with [001] orientation. The [001] orientation fatigue strength data was significantly higher than simple cubic lattices with other orientations. It agrees with the experiment's finding that the fatigue strength of the simple cubic lattice follows the trend of their compressive strength.

4.2.4 Batch Variation Effect on Fatigue Strength Analysis

The compression-compression fatigue test on the simple cubic Ti-6Al-4V lattice structure made with EB-PBF has been carried out in this study, and the results are presented in Section 4.2.1. The

strut fatigue fracture data inspected using SEM is given in Section 4.2.2. This section will discuss the findings and analysis based on the batch variation effect. This study could only examine the batch variation effect on the compressive fatigue strength experimentally for four batches (with one batch only having two specimens) of the Ti-6Al-4V simple cubic lattice due to limited specimen availability.

Fatigue strength of 1013 and 0932 is higher than 0950. The fatigue strength of the specimen from batches 1013 and 0932 is significantly higher than that of batch 0950, which follows the trend observed in their compressive strength under quasi-static compression load. This suggests that the fatigue strength is proportional to the compressive strength of the specimen and that factors such as the batch variation effect that affected the compressive strength also influence the fatigue strength. Therefore, the significantly weaker fatigue strength of the 0950 specimen batch is attributed to the batch variation effect that caused their $d_{s\text{-}e}$ to be considerably smaller than the other batch specimen with the same net theme A. The fatigue strength of the 0937 batch, with only two specimen data points, also seems to follow the compressive strength data trend of being slightly higher than the 0950 batch but lower than the 1013 and 0932 batches when looking at the specimen with cycles to failure of about 10^4.

Fatigue strength difference between batches becomes less apparent at the HCF region. The difference in fatigue strength is more significant at the LCF region and becomes much smaller when passing 10^5 cycles. The fatigue strengths of all batches 1013, 0932 and 0950 converge at about 10.5 MPa after passing 10^6 cycles (Figure 4.20). This is against the expectation that the lattice specimen from the 1013 batch, that have a much higher fatigue strength at the LCF region, should also have a higher fatigue strength in the HCF region when compared to the 0950 batch.

This indicates that the lattice structure print quality and the difference in the $d_{s\text{-}e}$ between the specimen batches may not influence the fatigue strength as significantly at higher cycles region and lower maximum stress when compared to lower cycles region and high maximum stress. However, this observation may only be applicable with bending-dominated deformation lattice structures such as the [011] and [$\sqrt{1/2}$ $\sqrt{1/2}$1] orientation in this study.

This may suggest that the difference in the print quality for surface roughness and the presence of notches as a stress concentrator becomes less significant at lower maximum stress cyclic loading during the fatigue test as all the specimens are as-built and have a minimum level of strut surface roughness. Thus, the number of loading cycles spent for the crack initiation or stage I phase, as described by Benedetti et al. (2021), would be comparable between the batches. The number of loading cycles spent in the stage II phase of crack propagation, which is the majority of the total

fatigue cycles before going into stage III, does not increase significantly as the maximum stress of the cyclic load is lowered, negating the effect of the difference in $d_{s\text{-}e}$ between batches.

The strut fatigue fracture may explain the lack of effect from the difference in $d_{s\text{-}e}$ between batches in the fatigue strength. All strut fatigue fractures inspected using the SEM seem to have initiated at a notch or melt imperfections of the strut, as expected (Section 4.2.2. The fatigue fracture of the LCF specimens with N_f of 433 cycles and 18,808 cycles are jagged and have multiple fractures, with the crack growth direction relatively going across the strut thickness (Figure 4.22). On the other hand, the fatigue fracture of the HCF specimen with N_f of 1,920,542 cycles (run-out) is smoother, with striation marks visible and the crack growth following the general shape of the melt imperfection (Figure 4.25). The difference in the crack growth direction may cause a difference in the failure mechanism of the lattice specimen during the fatigue test, where the higher stress maximum applied would fail due to total strut fracture and the lower stress maximum applied would fail due to the overall weakening of the lattice specimen as the crack propagation reduces the remaining supporting strut thickness. As the crack propagation at the lower stress maximum does not necessarily go across the strut thickness and may follow the shape of the notch or melt imperfection, the difference in $d_{s\text{-}e}$ between batches will not be a significant factor.

Batch variation effect on fatigue strength overall findings. Based on the analysis and discussion above, it is clear that the batch variation factor does affect the fatigue strength of the simple cubic Ti-6Al-4V lattice structure with bending-dominated deformation made with EB-PBF under compression-compression loading. The fatigue strength generally follows the compressive strength of the lattice structure with the effect of the batch variation factor, but only in LCF regions. The fatigue strength of all the specimen batches seems to converge at 10.5 MPa past 10^6 cycles to failure.

4.2.5 Fatigue Strength of EB-PBF and L-PBF Strut-based Ti-6Al-4V Lattice

A comparison between experimental data from this study and the data from the literature for compression-compression fatigue strength of EB-PBF and L-PBF strut-based Ti-6Al-4V lattice is done in this section. To make the literature and experimental data comparable, the compressive fatigue strength data of the lattice specimens were normalised with the ultimate compressive strength, $\sigma_{UCS\text{-}L}$ of its lattice specimen. Since the same factors that affect the $\sigma_{UCS\text{-}L}$ also affect the compressive fatigue strength, σ_N of the lattice, then normalising the σ_N the $\sigma_{UCS\text{-}L}$ will take into account the effects from relative density, unit cell design, effective strut thickness, loading and build direction and post-print heat treatment. The normalised σ_N will be expressed as a fraction

of its $\sigma_{UCS\text{-}L}$ as shown in Figure 4.26 and with a log scale in Figure 4.27.

Figure 4.26
Normalised Fatigue Strength with UCS vs Cycles to Failure Graph

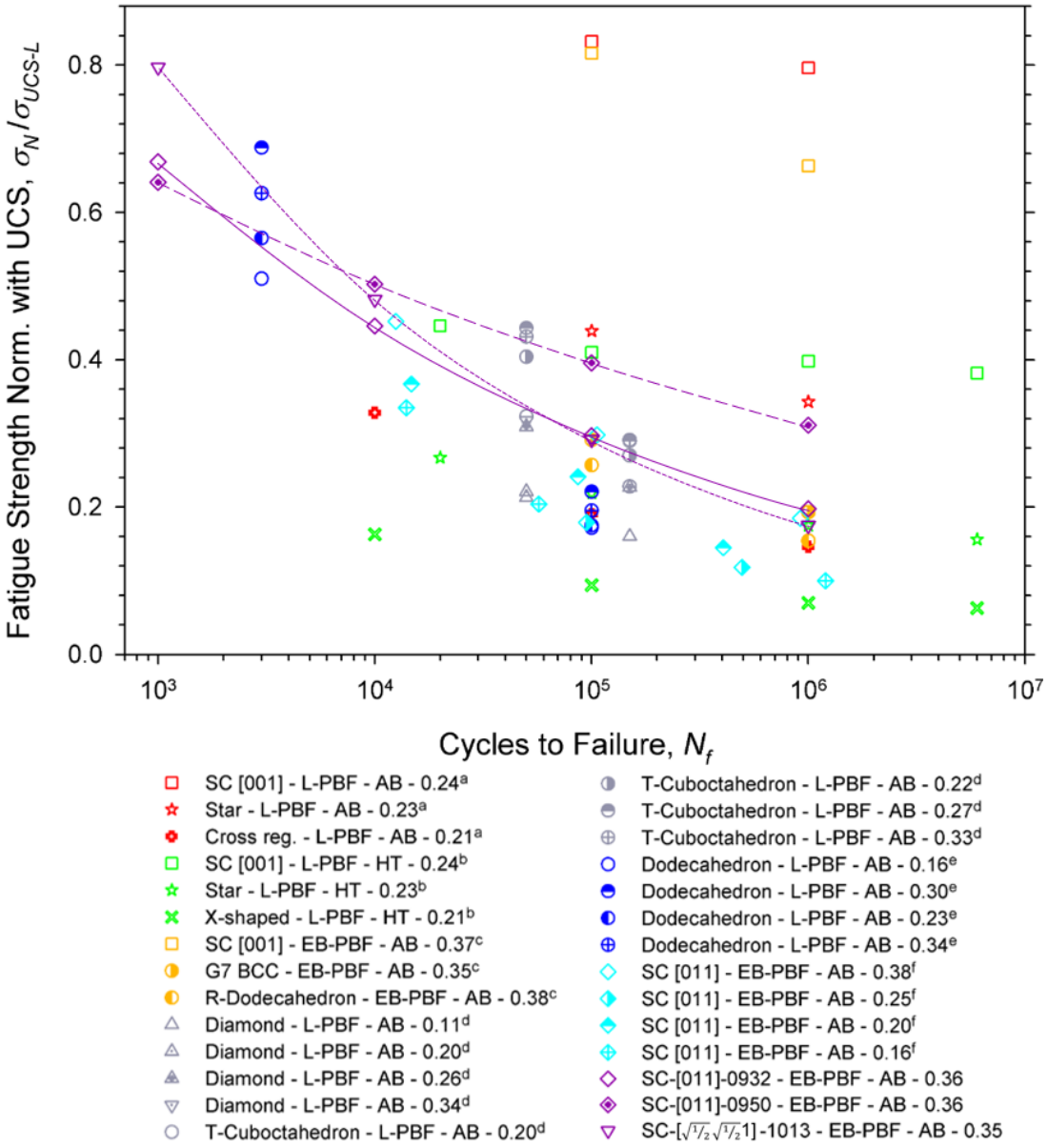

Note. Fatigue strength normalised with ultimate compressive strength $\sigma_{UCS\text{-}L}$ versus cycles to failure graph based on the data in Table 4.8 and the studies of [a]Raghavendra et al. (2021), [b]Raghavendra et al. (2020), [c]Zhao et al. (2016), [d]Amin Yavari et al. (2015), [e]Amin Yavari et al. (2013) and [f]Li et al. (2012). The legend shows "unit cell design/orientation - powder bed fusion type - post-print processing - relative density". All lattice specimens are made with Ti-6Al-4V.

The data from the literature are for Ti-6Al-4V lattice specimens with strut-based unit cell designs made with both powder bed fusion of EB-PBF and L-PBF. Some of the lattice specimens from the literature used the simple cubic unit cell design with [001] and [011] orientation. Experimentally, only SC lattice specimens with the [011] and [$\sqrt{1/2}$ $\sqrt{1/2}$1] orientations were tested. Some of the L-PBF specimens have post-print heat treatment (HT), and the rest are in as-built (AB) con-

ditions without any post-print treatment. The relative densities of $\bar{\rho}$ indicated in the legends are either the designed CAD or the measured value. The $\bar{\rho}$ of the specimens from the literature ranges from 0.11 to 0.38.

Examining the Figure 4.26, the normalised σ_N experimental data shows the weakest specimens of 0950 batch to be comparable or better than the other two batches of 0932 and 1013 at N_f of 10^4 and above. The specimens of the 0950 batch were able to withstand about 30 % of its $\sigma_{UCS\text{-}L}$ as the max fatigue stress up to 10^6 cycles, whereas the specimens in batches 0932 and 1013 can withstand about 20 % of its $\sigma_{UCS\text{-}L}$ to the same number of cycles. Most of the data points from the literature are in the same normalised σ_N range for the cycles of failure.

It can be observed that the σ_N for the N_f range of 10^4 to 10^6 are less than half of the value of their $\sigma_{UCS\text{-}L}$, except for SC [001] lattice specimens from the study by Raghavendra et al. (2021) and Zhao et al. (2016), which are above 0.65 of normalised σ_N. The specimens by Raghavendra et al. (2021) were made with L-PBF, and the specimens by Zhao et al. (2016) were made with EB-PBF. Both studies were tested with their specimens in AB condition. The other lattice specimens with their normalised σ_N value above 0.5 are only when the N_f are less than 10^4 and closer to 10^3, which are the specimens with dodecahedron unit cell design from Amin Yavari et al. (2013).

Unit cell designs and deformation modes effect. The lattice specimens in Figure 4.26 have unit cell designs that are generally known to have bending-dominated deformation when under compressive loading, except for the lattice specimen of SC [001], which have a stretching-dominated deformation. The normalised σ_N values of the literature specimens, except the SC [001], show a general trend that follows the experimental data of SC [011]-0950, SC [011]-0932 and SC [$\sqrt{1/2}$ $\sqrt{1/2}$1]-1013, which are bending-dominated deformation lattices. The SC [001] lattice specimen, except for the ones from Raghavendra et al. (2020), are significantly higher in their normalised σ_N values and have a grouping that is higher than the general trend.

The SC [011] lattice specimens by Li et al. (2012) have normalised σ_N values that are slighlty lower than the SC [$\sqrt{1/2}$ $\sqrt{1/2}$1]-1013 and SC [011]-0932 specimens, except for the SC [011] specimens with $\bar{\rho}$ of 0.38, which have comparable normalised σ_N values. The lower $\bar{\rho}$ values of 0.16 to 0.25 of the other SC [011] lattice specimens by Li et al. (2012) might be the cause of the slightly lower normalised σ_N values when compared to the C [$\sqrt{1/2}$ $\sqrt{1/2}$1]-1013 and SC [011]-0932 specimens with $\bar{\rho}$ of about 0.35. The other specimens with lower normalised σ_N values compared to the experimental data also seem to have lower $\bar{\rho}$ values below 0.3. Among them is the x-shaped unit cell by Raghavendra et al. (2020) (although it might also be related to the heat treatment as discussed in the following), the dodecahedron unit cell by Amin Yavari et al. (2013) and the diamond

unit cell by Amin Yavari et al. (2015).

Therefore, the dominant deformation mode of the unit cell design does affect the normalised σ_N of the Ti-6Al-4V lattice made with PBF, which is also in agreement with the unit cell orientation effect that influences the dominant deformation mode of the simple cubic Ti-6Al-4V lattice made with EB-PBF, as observed and discussed in Section 4.2.3 and Section 4.1.4.

Unit cell orientation effect of SC [001]. Excluding the normalised σ_N data of the SC [001] lattice specimens by Raghavendra et al. (2020), the data from literature supports and is in agreement with the findings discussed in Section 4.2.3 and Section 4.1.4, which is that the σ_N of the simple cubic Ti-6Al-4V lattice follows the trend of its compressive strength under quasi-static loading, especially at LCF region. The data in Figure 4.26 shows that the SC [001] specimen from Raghavendra et al. (2021) and Zhao et al. (2016) has a significantly higher σ_N and the SC [011] and SC [$\sqrt{1/2}\,\sqrt{1/2}1$] specimens have lower σ_N. This trend of the σ_N is exactly the same as observed in the quasi-static compressive experiment and is attributed to the difference in the stretching-dominated deformation of the SC [001] specimens and the bending-dominated deformation of the SC [011] and SC [$\sqrt{1/2}\,\sqrt{1/2}1$] specimens.

The SC [001] lattice specimens by Raghavendra et al. (2021) and Raghavendra et al. (2020) were both made using L-PBF with about the same $\bar{\rho}$, but the specimens for the former were AB condition, and the latter undergone post-print heat treatment. The normalised σ_N values of the Raghavendra et al. (2020) heat treated SC [001] specimens are significantly lower than the AB SC [001] specimens of Raghavendra et al. (2021). It is not clear if the post-print heat treatment has the effect of reducing the fatigue strength of the SC [001] specimens from Raghavendra et al. (2020) as both the HT and AB SC [001] specimens were reported to have the same $\bar{\rho}$ and ultimate compressive strength of 125.6 MPa by the same author. Comparing the fatigue strength of another unit cell design by the same two studies, the star lattice specimens showed a similar significantly lower normalised σ_N of the HT specimen from Raghavendra et al. (2020) when compared to the similar AB star lattice specimen in Raghavendra et al. (2021), even though both specimens have the same $\bar{\rho}$. Thus, it can be assumed that the HT may have an effect that caused the difference in the normalised σ_N of the HT SC [001] specimens.

Therefore, it can be stated that the trend of the normalised σ_N of the simple cubic Ti-6Al-4V lattice made with PBF, based on the unit cell orientations, agrees with the same trend of compressive strength observed in the quasi-static compressive experiment.

Figure 4.27
Normalised Fatigue Strength with UCS (log) vs Cycles to Failure Graph

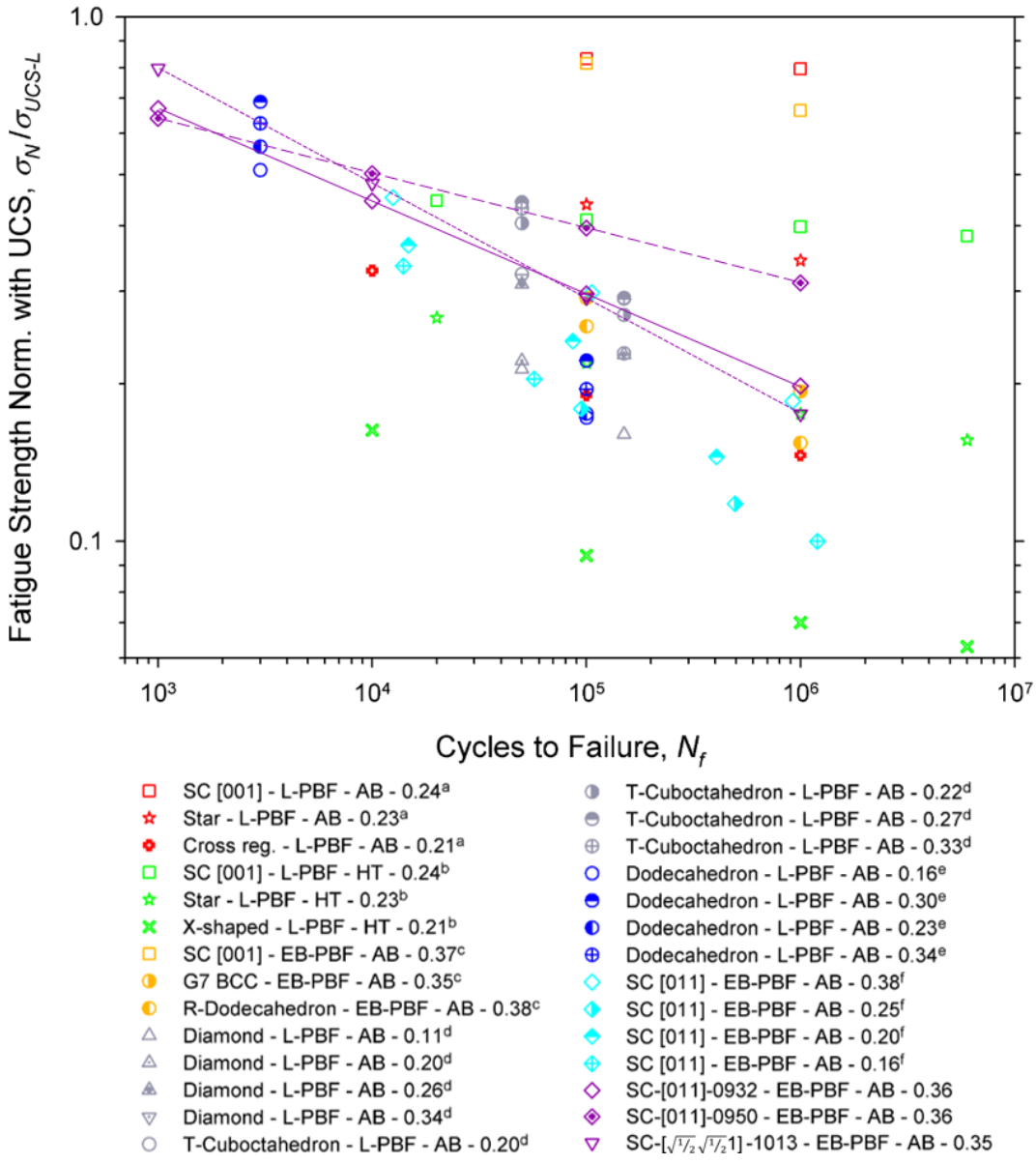

Note. Fatigue strength normalised with ultimate compressive strength $\sigma_{UCS\text{-}L}$ (log) versus cycles to failure graph based on the data in Table 4.8 and the studies of [a]Raghavendra et al. (2021), [b]Raghavendra et al. (2020), [c]Zhao et al. (2016), [d]Amin Yavari et al. (2015), [e]Amin Yavari et al. (2013) and [f]Li et al. (2012). The legend shows "unit cell design/orientation - powder bed fusion type - post-print processing - relative density". All lattice specimens are made with Ti-6Al-4V.

Chapter 5

Conclusion

This concluding chapter summarises the key research findings of this study relative to the research questions stated in the second chapter. Lastly, the lists of possible opportunities for future research based on the current findings are presented.

Main findings. This study aimed to examine the effect of unit cell orientation and batch variation on the mechanical strength of Ti-6Al-4V simple cubic lattice made with Electron Beam Powder Bed Fusion (EB-PBF) for quasi-static compressive and compression-compression fatigue loading. Four unit cell orientations of [001], [011], [111] and [$\sqrt{1/2}$ $\sqrt{1/2}$1] made from six batches of the simple cubic lattice were tested for in the quasi-static compressive test and two unit cell orientations of [011] and [$\sqrt{1/2}$ $\sqrt{1/2}$1] made from four batches of the simple cubic lattice were tested in the compression-compression fatigue test. The main findings of this thesis can be summarised below, where main findings 1 and 2 answer the first research question, and the main findings 3 and 4 answer the second research question.

1. The unit cell orientation does affect the mechanical behaviour of a simple cubic Ti-6Al-4V lattice structure made with EB-PBF under compressive load. The non-rotated simple cubic unit cell of [001] orientation still behaves with a stretching-dominated deformation, even with the small strut diameter and pore diameter that follows the osteoconductive requirement. The [001] orientation of stretching-dominated deformation is significantly stronger than the [011], [111] and [$\sqrt{1/2}$ $\sqrt{1/2}$1] orientations with bending-dominated deformation, which are in agreement with the quasi-static compressive simulation results. The [001] orientation has the highest compressive strength with $\sigma_{UCS\text{-}L}$ of 2.0 to 2.5 times higher, $\sigma_{y\text{-}L}$ of 1.8 to 2.1 times higher and E_L of 1.6 to 2.1 times higher than other orientations of [011], [111] and [$\sqrt{1/2}$ $\sqrt{1/2}$1].

2. The batch variation factor does affect the compressive strength behaviour of the simple cubic

Ti-6Al-4V lattice structure made with EB-PBF. The specimens that were printed using both of the net themes A and B showed that they had been affected by the batch variation of either increasing the spread of the $\sigma_{UCS\text{-}L}$, $\sigma_{y\text{-}L}$ and E_L values or decrease their mean values. The batch variation in net theme A were more significant in affecting the compressive strength of the printed lattice specimens.

3. The unit cell orientation of [011] and [$\sqrt{1/2}$ $\sqrt{1/2}$1] does affect the fatigue strength of simple cubic Ti-6Al-4V lattice structure made with EB-PBF under cyclic compression-compression loading. The fatigue strength generally follows the compressive strength of the lattice structure. Even though there is no lattice specimen with [001] orientation tested in the experiment, an examination of the available fatigue strength data from the literature for simple cubic Ti-6Al-4V lattices found that the [001] orientation fatigue strength data was significantly higher than simple cubic lattices with other orientations, which also agrees with the experiment's finding that the fatigue strength of the simple cubic lattice follows the trend of their compressive strength.

4. The batch variation factor does affect the fatigue strength of the simple cubic Ti-6Al-4V lattice structure with bending-dominated deformation made with EB-PBF under compression-compression loading. The fatigue strength generally follows the compressive strength of the lattice structure with the effect of the batch variation factor, but only in LCF regions. The fatigue strength of all the specimen batches seems to converge at 10.5 MPa past 10^6 cycles to failure.

5. The simple cubic lattice specimens with [001] orientation of batch 1123 and 1170 have the mechanical strength values that could be a good match for the biomedical bone implant, where the mean $\sigma_{UCS\text{-}L}$ for the lattice specimen is of about 235 MPa, which slightly exceeds the compressive strength of the cortical bone of 205 MPa, ensuring the ability to support the load. While the mean E_L for the lattice specimen is about 5 GPa, which is lower than the elastic modulus of the cortical bone of 17.9 GPa (longitudinal) and 10.1 (transverse) but higher than the elastic modulus of the trabecular bone of 0.44 GPa (femur), which would prevent the risk for stress shielding.

Recommendation for future work. The following are recommended for further investigation.

- The comparison of compressive strength for [001] simple cubic lattice from the literature and the experimental data in this study showed that a build direction that is not parallel to the

unit cell orientation and loading direction is lower than when they are all parallel. Further investigation should be done to clarify this and examine if a change in build direction for the other orientations, such as the [011] and [111], also changes its compressive strength as its dominant deformation mode is bending.

- The net theme A was found to have more batch variation of strut irregularities and effective strut diameter compared to net theme B. The differences in the net themes that cause net theme A to produce more batch variation in Ti-6Al-4V lattice specimens should be investigated.

References

Ahmadi, S. M., Hedayati, R., Li, Y., Lietaert, K., Tümer, N., Fatemi, A., Rans, C. D., Pouran, B., Weinans, H. H., & Zadpoor, A. A. (2018). Fatigue performance of additively manufactured meta-biomaterials: The effects of topology and material type. *Acta Biomaterialia*, *65*, 292–304. https://doi.org/10.1016/j.actbio.2017.11.014

Ahmadi, S. M., Yavari, S. A., Wauthle, R., Pouran, B., Schrooten, J., Weinans, H. H., & Zadpoor, A. A. (2015). Additively manufactured open-cell porous biomaterials made from six different space-filling unit cells: The mechanical and morphological properties. *Materials*, *8*(4), 1871–1896. https://doi.org/10.3390/ma8041871

Alabort, E., Barba, D., & Reed, R. C. (2019). Design of metallic bone by additive manufacturing. *Scripta Materialia*, *164*, 110–114. https://doi.org/10.1016/j.scriptamat.2019.01.022

Alamos, F. J., Schiltz, J., Kozlovsky, K., Attardo, R., Tomonto, C., Pelletiers, T., & Schmid, S. R. (2020). Effect of powder reuse on mechanical properties of Ti-6Al-4V produced through selective laser melting. *International Journal of Refractory Metals and Hard Materials*, *91*, 105273. https://doi.org/10.1016/j.ijrmhm.2020.105273

Al-Ketan, O., Rowshan, R., & Abu Al-Rub, R. K. (2018). Topology-mechanical property relationship of 3D printed strut, skeletal, and sheet based periodic metallic cellular materials. *Additive Manufacturing*, *19*, 167–183. https://doi.org/10.1016/j.addma.2017.12.006

Alomar, Z., & Concli, F. (2020). A review of the selective laser melting lattice structures and their numerical models. *Advanced Engineering Materials*, *22*(12), 1–17. https://doi.org/10.1002/adem.202000611

Amin Yavari, S., Ahmadi, S., Wauthle, R., Pouran, B., Schrooten, J., Weinans, H., & Zadpoor, A. (2015). Relationship between unit cell type and porosity and the fatigue behavior of selective laser melted meta-biomaterials. *Journal of the Mechanical Behavior of Biomedical Materials*, *43*, 91–100. https://doi.org/10.1016/j.jmbbm.2014.12.015

Amin Yavari, S., Wauthle, R., van der Stok, J., Riemslag, A., Janssen, M., Mulier, M., Kruth, J., Schrooten, J., Weinans, H., & Zadpoor, A. (2013). Fatigue behavior of porous biomaterials manufactured using selective laser melting. *Materials Science and Engineering: C*, *33*(8), 4849–4858. https://doi.org/10.1016/j.msec.2013.08.006

AP&C. (2024). Titanium alloy: Ti-6Al-4V grade 5. Retrieved March 23, 2024, from https://www.advancedpowders.com/powders/titanium/ti-6al-4v-5

ASTM International. (2014a). *Standard specification for additive manufacturing titanium-6 aluminum-4 vanadium ELI (extra low interstitial) with powder bed fusion (F3001-14)*. ASTM International. https://www.astm.org/Standards/

ASTM International. (2014b). *Standard specification for additive manufacturing titanium-6 aluminum-4 vanadium with powder bed fusion (F2924-14)*. ASTM International. https://www.astm.org/Standards/

Ataee, A., Li, Y., Fraser, D., Song, G., & Wen, C. (2018). Anisotropic Ti-6Al-4V gyroid scaffolds manufactured by electron beam melting (EBM) for bone implant applications. *Materials & Design*, *137*, 345–354. https://doi.org/10.1016/j.matdes.2017.10.040

Barba, D., Alabort, E., & Reed, R. C. (2019). Synthetic bone: Design by additive manufacturing. *Acta Biomaterialia*, *97*, 637–656. https://doi.org/10.1016/j.actbio.2019.07.049

Benedetti, M., du Plessis, A., Ritchie, R., Dallago, M., Razavi, N., & Berto, F. (2021). Architected cellular materials: A review on their mechanical properties towards fatigue-tolerant design and fabrication. *Materials Science and Engineering: R: Reports*, *144*, 100606. https://doi.org/10.1016/j.mser.2021.100606

Bergmann, G., Bender, A., Dymke, J., Duda, G., & Damm, P. (2016). Standardized loads acting in hip implants. *PLoS ONE*, *11*(5), e0155612. https://doi.org/10.1371/journal.pone.0155612

Bobbert, F., Lietaert, K., Eftekhari, A., Pouran, B., Ahmadi, S., Weinans, H., & Zadpoor, A. (2017). Additively manufactured metallic porous biomaterials based on minimal surfaces: A unique combination of topological, mechanical, and mass transport properties. *Acta Biomaterialia*, *53*, 572–584. https://doi.org/10.1016/j.actbio.2017.02.024

Bonatti, C., & Mohr, D. (2019). Smooth-shell metamaterials of cubic symmetry: Anisotropic elasticity, yield strength and specific energy absorption. *Acta Materialia*, *164*, 301–321. https://doi.org/10.1016/j.actamat.2018.10.034

Branemark, P.-I. (1983). Osseointegration and its experimental background. *The Journal of Prosthetic Dentistry*, *50*(3), 399–410. https://doi.org/10.1016/S0022-3913(83)80101-2

British Standards Institution. (2012). *Mechanical testing of metals - Ductility testing - Compression test for porous and cellular metals (BS ISO 13314:2011)*. British Standards Institution. https://shop.bsigroup.com/

Carrion, P. E., Soltani-Tehrani, A., Phan, N., & Shamsaei, N. (2019). Powder recycling effects on the tensile and fatigue behavior of additively manufactured Ti-6Al-4V parts. *JOM*, *71*(3), 963–973. https://doi.org/10.1007/s11837-018-3248-7

Catchpole-Smith, S., Sélo, R., Davis, A., Ashcroft, I., Tuck, C., & Clare, A. (2019). Thermal conductivity of TPMS lattice structures manufactured via laser powder bed fusion. *Additive Manufacturing*, *30*, 100846. https://doi.org/10.1016/j.addma.2019.100846

Cheng, X. Y., Li, S. J., Murr, L. E., Zhang, Z. B., Hao, Y. L. Y. L., Yang, R., Medina, F. R., & Wicker, R. B. (2012). Compression deformation behavior of Ti-6Al–4V alloy with cellular structures fabricated by electron beam melting. *Journal of the Mechanical Behavior of Biomedical Materials*, *16*(1), 153–162. https://doi.org/10.1016/j.jmbbm.2012.10.005

Cordova, L., Campos, M., & Tinga, T. (2019). Revealing the effects of powder reuse for selective laser melting by powder characterization. *JOM*, *71*(3), 1062–1072. https://doi.org/10.1007/s11837-018-3305-2

CORE-Materials. (2006). Materials selection of femoral stem component. Retrieved April 23, 2024, from https://www.doitpoms.ac.uk/tlplib/bones/stem.php

Cuadrado, A., Yánez, A., Martel, O., Deviaene, S., & Monopoli, D. (2017). Influence of load orientation and of types of loads on the mechanical properties of porous Ti6Al4V biomaterials. *Materials & Design*, *135*, 309–318. https://doi.org/10.1016/j.matdes.2017.09.045

Dallago, M., Fontanari, V., Torresani, E., Leoni, M., Pederzolli, C., Potrich, C., & Benedetti, M. (2018). Fatigue and biological properties of Ti-6Al-4V ELI cellular structures with variously arranged cubic cells made by selective laser melting. *Journal of the Mechanical Behavior of Biomedical Materials*, *78*, 381–394. https://doi.org/10.1016/j.jmbbm.2017.11.044

Del Guercio, G., Galati, M., & Saboori, A. (2021a). Electron beam melting of Ti-6Al-4V lattice structures: Correlation between post heat treatment and mechanical properties. *The International Journal of Advanced Manufacturing Technology*, *116*(11-12), 3535–3547. https://doi.org/10.1007/s00170-021-07619-w

Del Guercio, G., Galati, M., & Saboori, A. (2021b). Innovative approach to evaluate the mechanical performance of Ti–6Al–4V lattice structures produced by electron beam melting process. *Metals and Materials International*, *27*(1), 55–67. https://doi.org/10.1007/s12540-020-00745-2

Del Guercio, G., Galati, M., Saboori, A., Fino, P., & Iuliano, L. (2020). Microstructure and mechanical performance of Ti–6Al–4V lattice structures manufactured via electron beam melting (EBM): A review. *Acta Metallurgica Sinica (English Letters)*, *33*(2), 183–203. https://doi.org/10.1007/s40195-020-00998-1

Denti, L., Sola, A., Defanti, S., Sciancalepore, C., & Bondioli, F. (2019). Effect of powder recycling in laser-based powder bed fusion of Ti-6Al-4V. *Manufacturing Technology*, *19*(2), 190–196. https://doi.org/10.21062/ujep/268.2019/a/1213-2489/MT/19/2/190

Deshpande, V., Ashby, M., & Fleck, N. (2001). Foam topology: Bending versus stretching dominated architectures. *Acta Materialia*, *49*(6), 1035–1040. https://doi.org/10.1016/S1359-6454(00)00379-7

du Plessis, A., Razavi, N., Benedetti, M., Murchio, S., Leary, M., Watson, M., Bhate, D., & Berto, F. (2022). Properties and applications of additively manufactured metallic cellular materials: A review. *Progress in Materials Science*, *125*, 100918. https://doi.org/10.1016/j.pmatsci.2021.100918

Ducato, A., Fratini, L., La Cascia, M., & Mazzola, G. (2013). An automated visual inspection system for the classification of the phases of Ti-6Al-4V titanium alloy. *Computer Analysis of Images and Pattern*, *8048*, 362–369. https://doi.org/10.1007/978-3-642-40246-3_45

Egan, P. F., Gonella, V. C., Engensperger, M., Ferguson, S. J., & Shea, K. (2017). Computationally designed lattices with tuned properties for tissue engineering using 3D printing. *PLoS ONE*, *12*(8), e0182902. https://doi.org/10.1371/journal.pone.0182902

Epasto, G., Palomba, G., D'Andrea, D., Guglielmino, E., Di Bella, S., & Traina, F. (2019). Ti-6Al-4V ELI microlattice structures manufactured by electron beam melting: Effect of unit cell dimensions and morphology on mechanical behaviour. *Materials Science and Engineering A*, *753*, 31–41. https://doi.org/10.1016/j.msea.2019.03.014

Galati, M., & Iuliano, L. (2018). A literature review of powder-based electron beam melting focusing on numerical simulations. *Additive Manufacturing*, *19*, 1–20. https://doi.org/10.1016/j.addma.2017.11.001

General Electric. (2024). GE additive machines: Arcam EBM Q10plus. Retrieved March 23, 2024, from https://www.ge.com/additive/additive-manufacturing/machines/ebm-machines/arcam-ebm-q10plus

Ghods, S., Schultz, E., Wisdom, C., Schur, R., Pahuja, R., Montelione, A., Arola, D., & Ramulu, M. (2020). Electron beam additive manufacturing of Ti6Al4V: Evolution of powder morphology and part microstructure with powder reuse. *Materialia*, *9*, 100631. https://doi.org/10.1016/j.mtla.2020.100631

Gibson, L. J. (2003). Cellular solids. *Mrs Bulletin*, *28*(4), 270–274. https://doi.org/10.1557/mrs2003.79

Gibson, L. J., & Ashby, M. F. (1997). *Cellular solids: Structure and properties* (2nd). Cambridge University Press. https://doi.org/10.1017/CBO9781139878326

Grell, W., Solis-Ramos, E., Clark, E., Lucon, E., Garboczi, E., Predecki, P., Loftus, Z., & Kumosa, M. (2017). Effect of powder oxidation on the impact toughness of electron beam melting Ti-6Al-4V. *Additive Manufacturing*, *17*, 123–134. https://doi.org/10.1016/j.addma.2017.08.002

Gupta, A., & Babu L, S. (2023). Triply periodic minimal surfaces: An overview of their features, failure mechanisms, and applications. *Journal of Mines, Metals and Fuels*, *70*, 211–221. https://doi.org/10.18311/jmmf/2022/31230

Harrysson, O. L., Cansizoglu, O., Marcellin-Little, D. J., Cormier, D. R., & West, H. A. (2008). Direct metal fabrication of titanium implants with tailored materials and mechanical properties using electron beam melting technology. *Materials Science and Engineering: C*, *28*(3), 366–373. https://doi.org/10.1016/j.msec.2007.04.022

Hedayati, R., Ahmadi, S., Lietaert, K., Pouran, B., Li, Y., Weinans, H., Rans, C., & Zadpoor, A. (2018). Isolated and modulated effects of topology and material type on the mechanical properties of additively manufactured porous biomaterials. *Journal of the Mechanical Behavior of Biomedical Materials*, *79*, 254–263. https://doi.org/10.1016/j.jmbbm.2017.12.029

Jamshidinia, M., Kong, F., & Kovacevic, R. (2012). Temperature distribution and fluid flow modeling of electron beam melting (EBM). *Volume 7: Fluids and Heat Transfer, Parts A, B, C, and D*, *7*, 3089–3101. https://doi.org/10.1115/IMECE2012-89440

Jin, W., & Chu, P. K. (2019). Orthopedic implants. In *Encyclopedia of biomedical engineering* (pp. 425–439, Vol. 1-3). Elsevier. https://doi.org/10.1016/B978-0-12-801238-3.10999-7

Karachalios, T., Tsatsaronis, C., Efraimis, G., Papadelis, P., Lyritis, G., & Diakoumopoulos, G. (2004). The long-term clinical relevance of calcar atrophy caused by stress shielding in total hip arthroplasty. *The Journal of Arthroplasty*, *19*(4), 469–475. https://doi.org/10.1016/j.arth.2003.12.081

Kolken, H. M. A., Garcia, A. F., Du Plessis, A., Rans, C., Mirzaali, M. J., & Zadpoor, A. A. (2021). Fatigue performance of auxetic meta-biomaterials. *Acta Biomaterialia*, *126*, 511–523. https://doi.org/10.1016/j.actbio.2021.03.015

Lefebvre, L. P., Baril, E., & Bureau, M. N. (2009). Effect of the oxygen content in solution on the static and cyclic deformation of titanium foams. *Journal of Materials Science: Materials in Medicine*, *20*(11), 2223–2233. https://doi.org/10.1007/s10856-009-3798-x

Li, S. J., Murr, L. E., Cheng, X. Y., Zhang, Z. B., Hao, Y. L., Yang, R., Medina, F. R., & Wicker, R. B. (2012). Compression fatigue behavior of Ti–6Al–4V mesh arrays fabricated by electron beam melting. *Acta Materialia*, *60*(3), 793–802. https://doi.org/10.1016/j.actamat.2011.10.051

Lietaert, K., Cutolo, A., Boey, D., & Van Hooreweder, B. (2018). Fatigue life of additively manufactured Ti6Al4V scaffolds under tension-tension, tension-compression and compression-compression fatigue load. *Scientific Reports*, *8*(1), 4957. https://doi.org/10.1038/s41598-018-23414-2

Liu, B., Wang, H., Zhang, N., Zhang, M., & Cheng, C.-K. (2021). Femoral stems with porous lattice structures: A review. *Frontiers in Bioengineering and Biotechnology*, *9*, 1–19. https://doi.org/10.3389/fbioe.2021.772539

Liu, F., Mao, Z., Zhang, P., Zhang, D. Z., Jiang, J., & Ma, Z. (2018). Functionally graded porous scaffolds in multiple patterns: New design method, physical and mechanical properties. *Materials & Design*, *160*, 849–860. https://doi.org/10.1016/j.matdes.2018.09.053

Liu, R., Chen, W., & Zhao, J. (2023). A review on factors affecting the mechanical properties of additively-manufactured lattice structures. *Journal of Materials Engineering and Performance*. https://doi.org/10.1007/s11665-023-08423-1

Liu, S., & Shin, Y. C. (2019). Additive manufacturing of Ti6Al4V alloy: A review. *Materials & Design*, *164*, 107552. https://doi.org/10.1016/j.matdes.2018.107552

Lütjering, G., & Williams, J. C. (2007). *Titanium* (2nd). Springer Berlin Heidelberg. https://doi.org/10.1007/978-3-540-73036-1

McGregor, M., Patel, S., McLachlin, S., & Mihaela Vlasea. (2021). Architectural bone parameters and the relationship to titanium lattice design for powder bed fusion additive manufacturing. *Additive Manufacturing*, *47*, 102273. https://doi.org/10.1016/j.addma.2021.102273

Millis, D. L. (2014). Responses of musculoskeletal tissues to disuse and remobilization. In *Canine rehabilitation and physical therapy* (pp. 92–153). Elsevier. https://doi.org/10.1016/B978-1-4377-0309-2.00007-7

Montelione, A., Ghods, S., Schur, R., Wisdom, C., Arola, D., & Ramulu, M. (2020). Powder reuse in electron beam melting additive manufacturing of Ti6Al4V: Particle microstructure, oxygen content and mechanical properties. *Additive Manufacturing*, *35*, 101216. https://doi.org/10.1016/j.addma.2020.101216

Murr, L., & Gaytan, S. (2014). Electron beam melting. In *Comprehensive materials processing* (pp. 135–161, Vol. 10). Elsevier. https://doi.org/10.1016/B978-0-08-096532-1.01004-9

Nagels, J., Stokdijk, M., & Rozing, P. M. (2003). Stress shielding and bone resorption in shoulder arthroplasty. *Journal of Shoulder and Elbow Surgery*, *12*(1), 35–39. https://doi.org/10.1067/mse.2003.22

Naghavi, S. A., Lin, C., Sun, C., Tamaddon, M., Basiouny, M., Garcia-Souto, P., Taylor, S., Hua, J., Li, D., Wang, L., & Liu, C. (2022). Stress shielding and bone resorption of press-fit polyether–ether–ketone (PEEK) hip prosthesis: A sawbone model study. *Polymers*, *14*(21). https://doi.org/10.3390/polym14214600

Nandwana, P., Kirka, M. M., Paquit, V. C., Yoder, S., & Dehoff, R. R. (2018). Correlations between powder feedstock 1uality, in situ porosity detection, and fatigue behavior of Ti-6Al-4V

fabricated by powder bed electron beam melting: A step towards qualification. *JOM*, *70*(9), 1686–1691. https://doi.org/10.1007/s11837-018-3034-6

Özbilen, S., Liebert, D., Beck, T., & Bram, M. (2016). Fatigue behavior of highly porous titanium produced by powder metallurgy with temporary space holders. *Materials Science and Engineering: C*, *60*, 446–457. https://doi.org/10.1016/j.msec.2015.11.050

Parthasarathy, J., Starly, B., Raman, S., & Christensen, A. (2010). Mechanical evaluation of porous titanium (Ti6Al4V) structures with electron beam melting (EBM). *Journal of the Mechanical Behavior of Biomedical Materials*, *3*(3), 249–259. https://doi.org/10.1016/j.jmbbm.2009.10.006

Petrovic, V., & Niñerola, R. (2015). Powder recyclability in electron beam melting for aeronautical use. *Aircraft Engineering and Aerospace Technology*, *87*(2), 147–155. https://doi.org/10.1108/AEAT-11-2013-0212

Popov, V. V., Katz-Demyanetz, A., Garkun, A., & Bamberger, M. (2018). The effect of powder recycling on the mechanical properties and microstructure of electron beam melted Ti-6Al-4 V specimens. *Additive Manufacturing*, *22*, 834–843. https://doi.org/10.1016/j.addma.2018.06.003

Quintana, O. A., Alvarez, J., Mcmillan, R., Tong, W. D., & Tomonto, C. (2018). Effects of reusing Ti-6Al-4V powder in a selective laser melting additive system operated in an industrial setting. *JOM*, *70*(9), 1863–1869. https://doi.org/10.1007/s11837-018-3011-0

Raghavendra, S., Molinari, A., Cao, A., Gao, C., Berto, F., Zappini, G., & Benedetti, M. (2021). Quasi-static compression and compression–compression fatigue behavior of regular and irregular cellular biomaterials. *Fatigue & Fracture of Engineering Materials & Structures*, *44*(5), 1178–1194. https://doi.org/10.1111/ffe.13422

Raghavendra, S., Molinari, A., Fontanari, V., Zappini, G., & Benedetti, M. (2020). Evaluation of static and fatigue properties of regular lattice and trabecular cellular structures. *Procedia Structural Integrity*, 517–524. https://doi.org/10.1016/j.prostr.2020.10.061

Riedlbauer, D., Scharowsky, T., Singer, R. F., Steinmann, P., Körner, C., & Mergheim, J. (2017). Macroscopic simulation and experimental measurement of melt pool characteristics in selective electron beam melting of Ti-6Al-4V. *The International Journal of Advanced Manufacturing Technology*, *88*(5-8), 1309–1317. https://doi.org/10.1007/s00170-016-8819-6

Ryan, G., Pandit, A., & Apatsidis, D. P. (2006). Fabrication methods of porous metals for use in orthopaedic applications. *Biomaterials*, *27*(13), 2651–2670. https://doi.org/10.1016/j.biomaterials.2005.12.002

Schur, R., Ghods, S., Schultz, E., Wisdom, C., Pahuja, R., Montelione, A., Arola, D., & Ramulu, M. (2020). A fractographic analysis of additively manufactured Ti6Al4V by electron beam melting: Effects of powder reuse. *Journal of Failure Analysis and Prevention*, *20*(3), 794–803. https://doi.org/10.1007/s11668-020-00875-0

Shan, D., Zong, Y., Lv, Y., & Guo, B. (2008). The effect of hydrogen on the strengthening and softening of Ti-6Al-4V alloy. *Scripta Materialia*, *58*(6), 449–452. https://doi.org/10.1016/j.scriptamat.2007.10.047

Shaoqing, Z., & Linruo, Z. (1995). Effect of hydrogen on the superplasticity and microstructure of Ti-6Al-4V alloy. *Journal of Alloys and Compounds*, *218*(2), 233–236. https://doi.org/10.1016/0925-8388(94)01384-5

Soro, N., Saintier, N., Merzeau, J., Veidt, M., & Dargusch, M. S. (2021). Quasi-static and fatigue properties of graded Ti–6Al–4V lattices produced by laser powder bed fusion (LPBF). *Additive Manufacturing*, *37*, 101653. https://doi.org/10.1016/j.addma.2020.101653

Sumner, D. (2015). Long-term implant fixation and stress-shielding in total hip replacement. *Journal of Biomechanics*, *48*(5), 797–800. https://doi.org/10.1016/j.jbiomech.2014.12.021

Sun, Y., Aindow, M., & Hebert, R. J. (2018). The effect of recycling on the oxygen distribution in Ti-6Al-4V powder for additive manufacturing. *Materials at High Temperatures*, *35*(1-3), 217–224. https://doi.org/10.1080/09603409.2017.1389133

Surmeneva, M. A., Surmenev, R. A., Chudinova, E. A., Koptioug, A., Tkachev, M. S., Gorodzha, S. N., & Rännar, L. E. (2017). Fabrication of multiple-layered gradient cellular metal scaffold via electron beam melting for segmental bone reconstruction. *Materials and Design*, *133*, 195–204. https://doi.org/10.1016/j.matdes.2017.07.059

Sutton, A. T., Kriewall, C. S., Leu, M. C., & Newkirk, J. W. (2017). Powder characterisation techniques and effects of powder characteristics on part properties in powder-bed fusion processes. *Virtual and Physical Prototyping*, *12*(1), 3–29. https://doi.org/10.1080/17452759.2016.1250605

Tan, X., Tan, Y., Chow, C., Tor, S., & Yeong, W. (2017). Metallic powder-bed based 3D printing of cellular scaffolds for orthopaedic implants: A state-of-the-art review on manufacturing, topological design, mechanical properties and biocompatibility. *Materials Science and Engineering: C*, *76*, 1328–1343. https://doi.org/10.1016/j.msec.2017.02.094

Tang, H. P., Qian, M., Liu, N., Zhang, X. Z., Yang, G. Y., & Wang, J. (2015). Effect of powder reuse times on additive manufacturing of Ti-6Al-4V by selective electron beam melting. *JOM*, *67*(3), 555–563. https://doi.org/10.1007/s11837-015-1300-4

Wang, X., Xu, S., Zhou, S., Xu, W., Leary, M., Choong, P., Qian, M., Brandt, M., & Xie, Y. M. (2016). Topological design and additive manufacturing of porous metals for bone scaffolds and orthopaedic implants: A review. *Biomaterials*, *83*, 127–141. https://doi.org/10.1016/j.biomaterials.2016.01.012

Weißmann, V., Bader, R., Hansmann, H., & Laufer, N. (2016). Influence of the structural orientation on the mechanical properties of selective laser melted Ti6Al4V open-porous scaffolds. *Materials & Design*, *95*, 188–197. https://doi.org/10.1016/j.matdes.2016.01.095

Wu, Y. C., Kuo, C. N., Shie, M. Y., Su, Y. L., Wei, L. J., Chen, S. Y., & Huang, J. C. (2018). Structural design and mechanical response of gradient porous Ti-6Al-4V fabricated by electron beam additive manufacturing. *Materials & Design*, *158*, 256–265. https://doi.org/10.1016/j.matdes.2018.08.027

Xiao, L. J., Song, W. D., Wang, C., Liu, H. Y., Tang, H. P., & Wang, J. Z. (2015). Mechanical behavior of open-cell rhombic dodecahedron Ti-6Al-4V lattice structure. *Materials Science and Engineering A*, *640*, 375–384. https://doi.org/10.1016/j.msea.2015.06.018

Xiong, Y., Wang, W., Gao, R., Zhang, H., Dong, L., Qin, J., Wang, B., Jia, W., & Li, X. (2020). Fatigue behavior and osseointegration of porous Ti-6Al-4V scaffolds with dense core for dental application. *Materials and Design*, *195*, 108994. https://doi.org/10.1016/j.matdes.2020.108994

Yan, M., Xu, W., Dargusch, M. S., Tang, H. P., Brandt, M., & Qian, M. (2014). Review of effect of oxygen on room temperature ductility of titanium and titanium alloys. *Powder Metallurgy*, *57*(4), 251–257. https://doi.org/10.1179/1743290114Y.0000000108

Yánez, A., Cuadrado, A., Martel, O., Afonso, H., & Monopoli, D. (2018). Gyroid porous titanium structures: A versatile solution to be used as scaffolds in bone defect reconstruction. *Materials & Design*, *140*, 21–29. https://doi.org/10.1016/j.matdes.2017.11.050

Yánez, A., Fiorucci, M. P., Cuadrado, A., Martel, O., & Monopoli, D. (2020). Surface roughness effects on the fatigue behaviour of gyroid cellular structures obtained by additive manufacturing. *International Journal of Fatigue*, *138*, 105702. https://doi.org/10.1016/j.ijfatigue.2020.105702

Yánez, A., Herrera, A., Martel, O., Monopoli, D., & Afonso, H. (2016). Compressive behaviour of gyroid lattice structures for human cancellous bone implant applications. *Materials Science and Engineering C*, *68*, 445–448. https://doi.org/10.1016/j.msec.2016.06.016

Yang, L., Mertens, R., Ferrucci, M., Yan, C., Shi, Y., & Yang, S. (2019). Continuous graded gyroid cellular structures fabricated by selective laser melting: Design, manufacturing and mechanical properties. *Materials & Design*, *162*, 394–404. https://doi.org/10.1016/j.matdes.2018.12.007

Yang, L., Yan, C., Han, C., Chen, P., Yang, S., & Shi, Y. (2018). Mechanical response of a triply periodic minimal surface cellular structures manufactured by selective laser melting. *International Journal of Mechanical Sciences*, *148*, 149–157. https://doi.org/10.1016/j.ijmecsci.2018.08.039

Yuan, W., Hou, W., Li, S., Hao, Y., Yang, R., Zhang, L. C., & Zhu, Y. (2018). Heat treatment enhancing the compressive fatigue properties of open-cellular Ti-6Al-4V alloy prototypes fabricated by electron beam melting. *Journal of Materials Science and Technology*, *34*(7), 1127–1131. https://doi.org/10.1016/j.jmst.2017.12.003

Zadpoor, A. A. (2019). Additively manufactured porous metallic biomaterials. *Journal of Materials Chemistry B*, *7*(26), 4088–4117. https://doi.org/10.1039/C9TB00420C

Zenith Tecnica. (2024). Zenith Tecnica Industries. Retrieved March 29, 2024, from https://zenithtecnica.com/industries/

Zhang, C., Zhang, L., Liu, L., Lv, L., Gao, L., Liu, N., Wang, X., & Ye, J. (2020). Mechanical behavior of a titanium alloy scaffold mimicking trabecular structure. *Journal of Orthopaedic Surgery and Research*, *15*(1), 40. https://doi.org/10.1186/s13018-019-1489-y

Zhang, X., Fang, G., Leeflang, S., Zadpoor, A. A., & Zhou, J. (2019). Topological design, permeability and mechanical behavior of additively manufactured functionally graded porous metallic biomaterials. *Acta Biomaterialia*, *84*, 437–452. https://doi.org/10.1016/j.actbio.2018.12.013

Zhang, X. Z., Tang, H. P., Leary, M., Song, T., Jia, L., & Qian, M. (2018). Toward manufacturing quality Ti-6Al-4V lattice struts by selective electron beam melting (SEBM) for lattice design. *JOM*, *70*(9), 1870–1876. https://doi.org/10.1007/s11837-018-3030-x

Zhao, S., Li, S. J., Wang, S. G., Hou, W. T., Li, Y., Zhang, L., Hao, Y., Yang, R., Misra, R. D. K., & Murr, L. (2018). Compressive and fatigue behavior of functionally graded Ti-6Al-4V meshes fabricated by electron beam melting. *Acta Materialia*, *150*, 1–15. https://doi.org/10.1016/j.actamat.2018.02.060

Zhao, S., Li, S., Hou, W., Hao, Y., Yang, R., & Misra, R. (2016). The influence of cell morphology on the compressive fatigue behavior of Ti-6Al-4V meshes fabricated by electron beam melting. *Journal of the Mechanical Behavior of Biomedical Materials*, *59*, 251–264. https://doi.org/10.1016/j.jmbbm.2016.01.034

Zhong, H., Song, T., Li, C., Das, R., Gu, J., & Qian, M. (2023). The Gibson-Ashby model for additively manufactured metal lattice materials: Its theoretical basis, limitations and new insights from remedies. *Current Opinion in Solid State and Materials Science*, *27*(3), 101081. https://doi.org/10.1016/j.cossms.2023.101081

Zong, Y., Shan, D., Lu, Y., & Guo, B. (2007). Effect of 0.3wt%H addition on the high temperature deformation behaviors of Ti–6Al–4V alloy. *International Journal of Hydrogen Energy*, *32*(16), 3936–3940. https://doi.org/10.1016/j.ijhydene.2007.04.032